GROUNDWATER INVESTIGATIONS USING GEOPHYSICAL TECHNIQUES AT MAROPHE, THE OKAVANGO DELTA, BOTSWANA

KEBABONYE LALETSANG

GROUNDWATER INVESTIGATIONS USING GEOPHYSICAL TECHNIQUES AT MAROPHE, THE OKAVANGO DELTA, BOTSWANA.

By Kebabonye Laletsang©

A thesis submitted to the

school of graduate studies

in partial fulfilment of the

requirements for the degree of

Master of Science.

Department of Earth Sciences

Memorial University of Newfoundland

December, 1995.

St. John's Newfoundland

ISBN 0-612-13915-8

Canada

Memorial
University of Newfoundland

This is to authorize the Dean of Graduate Studies to deposit two copies of my thesis/report entitled
GROUNDWATER ~~in~~ INVESTIGATIONS USING GEOPHYSICAL TECHNIQUES AT MAROPHE, THE OKAVANGO DELTA, BOTSWANA.

in the University Library, on the following conditions. I understand that I may choose only ONE of the Options here listed, and may not afterwards apply for any additional restriction. I further understand that the University will not grant any restriction on the publication of thesis/report abstracts.

(After reading the explanatory notes at the foot of this form, delete TWO of (a), (b) and (c), whichever are inapplicable.)

The conditions of deposit are:

(a) that two copies are to be made available to users at the discretion of their custodians,

OR

(b) that access to, and quotation from, this thesis/report is to be granted only with my written permission for a period of one year from the date on which the thesis/report, after the approval of the award of a degree, is entrusted to the care of the University, namely, _____ 19 ____, after which time the two copies are to be made available to users at the discretion of their custodians,

OR

(c) that access to, and quotation from, this thesis/report is to be granted only with my written permission for a period of _____ years from the date on which the thesis/report, after approval for the award of a degree, is entrusted to the care of the University; namely, _____, 19 ____; after which time two copies are to be made available to users at the discretion of their custodians.

Date 19 OCT., 1995 Signed _____

_____ Witnessed by Maureen L. Moore
Dean of Graduate Studies

NOTES

1. *Restriction (b) will be granted on application, without reason given.*

   However, applications for restriction (c) must be accompanied with a detailed explanation, indicating why the restriction is thought to be necessary and justifying the length of time requested. Restrictions required on the grounds that the thesis is being prepared for publication, or that patents are awaited, will not be permitted to exceed **three** *years.*

   Restriction (c) can be permitted only by a Committee entrusted by the university with the task of examining such applications, and will be granted only in exceptional circumstances.

2. *Thesis writers are reminded that, if they have been engaged in contractual research, they may have already agreed to restrict access to their thesis until the terms of the contract have been fulfilled.*

Abstract

Results from a seismic reflection survey at Marophe, the Okavango Delta, are presented. The study aims to locate and characterize potential Karoo aquifers near Maun, as a supplement to the municipal water supply. The groundwater resources for Maun comprise the Upper Kalahari beds and alluvial sand aggregates. The Lower Kalahari formations contain saline groundwater. The shallow aquifers in the Upper Kalahari beds do not meet the present water demand, and are prone to nitrate pollution since they are unconfined and close to the town. Alternative groundwater resources are therefore presently being sought in the underlying Karoo strata. A variety of geophysical methods have been used to investigate the Okavango, particularly regarding the existence of Karoo beds. These studies have been inconclusive, in part due to the lack of stratigraphic boreholes required to calibrate potential field data. The present seismic reflection survey is a first attempt to use the seismic reflection method to investigate the Okavango region for hydrogeological purposes.

The geology of Ngamiland comprises Archean granitoid gneiss, the Damara metamorphic belt, and the Ghanzi-Chobe fold belt. Karoo rocks are inferred to overlie the Archean basement throughout the Okavango Delta. The geological structure was interpreted by re-analysis of the 1978 aeromagnetic data.

A seismic reflection survey was conducted along an existing cut-line ~ 14.5 km west of Maun. The survey consisted of a symmetric split-spread with 48 recording channels at 9.0 m intervals and recording at 0.5 ms sampling rate. The signal source was a Betsy seismic gun firing 12 gauge shells at the ground surface. The data set collected during this survey is discussed in this thesis.

Refraction statics analysis of the field records reveal the presence of a ~ 15 m unsaturated zone underlain by an impermeable layer. AVO inversion clearly images the base of the Kalahari beds, which manifests itself as a bright spot on the stacked section. Pseudo-acoustic impedance and velocity inversion of the bright spot show that ~ 377 m of sediment exist south of the Kunyere fault. These comprise ~ 191 m Kalahari and ~ 186 m Karoo beds. To the north, the stacked time section indicates ~ 570 m of sediment comprising ~ 155 m Okavango beds, ~ 230 m Kalahari, and ~ 185 m of Karoo. The Kunyere fault zone comprises a number of faults with a total NW throw of ~ 155 m. The basement at Marophe comprises a mafic igneous body.

The seismic survey has established that potential Karoo aquifers exist below Tertiary cover at Marophe but that no confining Karoo basalt occurs above the sediments. This allows direct recharge from the overlying Kalahari beds, but also salt contamination of the aquifer. The survey has also shown that the seismic reflection technique has direct applicability to groundwater investigations in the Okavango area.

Table of Contents

List of Figures

List of Tables

Acknowledgments

Sincere gratitude and appreciation is expressed towards the following:

-the Botswana Geological Survey Geophysics Division for providing field equipment and crew to carry out the reflection survey.

-Canadian International Development Agency (CIDA) provided financial support for the project through their University of Manitoba/University of Botswana Linkage program.

-Dr. J.A. Wright initiated and supervised field investigations and also supervised the entire data processing and report compilation phase.

-Dr. W. Scott patiently reviewed and edited this manuscript.

-Mr. B. Hoffe was involved in the data acquisition and offered advice throughout data processing and the compilation of this thesis.

-the systems analyst, Mr. Tony Kocurko patiently offered advice and guidance regarding processing software and applications. The geophysics staff and students provided an amiable and very stimulating learning environment.

1.0 INTRODUCTION

The town of Maun is situated on the southern edge of the Okavango delta (fig. 1-1). Despite the occurrence of large quantities of surface water in the upper reaches of the delta, communities on the southern edge depend on groundwater abstracted from shallow boreholes. These boreholes tap perched aquifers within the recent Kalahari semi-consolidated sediments and floodplain sequences. The perched aquifers are everywhere in the vicinity of Maun underlain by either saline or brackish groundwater within the Lower Kalahari beds (BRGM, 1984). This fact militates against attempts to develop deep wells to allow greater abstraction rates from the present well fields. The other limiting factor is that the predominantly alluvial facies Thamalakane and Shashe River aquifers have poor hydraulic properties such as transmissivity and hydraulic conductivity (BRGM. 1984). Attempts to channel the Okavango surface water for domestic and industrial use have been relinquished in favour of the preservation of the aesthetic and ecological aspects of the deltaic environment (IUCN, 1992).

In the face of this bleak future water supply prospect for Maun, it has become necessary to search for alternative groundwater sources to augment the present well fields and for future development and expansion of the town. Against this backdrop, attention is presently being focused on locating, and characterising deep freshwater aquifers in the proximity of the town. The Karoo succession is known to contain prolific groundwater aquifers elsewhere in Botswana (Farr et al., 1981; SMEC, 1987). Since faulted outliers

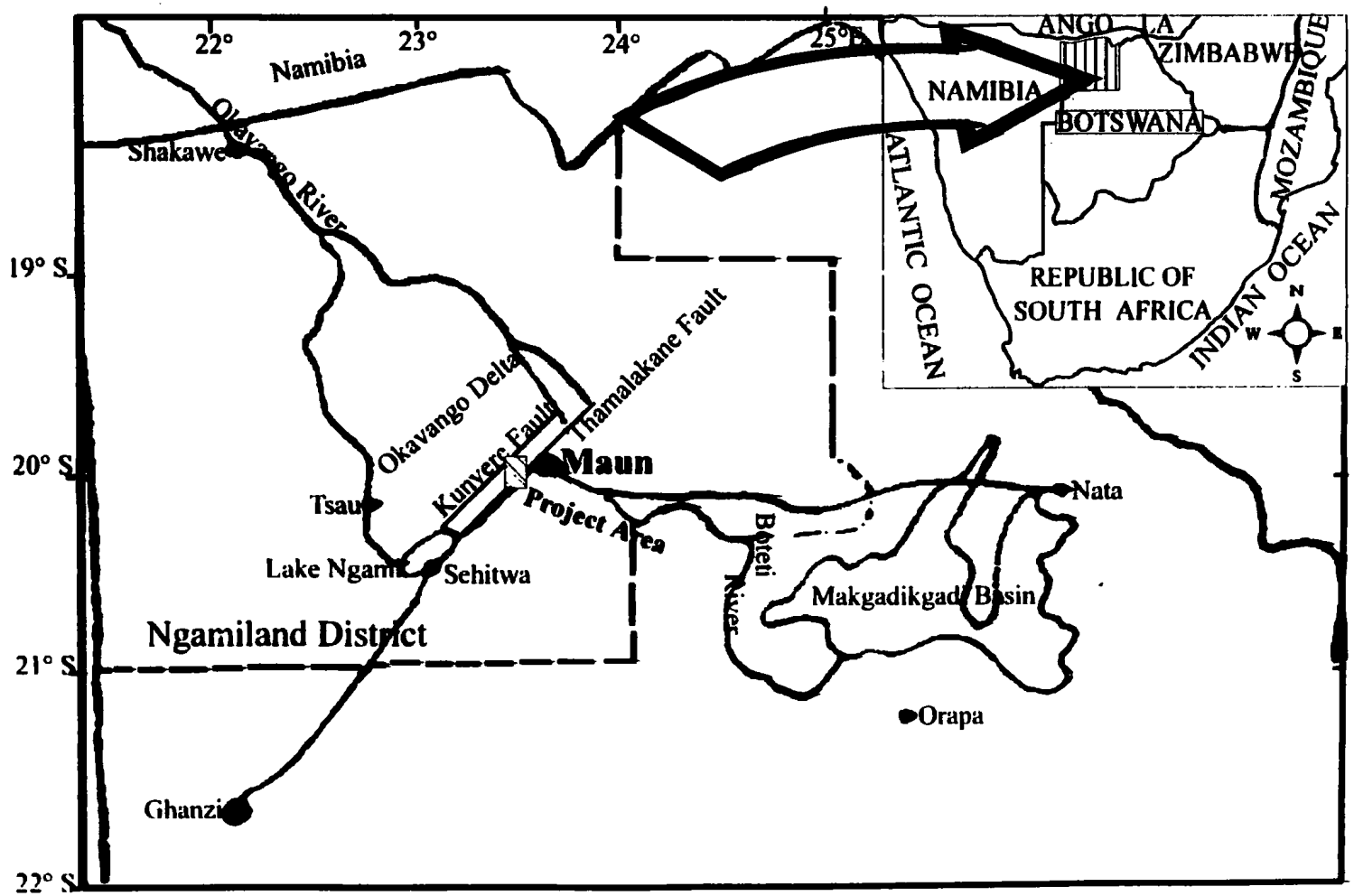

Figure 1-1: Location map showing the regional setting of the study area. The district of Ngamiland and the Okavango Delta are shown.

of Karoo affinity are suspected to occur beneath the Kalahari sediments within the delta, and also in proximity to Maun (Hutchins et al., 1976; Reeves, 1978), it forms the target for the present seismic reflection experiment. The current reflection survey was designed to map the subsurface geology and structure across one of the main structural features of the delta: the southeast bounding Kunyere fault zone. The fact that the groundwater potential of the Karoo succession has not yet been investigated in the Maun region owes to its complete lack of exposure, the paucity of appropriate geophysical exploration techniques within the country, and the occurrence of saline water in the Lower Kalahari beds. This latter fact is frequently the main reason for drillers to terminate boreholes at shallow depth. It was assumed in the current work that Karoo aquifers have no hydraulic continuity with the overlying Kalahari beds, such that freshwater may be present at depth. This would be the case if the Karoo stratigraphy in the Okavango area is similar to that studied elsewhere in the country by Farr et al. (1981) and Smith (1984). In this case the Karoo sandstone aquifers are confined by a basalt sheet, which prevents hydraulic continuity with the overlying Kalahari beds. Recharge to such buried aquifers can occur along fracture zones and near the basement ridges where the Karoo strata may subcrop at shallow depth.

It was initially intended to carry out a number of short seismic reflection profiles normal to the regional strike near Maun (i.e. in a NW-SE direction). However, due to unforeseen logistical and financial constraints, efforts were concentrated on one ~5 km

seismic profile. The depth of investigation was dependent on the strength of the available impulse signal source (Betsy seismic gun), which attained a maximum depth of ~500 m. It was anticipated that this depth would be adequate to investigate the extent and structure of the crystalline basement and the overlying Karoo beds at a reasonable resolution. Since the Okavango region has been investigated by several geophysical methods (gravity, aeromagnetic, dc (direct current) resistivity, seismic refraction, TDEM (time-domain electromagnetic)) without any conclusive evidence regarding the stratigraphy of the buried Karoo units, seismic reflection seems to be the only exploration method with the capacity to achieve this goal. The details of seismic reflection surveying are elaborated on in the later sections.

Groundwater exploration at Maun was carried out by the French consulting group BRGM (Bureau de Recherches Géologiques et Miniéres) under the aegis of the Ministry of Mineral Resources and Water Affairs in 1984. The survey identified groundwater resources adequate to meet a projected water demand of up to and including the year 1995. This demand projection period is now about to end and additional resources are required. The scope of the BRGM survey allowed for the evaluation of only short-term resources, hence they investigated only shallow perched aquifers in the Upper Kalahari sequence and alluvial sand aggregate deposits.

The present investigation was undertaken in collaboration with the Geological Survey of Botswana, which supplied field equipment and personnel, with the understanding that the data will be on open file to all parties involved. The results of this survey identify a new methodology to assist in the present and future endeavours to locate groundwater resources for Maun.

1.1 Location, Climate, and Geomorphology of the study area

The district of Ngamiland is located in the northwest corner of Botswana, Southern Africa. It occupies the area between latitudes 18° and 21°S, and longitudes 21° and 24° E (fig. 1-1). The Okavango delta occupies a large portion of the Ngamiland district. This delta is essentially an alluvial fan (18 000 km^2) developed at the terminus of a fluvial system that drains the highlands of Southern Angola (McCarthy, 1992). It is an area of great ecological importance with diverse flora and fauna, thriving on the abundant water supply from the Okavango river. The administrative centre of Ngamiland is Maun, which is growing rapidly in concert with a tourist industry supported by the delta.

Ngamiland is an area of low relief, with the exception of isolated inselbergs and some mountainous terrain in the northwest. The altitude varies between 930 and 1000 m above mean sea level at the distal end at Maun and the proximal end ~250 km north of Maun,

and between 924 and 917 m.s.l on either end of the southeast bounding fault zone (Dincer et al., 1987). A large portion of the annual river inflow (~95%) is lost through evapotranspiration over the swamp, and hence all the sediment load is deposited on the delta. This process has accumulated ~300 m of alluvial deposits since the Miocene (McCarthy et al., 1991). The origin of the Okavango delta is enigmatic, but recent opinion is that it is a southwest extension of the East African Rift system which has caused the formation of a graben structure transecting the coarse of the Okavango River (Dincer et al., 1987; McCarthy et al., 1991).

The climate over northwest Botswana is semi-arid, with precipitation confined to the summer months (November to March). Annual rainfall varies between 450-600 mm from the south to the north (Davies and Goldberg, 1980). This precipitation is, however, far exceeded by the annual evapotranspiration, estimated at 1860 mm (Dincer et al., 1987). Daytime temperatures in the summer range from 25 to 40° C, but may fall below 10° C in the winter. A large area of the delta is inundated by floodwater annually, resulting in a swamp of between 6 000 and 12 000 km^2, the exact size depending on the season of the year. Because of the extremely low river grade across the Okavango delta, the arrival of peak floodwater at its distal end is delayed such that very little reaches the cultural centres on the southeastern fringes. It is for this reason that these communities rely on groundwater for domestic and industrial purposes.

2.0 GEOLOGICAL SETTING

2.1 Geology

The known and interpreted geology of Ngamiland is presented in figure 2.1-1 (in the pocket at the back of this thesis), and the stratigraphy is summarised in Table 2-1. The geology of Ngamiland has been summarised by Hutchins et al. (1976). The basement is concealed by a mantle of unconsolidated aeolian Kalahari and alluvial Okavango deposits. The basement complex is comprised of Archean granitoid gneisses. These gneisses are overlain northwest of the delta by rocks of the Damara Supergroup. The Damara strata outcrop at Koanaka, Aha, and Tsodilo hills (fig. 2.1-1). The Damaran succession is bounded in the southeast by the Gomare-Chobe basement fault, which forms the northwest edge of the Okavango graben. Along the southeastern edge of the delta, the Archean gneisses are overlain by strata of the Ghanzi-Chobe fold belt, which runs parallel to the Thamalakane and Kunyere fault zones. This fold belt contains extrusive igneous rocks dated at ~900 Ma (Borg, 1988). The Archean basement is inferred from borehole and geophysical evidence to be overlain by Karoo sediments (Meixner and Peart, 1984). The basement complex is intruded by a NW trending post-Karoo dolerite dike swarm. The dolerite dike swarm was clearly delineated by the 1978 aeromagnetic survey (Paterson et al., 1979; Reeves, 1979).

Table 2-1: A summary of the stratigraphy of Ngamiland. Note that only the lithologies that occur within Ngamiland are included in the table.

Age	Supergroup	Group	Lithology
Cenozoic		Kalahari	aeolian sands and silts, fluvio-lacustrine and pan deposits
Palaeozoic-Mesozoic	Karoo	Stormberg	vesicular and massive tholeiites
		Lebung	pink to white, friable sandstone varicoloured mudstones and silts
		Ecca	angular conglomerates and silts grey mudstones, sandstones
Proterozoic	Damara	Otavi	dolomitic limestones, marls stromatolitic dolomite, arkose greywacke
		Nosib	andesitic tuff arkose, arenite, rhyolite
		Ghanzi	arkose, arenite, stratiform sulphides quartz-feldspar porphyry
Archean	Basement		granitoid gneiss

2.1.1 Damara Supergroup

The Damara orogeny, which culminated at 450-650 Ma, gave rise to a pre-, syn-, and post-orogenic succession collectively called the Damara Supergroup. The Damara orogenic belt is divided into an inland and a coastal branch. The coastal branch has no bearing on the present investigation and will not be discussed further. The inland branch originates at the Atlantic coast in Namibia, stretches through northern Namibia and northwest Botswana, and disappears in the vicinity of the Irumide and Zambezi belts in southeastern Zambia and northern Zimbabwe (fig. 2.1.1-1). The inland branch is some 400-500 km across and is subdivided into a northern marginal zone, a central zone, and a southern marginal zone (Petters, 1991). The present discussion is mainly concerned with the southern marginal zone. The trend of the Damara orogenic belt closely follows the boundary between the Congo and Kalahari cratons. The Damara succession comprises four groups: Nosib, Otavi, Mulden, and Ghanzi. The Ghanzi strata form a persistent fold belt along the southern edge of the Damara belt. The Ghanzi group is stratigraphically equivalent to the Nosib (Borg, 1988).

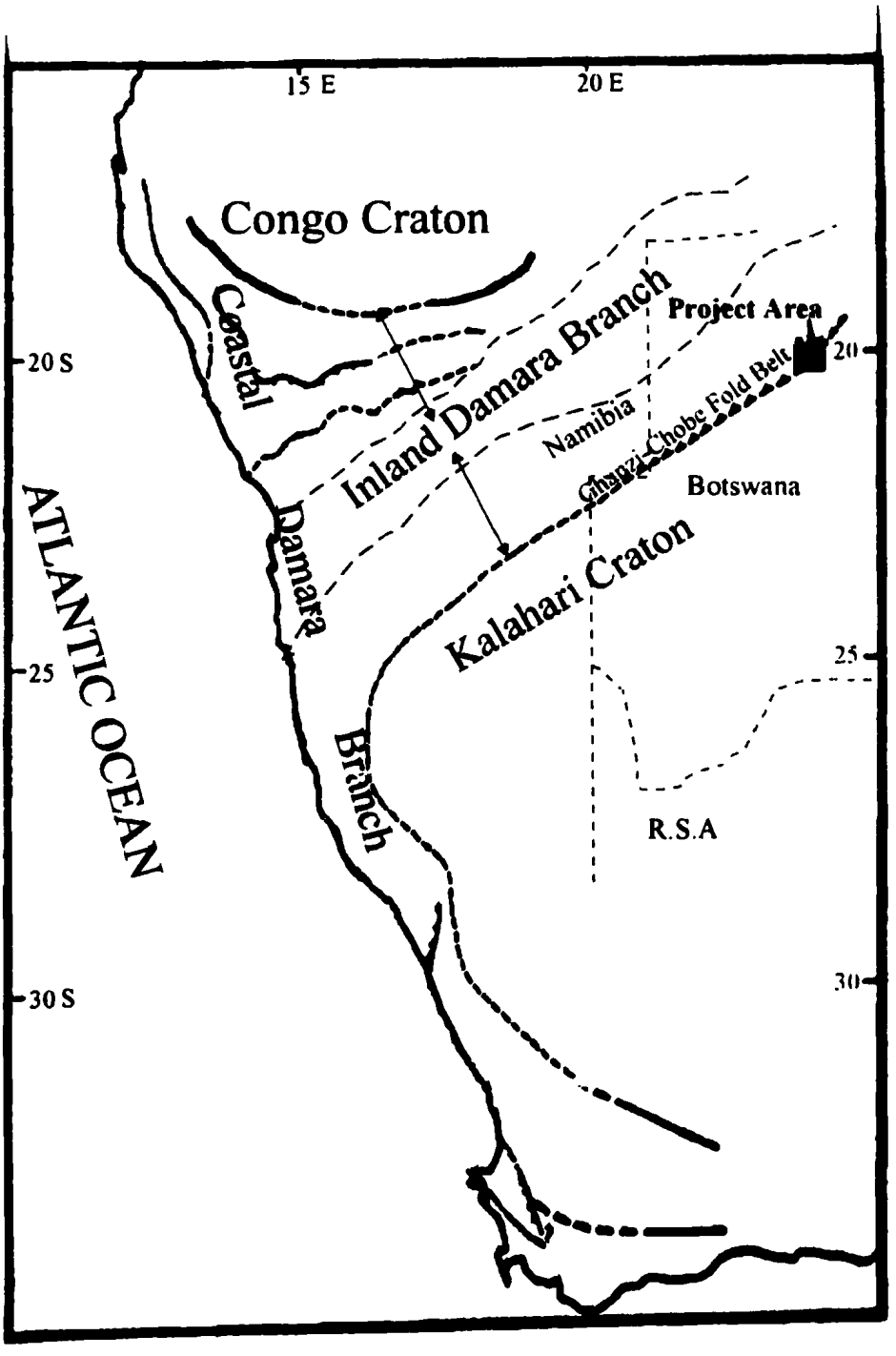

Figure 2.1.1-1: The regional and structural setting of the Damara Province. Adapted from a figure by Hartnady et al., 1985.

2.1.1.1 Nosib Group

Nosib rocks are coarse clastic sediments of continental rift type. Continental rifting is inferred to have begun at 1000-900 Ma with the formation of fault-bound grabens elongated along the strike of the Damara belt. These rift grabens were filled by up to 6 km of clastic sediments of basement provenance. The Nosib grabens are 50-70 km wide and ~200 km long, and all trend to the northeast (Tankard et al., 1982). Syn-rift rhyolites associated with mineralised horizons of fumarolic Fe, Cu, and Zn are found in some of these grabens. Following the end of Nosib deposition, the Damara province developed a dichotomy of depositional environments. A platform Otavi succession accumulated on a subsiding foreland basin on the edge of the Congo craton, and a flysch type clastic succession was contemporaneously accumulated in a deepening trough to the south.

2.1.1.2 Otavi and Mulden Groups

The Otavi group unconformably overlies the Nosib rocks and Archean basement. It comprises a thick shallow marine succession of stromatolitic dolomitic limestones and marls. These sediments are dated at 830-760 Ma. The limestones host some economic Mississippi Valley Type Zn-Pb deposits at Tsumeb, Namibia (Tankard et al., 1982).

The Otavi is overlain by the Mulden group with an angular unconformity. This group consists of clastic basement-derived sediments with carbonate intercalations laid down at ~550 Ma. The succession ends with mollasse type deposition.

2.1.1.3 Ghanzi Group

The Ghanzi group preserves a continental siliciclastic and volcanogenic sequence of middle Proterozoic age (~900 Ma) (Borg, 1988). These rocks outcrop in a 30-40 km wide belt stretching from the Botswana/Namibia border to northeast Botswana, a strike length of ~600 km. Outcrop is intermittent along the belt, separated by areas obscured by Kalahari cover. To the northwest, the Ghanzi-Chobe fold belt is flanked by the Damara Metamorphic belt. The southeastern edge of the belt is inclined to a depth of ~15 km, where it merges with the basement of the Karoo Central basin (Borg. 1988). The Damara orogenic activity imparted to the Ghanzi beds large open folds with axes in a northeast trend. Subsequent Karoo block faulting produced deep graben structures within the Ghanzi group which possibly accumulated Karoo sediments, as at Lake Ngami (Smith, 1984).

The structure and sedimentology of the Ghanzi group have been examined in the vicinity of Lake Ngami by Catterall and Carruthers (1992). The succession consists of a volcanogenic Kgwebe Formation overlain by the siliciclastic Ghanzi Formations.

2.1.1.3.1 Kgwebe Formation

The Kgwebe Formation consists of a folded package of acidic to basic volcanics with some interbedded metasediments. In outcrop, the volcanic rocks are a massive, flow banded feldspar porphyry (Catterall and Carruthers, 1992). The rocks have been petrographically shown to range in composition from rhyodacite to quartz andesite. The Kgwebe Formation contains more basic volcanics near the top. These are largely pyroxene andesite and microdiorite with high iron content. The basic volcanics can be either massive or amygdaloidal, and may contain significant amounts of tourmaline in the latter case. The sediments within the volcanic pile are medium to fine-grained sub-arkose and andesitic tuff.

2.1.1.3.2 Ghanzi Formation

Because of the poor exposure of the Ghanzi sediments, the available information was obtained from logging of drill chips and borehole cores in the area near Lake Ngami (Catterall and Carruthers, 1992). The sediments consist of fine to coarse-grained sub-arkose and arenite with occasional mudflake conglomerate horizons. The arenite contains lithic fragments of deformed granitoid gneiss and hyperbyssal igneous rocks. These sediments, like their Nosib counterparts, occasionally contain heavy mineral laminae with magnetite, rutile, zircon, and tourmaline. The upper Ghanzi beds are divided into a lower "mineralised sequence" and an upper "marker sub-arkose" for mineral exploration purposes (Catterall and Carruthers, 1992).

The "mineralised sequence" consist of grey/green siltstone with a low carbonate content. The latter usually increases towards the base, where a thin limestone may be developed. The siltstone comprises essentially sericite and chlorite with a preferred orientation. These micas enclose opaque sulphide mineral phases including chalcocite, chalcopyrite, bornite, digenite and pyrrhotite. The occurrence of this disseminated sulphide mineralisation has generated enormous economic interest in the Ghanzi-Chobe fold belt stratigraphy. The "marker sub-arkose" is a grey sandstone with pervasive oxidation along fracture zones. The sandstone contains subrounded grains of quartz, feldspar, mica, and accessory tourmaline.

2.1.2 Karoo Supergroup

Slivers of Karoo Supergroup rocks occur in the area south of Lake Ngami and are inferred from borehole and geophysical evidence to overlie either the Damara Supergroup or Archean basement in the Okavango delta (Greenwood and Carruthers, 1973; Hutchins et al., 1976; Reeves, 1978). Stratigraphic boreholes have also intersected Karoo rocks in the northeastern part of the Okavango delta (Meixner and Peart, 1984). The Karoo succession consists of sandstones, shales, coal measures, mudstone, and basaltic lava. The basaltic lava outcrops along the Chobe and Ngwezumba rivers northeast of the Okavango swamps (Smith, 1984).

The occurrence of Karoo rocks in Botswana has been discussed by Farr et al. (1981) and their lithostratigraphy formalised by Smith (1984). The Karoo Supergroup comprises stratiform consolidated sedimentary rocks capped by basaltic lava. They are arenaceous deposits accumulated in a continental environment during the late Palaeozoic to the early Mesozoic. Deposition of Karoo sediments was controlled by a crustal downwarp of the Kalahari craton in the events leading to the breakup of the supercontinent Gondwana (Farr et al., 1981). The sediments were laid down in several sub-basins including the Central, Southwest, Northwest, and Northeast Karoo sub-basins (fig. 2.1.2-1). The Central sub-basin is bound along the northwest by the Ghanzi-Chobe fold belt, on the southwest by the Tshane fault, and abuts against crystalline basement on the remaining

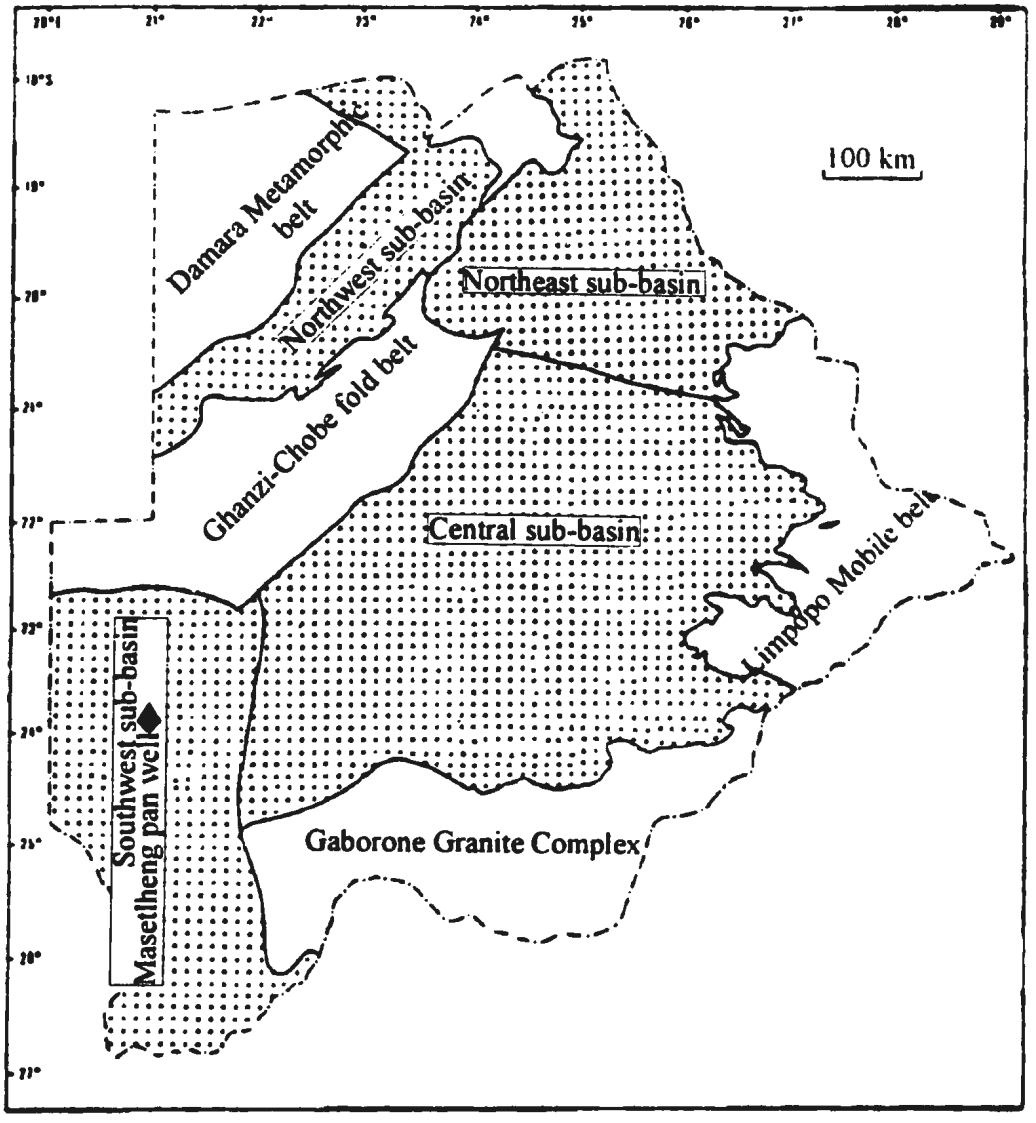

Figure 2.1.2-1: Distribution of Karoo sub-basins and exposed basement in Botswana. After Smith, 1984.

periphery. North of the Ghanzi-Chobe fold belt occurs the narrow graben-like Northwest Karoo sub-basin. It is bounded between the Damara Metamorphic Belt along the northwest edge and the Ghanzi-Chobe fold belt in the southeast. The total thickness of Karoo sediments in Botswana is uncertain, but Farr et al. (1981) estimate a maximum of 1000 m for the Central sub-basin. Stoakes and McMaster (1990) recorded 1162 m at Masetlheng pan during a hydrocarbon exploration campaign in the Southwest sub-basin (fig. 2.1.2-1). The Karoo Supergroup is subdivided from base to top into four groups: Dwyka, Ecca, Lebung, and Stormberg Lava (Smith, 1984). Table 2-2 lists the Karoo units presently known to exist in Ngamiland.

2.1.2.1 Dwyka Group

This deposit is composed of poorly-sorted boulder conglomerates with a gritty matrix. The unit is grey/green and well-cemented, with intercalations of fine green silts. The conglomerate is overlain by black shales and siltstone. The Dwyka group has not been identified in Ngamiland.

Table 2-2: A simplified stratigraphy of the Karoo Supergroup in Ngamiland.

Group	Formation	Lithology
Stormberg	Stormberg basalt	amygdaloidal and massive tholeiitic basalt
Lebung	Bodibeng sandstone	pink to white fine-grained sandstone
	Savuti Formation	varicoloured clays, mudstones, silts
Ecca	Marakwena Formation	angular conglomerates, silts, arkose
	Tale Formation	grey mudstones, cross-laminated sandstone
Dwyka	?	grey to green poorly-sorted conglomerates

2.1.2.2 Ecca Group

The lower Ecca deposits are diachronous with the Dwyka shales and siltstones. They comprise a rhythmically banded siltstone laid down in a lacustrine setting. The Ecca deposits are variable in thickness and distribution, conformable with the Dwyka in some places and overstepping onto basement at the basin margins. The middle Ecca consists of arkosic sandstones which pass upward into fine-grained rocks and ultimately into coal

seams and mudstone. The arkoses are coarse-grained angular sandstones, often weathered to a clay matrix. Their typical graded and/or cross bedding, and the marked angularity, point to deposition under torrential conditions (Farr et al., 1981). The unit contains a basal conglomerate developed where the middle Ecca oversteps onto crystalline basement. The coal-bearing member contains upward and downward fining cycles with sharp boundaries. This is inferred to indicate a deltaic depositional environment (Farr et al., 1981). The coal-bearing strata grade upward to shale coals and finally to mudstone with conchoidal fracture. The upper Ecca argillaceous lithologies in general indicate a fluvio-lacustrine depositional environment, developing from a deltaic/lagoonal facies of the middle Ecca. The upper Ecca strata comprise deeply weathered mudstone and siltstone, lying conformably on the middle Ecca. No great development of the Ecca Group occurs in Ngamiland, but some of its middle formations have been intersected by exploration boreholes at Lake Ngami (Smith, 1984). These deposits have been correlated to the Marakwena and Tale Formations by Smith (1984).

2.1.2.3 Lebung Group

The Lebung Group in Ngamiland consists of the Savuti Formation and the Bodibeng sandstone. The base of the Lebung group is marked in the Central sub-basin by the abrupt disappearance of coal seams and the proliferation of more argillaceous material.

This depicts relatively fast inundation of the Ecca deltaic environment by expanding lakes and/or decreased river grade. The lower Lebung consists of greenish blue siltstone and mudstone with little to no calcareous cement (Smith, 1984). Sedimentation is progressive from the upper Ecca with no hiatus.

2.1.2.3.1 Savuti Formation

This unit represents a dramatic climatic change from the lacustrine environment of the upper Ecca to that of a semi-arid continental environment with variable redox conditions. It is composed of maroon, green, and red mottled mudstone, shales, siltstone, marls, and minor fine-grained calcareous sandstones. These formations have a variable thickness over most of the Central sub-basin. The upper fine-grained sandstone/siltstone unit grades into the overlying Bodibeng sandstone, but at isolated places a thin pellet clay conglomerate marks an unconformity with the Bodibeng sandstone.

2.1.2.3.2 Ntane Sandstone[1] (Bodibeng sandstone)

The semi-arid to arid palaeoenvironment of the Lebung led ultimately to the deposition of fine-grained aeolian sandstones over the former Karoo sub-basins and also directly on the pre-Karoo basement, thus forming the most regionally extensive Karoo unit in Botswana. The Ntane sandstone (Bodibeng sandstone in Ngamiland) is a cream, red, or white, non-micaceous fine-grained, friable sandstone (Farr et al., 1981; Smith, 1984). It is massively bedded, but may contain cross-bedding structures near the top. Though the sandstone is largely aeolian, it contains intercalations of chert, limestone concretions, and red silts, probably derived from intermittent playa or sebkha sedimentation. The Ntane sandstone is a very uniform unit with a variable thickness over most of the Central Karoo sub-basin. This results from the development of an extensive dune field during aeolian deposition. The thermal contact aureole between the Ntane sandstone and the overlying Stormberg basalt sheet is invariably thin and underlain by calcareously indurated sandstones. Since the contact aureole is fractured, it is hydrogeologically significant (Farr et al., 1981).

---

[1]The Ntane Sandstone occurs extensively throughout the Karoo sub-basins. In Ngamiland, it is referred to by its type locality, Bodibeng (Smith, 1984).

2.1.2.4 Stormberg Lava

Karoo sediments are everywhere either partially or entirely covered by extensive plateaux basalt of Mesozoic age. These basalts are found on all the former Southern Gondwana continents including India, Australia, and South America (Petters, 1991). They are a product of the Mesozoic continental rifting that culminated in the breakup of the supercontinent Gondwana. The Karoo basalts of Botswana are phaneritic, fine-grained, grey to purple amygdaloidal and massive tholeiites. When weathered they are a brown, friable rock, easily confused with the basal Kalahari sequence grits and conglomerates. Individual flow banding may vary from one to tens of metres with relatively narrow chill margins (Farr et al., 1981). The basalt may be interbedded with sandstones, siltstone, marls, and palaeosoils. The thickness of the basalt sheet is variable, as it was deposited on an undulating dune field, and also because of the pervasive post-Karoo faulting. In the Northeast sub-basin Farr et al. (1981) estimate the basalt thickness at 400 m, decreasing southwestwards into the Central sub-basin.

2.1.3 Kalahari Beds

As mentioned earlier, the geology of the Okavango region is covered by a thick mantle of Tertiary to recent unconsolidated and semi-consolidated aeolian and alluvial deposits.

Indeed, the Karoo succession occurs mostly under Kalahari cover countrywide. Though the Kalahari sequence has not yet been stratigraphically formalised, it has been amply described from borehole sections at numerous locations over the Central Kalahari basin and also in the vicinity of Maun (Farr et al., 1981; BRGM, 1984; SMEC, 1987). The following description of the Kalahari beds is based largely on the work of the latter two references in the delta region.

Near Maun, the Kalahari sequence is comprised of three main units. At the surface occurs a layer of sandy to silty grey/green clay. It is unsaturated to a depth of ~ 10 m. The clay layer is mainly homogenous, but intercalations of a soft friable sandstone, up to one metre thick, may occur. The underlying formation consists of predominantly grey plastic clay interbedded with several thin beds of silcrete, calcrete, fine sands and silts. The total thickness of these middle Kalahari beds is 30-40 m. The interbedded sandstones contain a limestone cement, and since they are only semi-consolidated, they tend to crumble under percussion drilling conditions (BRGM, 1984).

The lower Kalahari beds consist of a thick semi-consolidated sandstone layer, interbedded with silcrete, calcrete, and clay. This formation was not fully penetrated by BRGM (1984) boreholes but geophysical indications are that it extends beyond a depth of ~ 80 m beneath Maun. The loose sand unit is particularly difficult to penetrate with a conventional drill, since it continuously collapses. Moreover, the thickness of the

Kalahari beds south of the Thamalakane fault known from the sections of boreholes CR2 and CR3 is only 43 and 59 m respectively (Hutchins et al., 1976). These beds are thickened to > 153 m at borehole CR1, north of the Thamalakane fault (see fig. 2.1-1).

2.1.4 Structure

The geological structure underlying Ngamiland defies direct observation because of the mantling Kalahari cover. Geophysical techniques, however, particularly gravity and aeromagnetic surveys, have afforded a reasonable assessment of the structure (Reeves, 1978; Paterson et al., 1979; Reeves, 1979). The aeromagnetic data base compiled and interpreted by Paterson et al. (1979) has been re-examined during the course of the present investigation. These data were re-analyzed with Geosoft® software. Various residual Fourier domain filters were applied to the data in order to enhance primary magnetic trends. The power spectrum obtained via the computation of the various FFT filters was used to estimate depth to magnetic basement following the method of Spector and Grant (1970). The geological structure derived from the re-analysis of the 1978 aeromagnetic data is shown in figure 2.1.4-1 (in the pocket at the back of this thesis).

Ngamiland is underlain by two main structural domains with conflicting strikes. The first domain comprises the Ghanzi-Chobe fold belt, the Damara Metamorphic belt, and the

Okavango rift, with a NE grain. This structural trend is intersected at near right angles by a post-Karoo dolerite dike swarm, with a NW trend. The post-Karoo dolerite dike swarm is 78 km across southeast of the Okavango graben, tapering down to 35 km across northwest of the delta (fig. 2.1.4-1). The dolerite dike swarm emanates from the vicinity of the Nuanetsi-Sabi monoclines ~ 1000 km to the southeast of Ngamiland (Ellam and Cox, 1989). It effectively demarcates the southwest extent of the Okavango rift. Several isolated basic dikes occur to the south of the main swarm, but none have been identified to the north of it (fig. 2.1.4-1).

2.2 Regional tectonics

The African continent consists of discrete cratonic blocks separated by shear zones (Lambiase, 1989). In Southern Africa, the southernmost block, the Kalahari craton[2], is separated from the Congo craton by the throughgoing Mwembeshi shear zone (fig. 2.2-1). This shear zone originates at the Atlantic coast and terminates in the vicinity of the Mozambique belt. The Mwembeshi shear zone is an early Proterozoic zone of crustal weakness which has hosted several Pan-African rifting and orogenic episodes such as the

[2]Kalahari craton includes both the Kaapvaal and Zimbabwe cratons. These cratons acted as a single entity during Pan-African tectonothermal episodes.

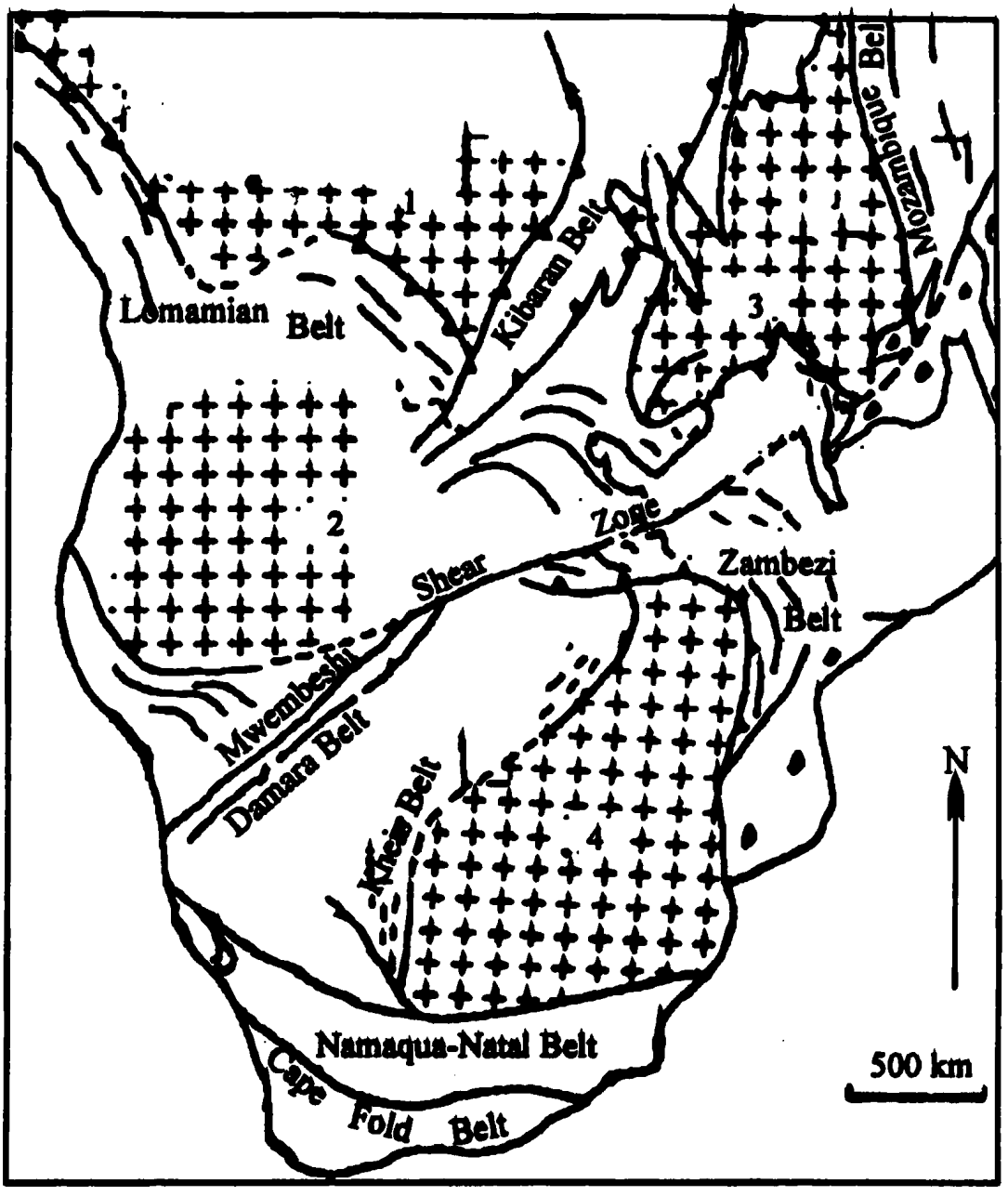

Figure 2.2-1: Tectonic map of southern Africa showing major cratons and mobile belts. The cratons are 1 = Central African, 2 = Congo, 3 = Tanzanian, and 4 = Kalahari. After Pettera, 1991.

middle Proterozoic Ghanzi rift, the late Proterozoic Damara orogeny, the Palaeozoic Zambezi rifts, and the present Okavango rift (Borg, 1988).

The Damara tectonic event (450-1300 Ma), involved initial continental rifting followed by a period of protracted mountain building (Stanistreet et al., 1991). The sediments deposited during the whole cycle are referred to as the Damara succession. Within the Damara succession syn-rift, breakup unconformities, sea marginal, and collisional facies have been identified. Also, geomagnetic array studies have identified a conductive zone at crustal depth underlying the Damara orogenic belt (de Beer et al., 1975). This crustal conductive zone is interpreted to be either a zone of crustal discontinuity with possibly trapped fluid, or a sliver of oceanic crust trapped at the former subduction interface. Furthermore, several early Mesozoic alkaline and ultramafic igneous complexes are situated in the vicinity of the conductive zone e.g. Orapa kimberlite field in Botswana and the Salem Intrusive suite in Namibia (Borg, 1988). The association of upper mantle intrusions with the conductive zone would suggest that it is a deep crustal detachment zone rather than relict oceanic crust.

The Ghanzi succession described in the geology section is on trend with similar middle to lower Proterozoic volcano-sedimentary sequences further to the southwest in

Namibia[3]. Stratigraphic correlation between these "Ghanzi Rift" basins is complicated by the fact that they did not form at exactly the same time, though formed by the same tectonic process. Borg (1988) has shown that the igneous rocks associated with these basins have decreasing age from the southwest to the northeast.

The form, sedimentology, and structural disposition of these basins indicate that they originated in a continental rift environment. The graben structures developed on propagating rifts that started at ~ 1300 Ma at the proto-Atlantic coast, and followed the edge of the Kalahari craton, to reach the Ghanzi-Chobe region at ~ 900 Ma. Borg (1988) argues that the Ghanzi propagating rifts were the initial stages of Damara rifting. It is interesting to note that Nosib sedimentation was contemporaneous with Ghanzi sedimentation (~ 900 Ma). Borg (1988) suggests that at this time, the initial propagating rift system was dying off in the northeast, but a new rifting phase was initiated north of the old one.

---

[3] For instance, the Dorbabis, Witvlei, Klein Aub, and the Sinclair and Koras Groups after an 80°bend in strike at Sesfontein, Namibia (Borg, 1988).

2.3 Hydrogeology of the Okavango

The groundwater table within the Okavango delta is generally shallow. Indeed, it occurs above the ground surface in the perennial swamp in proximal delta areas. The static water level gradually decreases towards the southeast graben-bounding Thamalakane fault zone, falling rapidly thereafter to 910 m above mean sea level (fig. 2.3-1). This is the level of the Makgadikgadi salt pans, the former destination of the Okavango River (Neumann-Redlin, 1980; Gieske, 1993).

The groundwater potential of the Kalahari beds in the proximity of Maun has been summarised by BRGM (1984) and SMEC (1987). The upper Kalahari sequence is predominantly argillaceous and precludes the existence of any major aquifers. The upper and middle Kalahari beds are mainly clays and therefore impermeable to groundwater flow. The fine-grained sandstone intercalations within this sequence are discontinuous and thin. This renders the upper 40-50 m of the beds unattractive regarding long-term groundwater resources. Most of the older boreholes, however, tap water from these beds, with yields of 1.6 to 18 m^3/hr, the latter value obtained where the porosity is enhanced by fracturing (BRGM, 1984).

The lower Kalahari beds present the most prolific potential aquifer. The beds are permeable and somewhat confined by the overlying clays. These beds, however, have

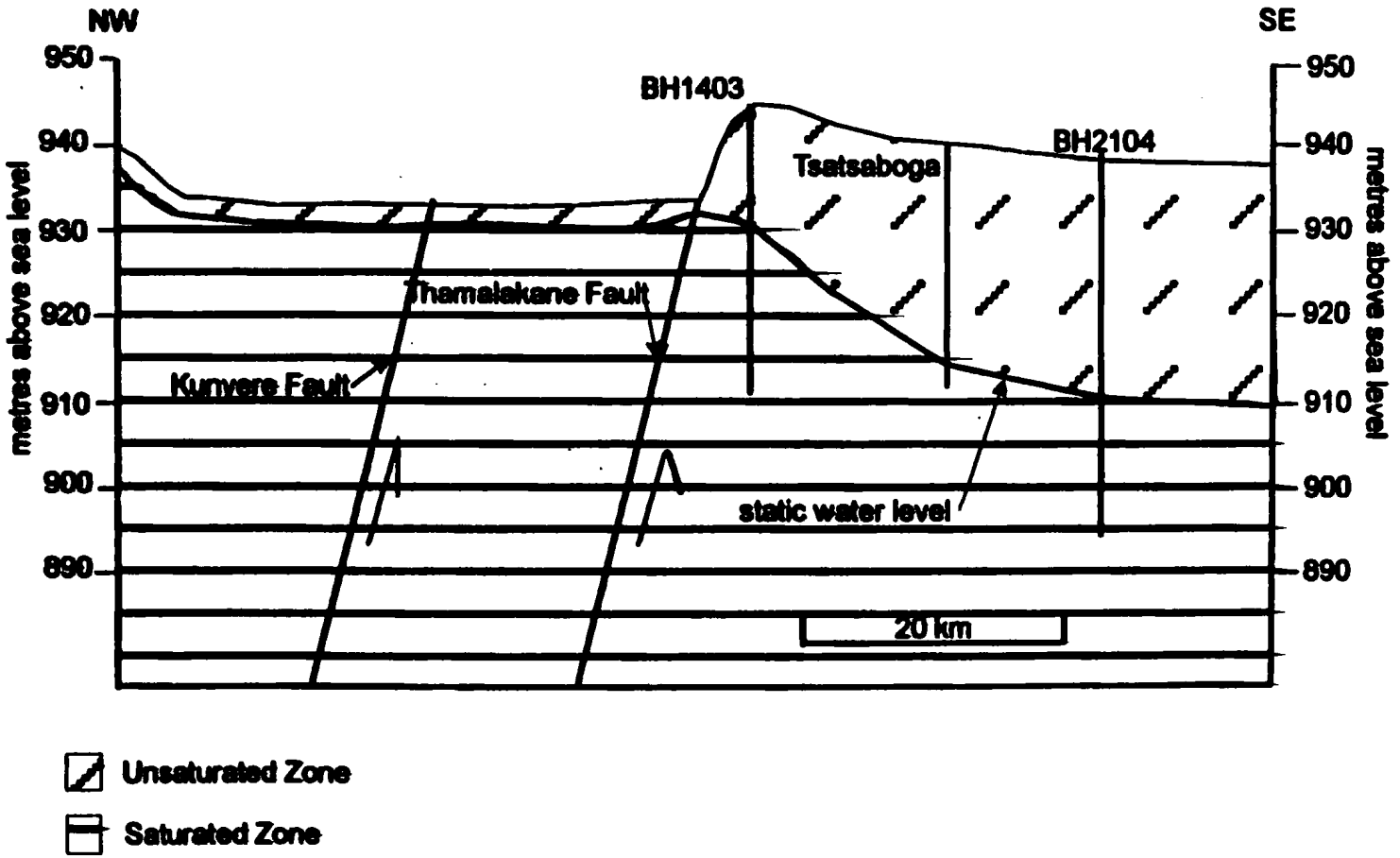

Figure 2.3-1: A hydrogeological transect across the southeast edge of the Okavango Delta. Redrawn from Neumann-Redlin, 1980.

been found to contain saline or brackish water of poor quality (BRGM, 1984). The argillaceous upper Kalahari beds completely prevent flushing and recharge by floodwater into the lower beds. The lower beds thus contain fossil groundwater, as is the case elsewhere in the Kalahari basin (Neumann-Redlin, 1980). It is possible that, since the Okavango area has been affected by pervasive tectonic disruption, the lower Kalahari beds could be displaced into structural dispositions favourable to aquifer flushing and hence recent recharge (BRGM, 1984). The latter consultant did not, however, locate any such structural features, possibly because of the limited scope of the survey and the exploration method employed (dc resistivity).

The present water supply for Maun is dependent on a sandy alluvial aquifer located on the floodplain of the Shashe River southwest of the town. A large, but thin (10 m) sandy alluvium occurs between the confluence of the Shashe and Thamalakane Rivers. Its hydraulic properties have been examined by BRGM (1984) and found to be excellent. This perched aquifer is recharged annually by floodwater in the upper reaches of the Shashe River and hence has good groundwater quality. It is appreciated that since the aquifer is unconfined, and thin, there is a small available drawdown. This requires that many boreholes be constructed to allow large-scale abstraction. The cost would be excessive. Secondly, the aquifer relies on annual recharge by floodwater from the delta. The Shashe River is sometimes dry during drought periods, such as the 1982-87 period (SMEC, 1987). Also, in the long run the alluvial aquifer is prone to nitrate pollution

since it is unconfined and very close to the town. A cross-section across the Shashe and Thamalakane alluvial aquifers is shown in figure 2.3-2.

The problems that surround the Shashe River aquifer warrant consideration of an alternative aquifer resource. Therefore, one considers the Karoo sequence, for reasons outlined in the geology section. Because the existence of Karoo beds in Ngamiland is at most speculative, their hydrogeology has not been directly investigated. However, the hydrogeology of the Karoo sequence has been studied extensively elsewhere in the Karoo sub-basins (e.g. Farr et al., 1981). As is the case in the Lake Ngami area, at least thin Karoo beds may be preserved in fault grabens in the Maun area.

That Karoo beds are stratiform, unmetamorphosed, and laterally extensive, make this sequence the most hydrogeologically important in Botswana (Farr et al., 1981). In particular, the Ntane sandstone, confined between the Stormberg lava sheet and the argillaceous middle Lebung hold considerable groundwater potential. The thickness of the Ntane sandstone in the Central sub-basin is 100 to 130 m. The contact with the overlying basaltic lava is fractured and weathered, making it an extension of the sandstone aquifer.

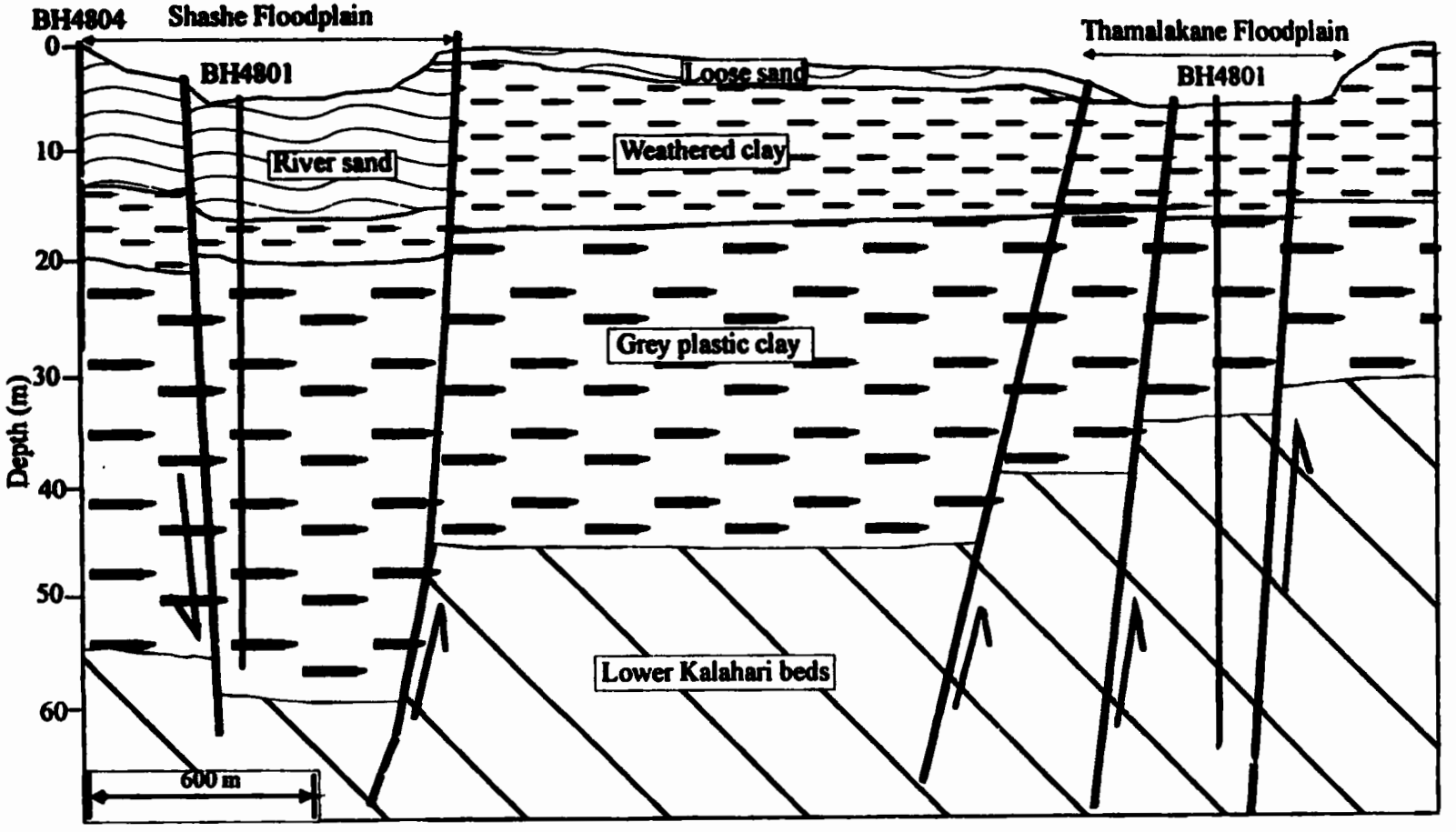

Figure 2.3-2: A NW-SE transect across the Shashe and Thamalakane river floodplains. The faults were mapped by BRGM (1984), using electrical resistivity.

Productivity of the Ntane sandstone aquifer has been assessed in the Central sub-basin by Farr et al. (1981). The specific capacity calculated from field observations is 14.7 m^2/day. It was found to vary both laterally and vertically due to corresponding facies variations. The transmissivity determined from pumping tests was in the range 10-35 m^2/day. There was a marked vertical variation in transmissivity, which was thought to indicate that the Ntane sandstone transmits water through intergranular flow (Farr et al., 1981). The confined storage is 0.0001-0.0008[4]. This is a high aquifer storage value, and it suggests that the aquifer is not likely to de-water during pumping. The sandstone has a porosity of 25-30%, and a permeability of 0.36-1.4 m/day. These parameters, though quantified in a different sub-basin, are likely to exist in the Ngami sub-basin because of the great uniformity of the Ntane sandstone (n.b. it is here called Bodibeng sandstone). The above-mentioned parameters were found to decrease with increasing depth, perhaps due to an increase in cementation. The calculated transmissivity and storage values indicate an aquifer of the highest performance anywhere within the Karoo succession (Farr et al., 1981).

Recharge conditions of the Karoo aquifers are at present unknown in the delta. Since the tectonic event that formed the delta is quite recent, it may be appreciated that in the former times Karoo aquifers discharged groundwater towards the Makgadikgadi basin, to the southeast of the delta. Subsequent to the formation of the delta, the groundwater

---

[4] Note that aquifer storage, or storativity, is a dimensionless quantity.

system was disrupted by graben subsidence. However, the sandstone aquifer at present may contain fossil groundwaters. Some recent recharge is also possible through fracture zones within the delta.

2.4 Summary

Ngamiland is underlain by Archean granitoid gneisses juxtaposed with Damaran rocks. The latter comprise the Ghanzi-Chobe fold belt in the south and the Damara Metamorphic belt in the north. Both fold belts are intruded by hyperbyssal igneous bodies. The northeast structural trend of the Damara is intersected by a northwest trending dolerite dike swarm of Mesozoic age. This basic intrusion is believed to be related to post-Karoo continental rifting.

The basement complexes are inferred to be overlain by at least the upper units of the Karoo Supergroup, including the Stormberg basalt and the Lebung Group. The latter group contains the potential Karoo aquifers which are the target of the present investigation. Surficial deposits over Ngamiland include the Kalahari sands and Okavango fluvial beds. The upper Kalahari beds are mostly impermeable while the lower beds contain saline groundwater. Very little is known regarding the groundwater potential of the Okavango beds, but a large number of boreholes within the delta contain saline

water. For these reasons, the surficial deposits present a poor potential target for extensive well field development. Exceptions may occur where gravel and sand aggregates form perched aquifers, such as the Shashe River sand.

Pan-African tectonic events were controlled by pre-existing zones of crustal weakness. In particular, the Mwembeshi shear zone controlled the Damaran episode, and perhaps also the present Okavango rift development. The Damara province is underlain by a conductive zone at crustal depth. Moreover, the associated sediments occur in NE trending grabens believed to be relict propagating rifts.

3.0 PREVIOUS GEOPHYSICAL WORK

The Okavango delta has been investigated by gravity, aeromagnetic, seismicity, seismic refraction, electrical and electromagnetic techniques (de Beer et al., 1975; Greenwood and Carruthers, 1973; Scholz, 1975; Hutchins et al., 1977; Reeves, 1978; Paterson et al., 1979; BRGM, 1984; Ludtke, 1986; and Koosimile, in preparation). Investigations were in most cases intended to reveal the geological structure and stratigraphic relationships otherwise obscured by Kalahari cover. Geophysical information from the potential field methods reveals the northeast-southwest regional trend but cannot provide detail on a local scale due to their inherent ambiguity in interpretation. The paucity of borehole sections makes calibration of the potential field data difficult.

Greenwood and Carruthers (1973) carried out seismic refraction experiments aimed at providing control for the National Gravity Survey in progress at the time. Refraction profiles were run at the few available stratigraphic boreholes (CR1-CR5, see fig. 3-1) to determine horizontal seismic velocities of the lithologic units encountered. Seismic refraction, detailed gravity, and magnetic profiles (in the same programme) were run at various locations across the fault zone bounding the Okavango delta in the southeast (Thamalakane and Kunyere faults). A few profiles were run in the interior of the delta to determine the maximum thickness of the Kalahari and alluvial deposits. The seismic refraction experiments of Greenwood and Carruthers (1973) were successful in delineating the detailed geological structure across the Thamalakane and Kunyere fault

zones. The experiments identified and delineated the topmost unit of the Karoo Supergroup, the Stormberg basalt. It was not possible to map the underlying Bodibeng sandstone since it has a lower seismic velocity than the basalt above it. Hence it was not even possible to determine the thickness of the presumed basalt sheet. The Kunyere fault was found to have a northwest throw of ~250 m at Marophe, the site of the present seismic reflection survey. A location map for the 1973 refraction survey is shown in figure 3-1.

Control seismic refraction experiments at boreholes CR1-CR5 established horizontal seismic velocities for the formations encountered. A surface layer composed of loose sand and soil has a seismic velocity of 0.4-0.8 km/s. This is underlain by Kalahari sediments with a velocity of 0.8-2.0 km/s, the exact value being governed by the relative amounts of sand, crete, and clay. Karoo basalt has a seismic velocity of $\geq$4.0 km/s. The basement complex in general shows velocities in excess of 5.0 km/s. The refraction profiles across the Thamalakane fault indicate a northwest throw of 50 m at line C and 200 m at line D respectively. The Kalahari beds rest directly on basement at line D (fig. 3-1). There exists a thick layer of Karoo basalt on the upthrown block at line C. Whether this basalt overlies Bodibeng sandstone could not be established from the seismic refraction results.

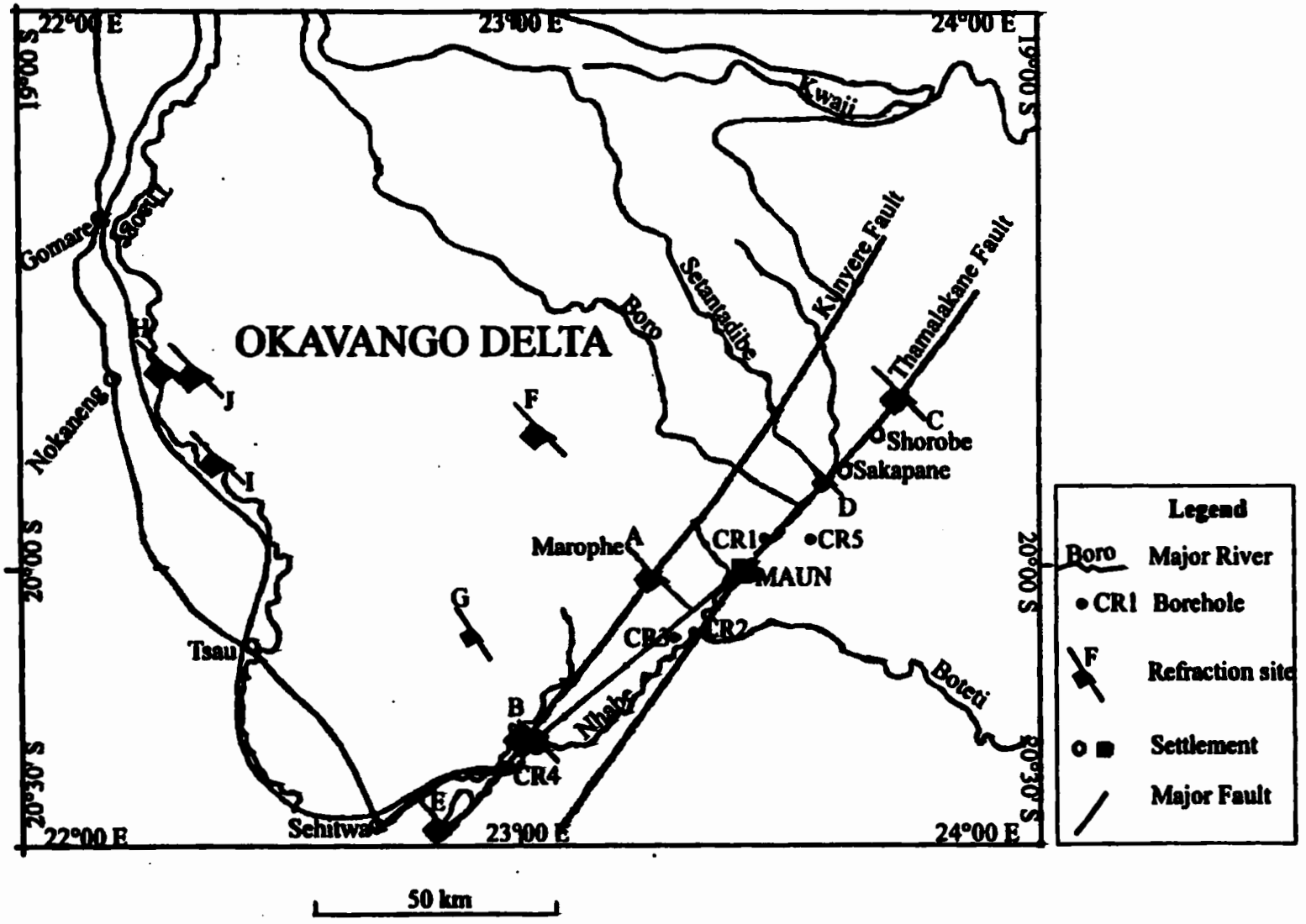

Figure 3-1: Map of the Okavango Delta showing the main fluvial systems. The 1973 seismic refraction sites A to J are shown.

Seismic refraction line A, at Marophe, partially coincides with the present reflection profile. It therefore provides a useful reference in the interpretation of the seismic reflection section. The profile shows a smooth gently dipping base to the Kalahari beds (1.8 to 2.0 km/s). The strata are downfaulted to the northwest, and displaced by ~250 m. The faulted structure is also indicated by the gravity and magnetic profiles (fig. 3-2).

Scholz (1975) undertook a micro-earthquake study in the Okavango rift zone to assess the rate of seismic activity and its associated hazard in the Maun region. Focal mechanism solutions from this study indicate nodal fault planes dipping at 60° to the northwest along the Thamalakane and Kunyere fault zones. These fault planes indicated active seismicity of at least four events per year. The study concluded that the Okavango region is presently undergoing active crustal subsidence with total cumulative displacement of 100-200 m along the Thamalakane and Kunyere fault zones. Scholz (1975) argues that the desiccation of the once extensive Lake Makgadikgadi in recent times is directly related to faulting in the Okavango, thereby damming the main water supply behind the rift graben. Seismicity observations in the Okavango, and further northeast in the Luanga rift, indicate that the East African rift system bifurcates south of Lake Tanganyika (Tanzania). The southwestern arm of this rift then propagates towards the Atlantic Ocean, and is presently within the Okavango rift zone (Scholz, 1975).

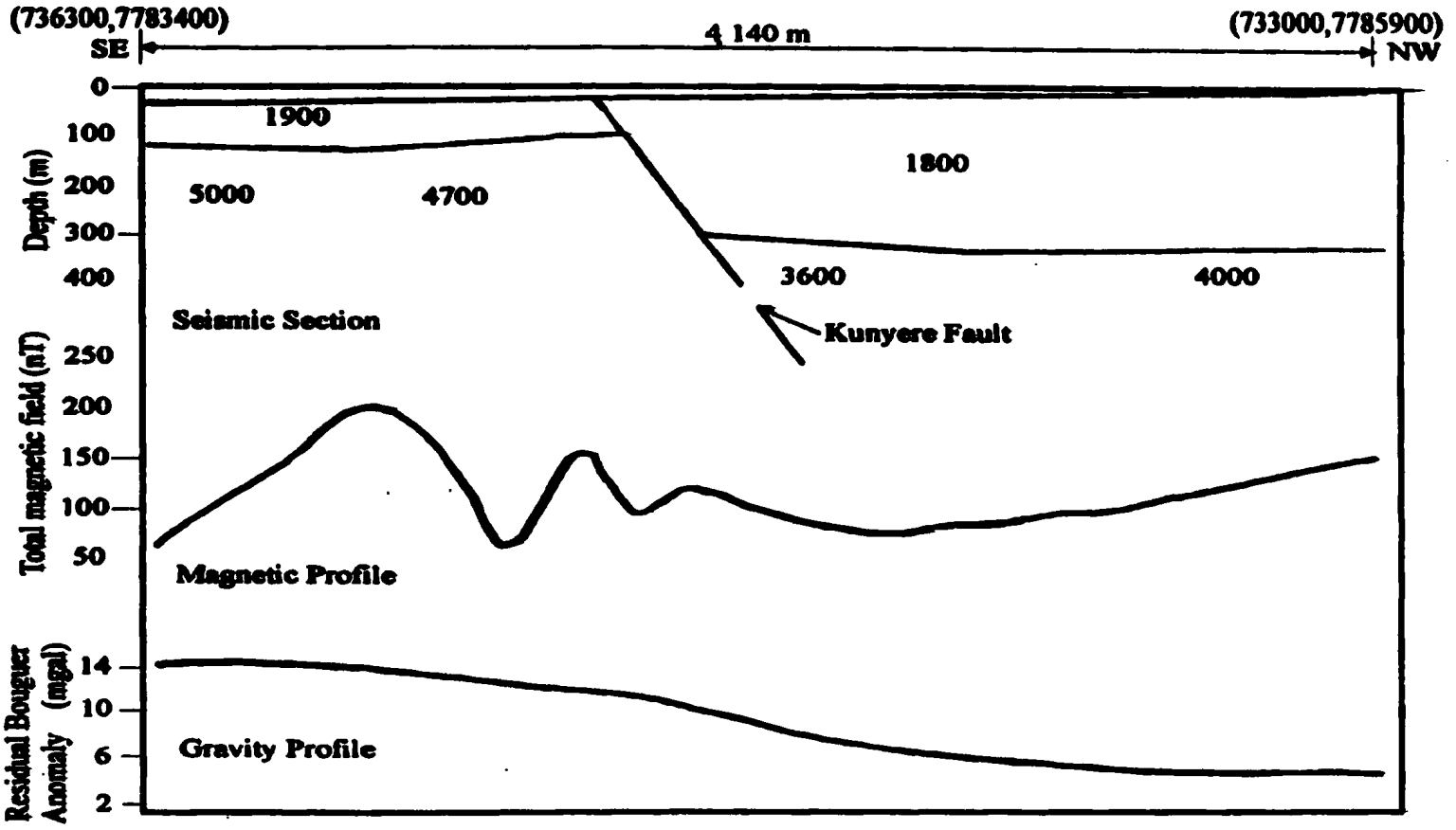

Figure 3-2: A seismic section from the 1973 refraction line at Marophe. The numbers indicate measured seismic velocities in m/s. UTM ground co-ordinates are indicated at the top. After Greenwood and Carruthers, 1973.

From magnetometer array studies, de Beer et al. (1975) delineated an electrical conductivity anomaly at crustal depth below and parallel to the present Okavango rift. This crustal conductor can be traced from the Atlantic coast, across Namibia, through the Okavango, and continues northeastwards to join the East African rift system. Geomagnetic induction anomalies are normally associated with either elevated upper mantle temperatures (partial melts) or a deep crustal fracture zone trapping fluid at depth. de Beer et al. (1975) propose the latter cause due to the observed graben formation (brittle failure) and the absence of a known thermal anomaly in the area. Moreover, the fact that the fracture zone fortuitously follows very closely the trend of the Pan-African Damara orogeny may indicate a re-activation of the Ghanzi rift.

Deep Schlumberger electrical soundings were conducted over the Okavango delta by Hutchins et al. (1977) to determine depth to resistive basement and the possible presence of Karoo beds beneath surficial cover. Interpretation of the resulting sounding curves was limited by lack of sufficient geological control but the results were in fair agreement with the seismic refraction results of Greenwood and Carruthers (1973). One such electrical sounding was conducted at Marophe, on the seismic refraction line, just north of the Kunyere fault. The sounding curve at Marophe (fig. 3-3) depicts a five layer electrical model comprising a resistive surface layer underlain by layers of alternating low and high resistivity. These lower layers are very conductive at 1.2-4.2 Ω-m. The resistive

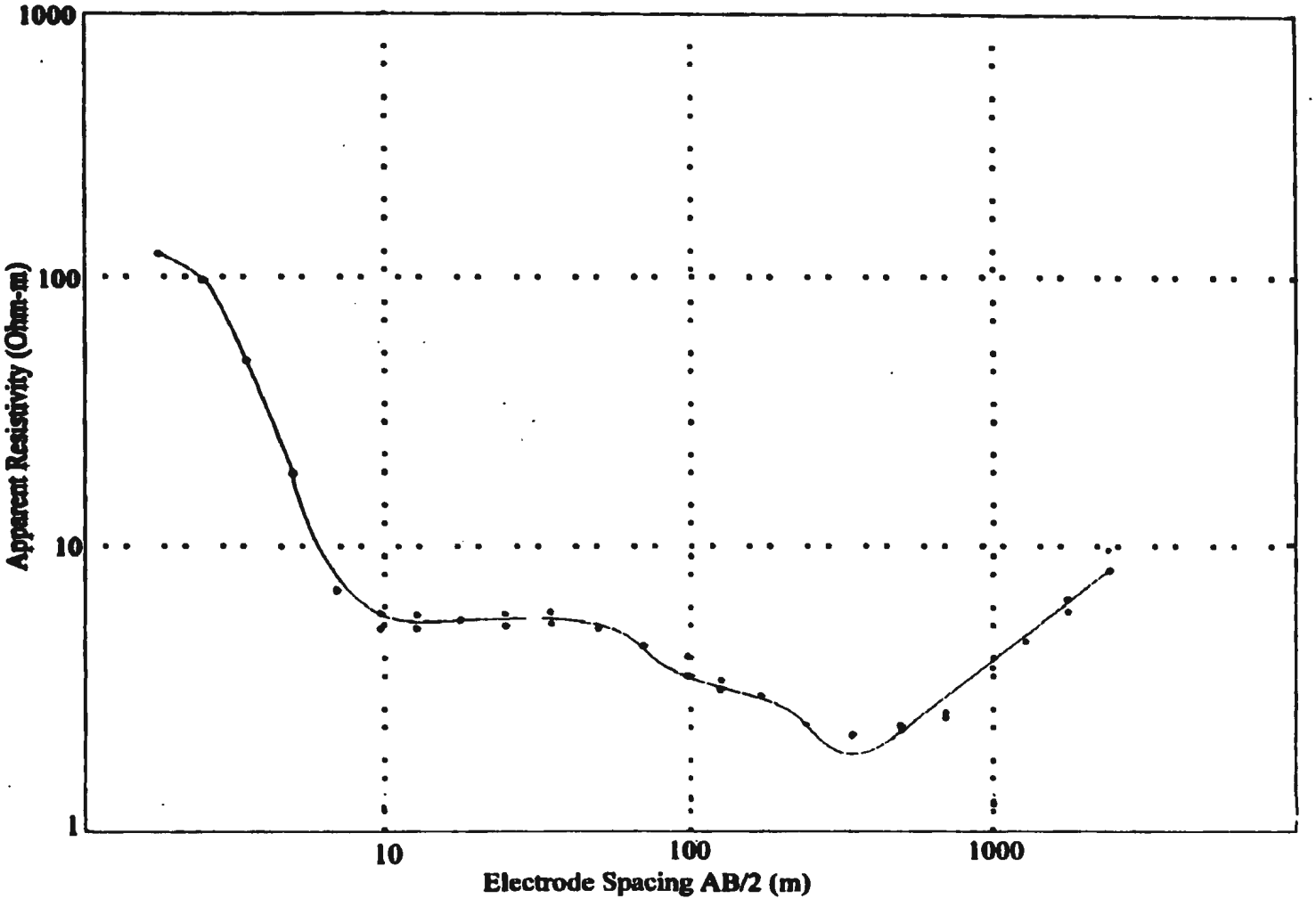

Figure 3-3: Results from an electrical resistivity sounding conducted at Marophe. After Hutchins et al., 1977.

basement is indicated at ~438 m depth. A geological interpretation for the sounding is given in Table 3-1.

Table 3-1: Interpretation of a Schlumberger electrical sounding at Marophe. After Hutchins et al. 1977.

Apparent Resistivity (Ω-m)	Thickness (m)	Interpreted Lithology
270	2	dry sand
4	27	saturated sand, clay
2.4	118	brine-saturated sand, clay
1.2	203	clay
4.2	88	fresh water sandstone

The geological interpretation in Table 3-1 shows that sediment thickness north of the Kunyere fault is at least 438 m. The sediments include ~350 m of Kalahari and Okavango beds overlying ~88 m of Karoo sandstone. Although the presumed Karoo

beds show a somewhat low resistivity (4.2 Ω-m), it is considered that since they are overlain by a thick conductive layer, their apparent resistivity is significantly suppressed.

3.1 Summary of the current exploration status

The previous chapters present the state of knowledge regarding the geology, stratigraphy, and structure of the Okavango area. It is apparent that the regional geology and structure is relatively well-constrained. On the local scale, however, the state of geological knowledge is severely limited. This situation is caused primarily by the presence of brine-saturated semi-consolidated Kalahari sands over the basement, which limits the penetration depths of electrical and electromagnetic methods. Gravity and aeromagnetic surveys have so far been carried out only at a reconnaissance scale. Electrical resistivity and time domain electromagnetic surveys in the vicinity of Maun have established the stratigraphy of the upper and middle Kalahari beds to a depth of ~80 m (BRGM. 1984, Koosimile, in preparation). The total thickness of the Kalahari and the layering of the lower Kalahari beds is still unknown since these methods cannot penetrate deep enough. Deep electrical resistivity soundings give an indication of the depth to basement in the Marophe area (Hutchins et al., 1977). The logistical and financial requirements for the deep electrical sounding effort turned out to be excessive for mapping purposes.

The seismic refraction experiments of Greenwood and Carruthers (1973) achieved some success in measuring depth to basement and fault displacements across the Thamalakane and Kunyere faults. These experiments, however, could not measure the thickness of the Stormberg basalt where it overlies Karoo sandstone since refracted arrivals are produced only when the lower horizon has a higher seismic velocity. A velocity inversion (i.e. a velocity decrease with depth) is expected in the area if the stratigraphy includes Karoo beds as indicated by gravity and scattered borehole evidence. It is this fact that prompted the use of the seismic reflection method to map the geology over the basement of the Okavango. This method is not affected by either the presence of saline groundwater or a velocity inversion.

Geophysical exploration is employed in groundwater studies to maximize the success rate of aquifer location, and thus substantially to reduce the cost of drilling. Groundwater exploration in the Okavango has until recently been dependent on electrical and electromagnetic surveys and also wildcat drilling. The latter geophysical methods have identified shallow aquifers perched on the impermeable middle Kalahari beds (e.g. the Shashe River aquifer). These aquifers are invariably thin and as such cannot provide a reliable long-term groundwater resource. Furthermore, the aquifers are prone to nitrate pollution since they are unconfined. Wildcat drilling is not favourable because of its low success rate and excessive cost to the exploration effort. The high number of dry and saline boreholes around the Maun area attest to this fact. The foregoing discussion

indicates that a somewhat more robust geophysical method is required to explore the Kalahari beds more thoroughly and also to investigate the possible existence of Karoo aquifers below the Kalahari cover. The seismic experiment discussed in the following chapters was designed to meet this end.

4.0 DATA ACQUISITION AND PROCESSING

4.1 Acquisition Overview

Many geophysical surveys have to date been carried out to discover groundwater resources for the town of Maun with marginal success. The details of the pertinent geophysical surveys carried out in this regard were discussed in chapter 3. It suffices to say here that it is now clear that a more robust geophysical technique is required to locate new groundwater resources for the town. The seismic refraction survey (Greenwood and Carruthers, 1973) established a possible presence of Karoo basalt at some locations on the Thamalakane and Kunyere fault zones. The thickness of these basalts, or whether they are underlain by Karoo sandstones was not determined by the refraction survey because of the hidden layer problem. The present seismic reflection survey was conceived to extend further the refraction findings and possibly locate potential Karoo sandstone aquifers in the area.

Seismic reflection profiling is suited to explore for groundwater around Maun because of its insensitivity to the limiting factors of salinity and velocity inversion. It is, however, susceptible to cultural noise such as traffic vibrations and electricity. The presence of these noise sources in Maun excluded the town and immediate surroundings as a possible prospecting target, although the sought stratigraphy and structure may underlie the town. This notwithstanding, the prospective survey sites have to be located close to the town

to avoid high haulage costs if new resources are found. It was found that the residual Okavango flood wave was arriving on the Thamalakane River at the beginning of the survey period. This reduced the possible targets only to the Kunyere fault zone to the west of Maun. All areas to the north and northeast of the town would be flooded at this time. The desired seismic profile was eventually sited across the Kunyere fault zone at Marophe (fig. 4.1-1). There was already an existing cut-line at this location utilized previously for the seismic refraction experiment, and also a deep electrical resistivity sounding. The results from these surveys gave a fair idea of the expected ground conditions and helped in the survey design discussed in the following section.

4.1.1 Acquisition strategy

We have learnt in the previous sections that the present well field for Maun is a perched sand aquifer ($\sim$ 10 m thick) in the Shashe River, and also that thin ($\sim$ 1 m) sandstone aquifers occur within a clay sequence. The sandstone aquifers are discontinuous, and terminated by faults. It is expected that these faults may displace the lower Kalahari beds into structural dispositions favourable to flushing and hence freshwater recharge. It is the intention of this survey to locate such fault displacements. At present the perched aquifers are not adequate to meet the water demand for the town. These aquifers therefore set the

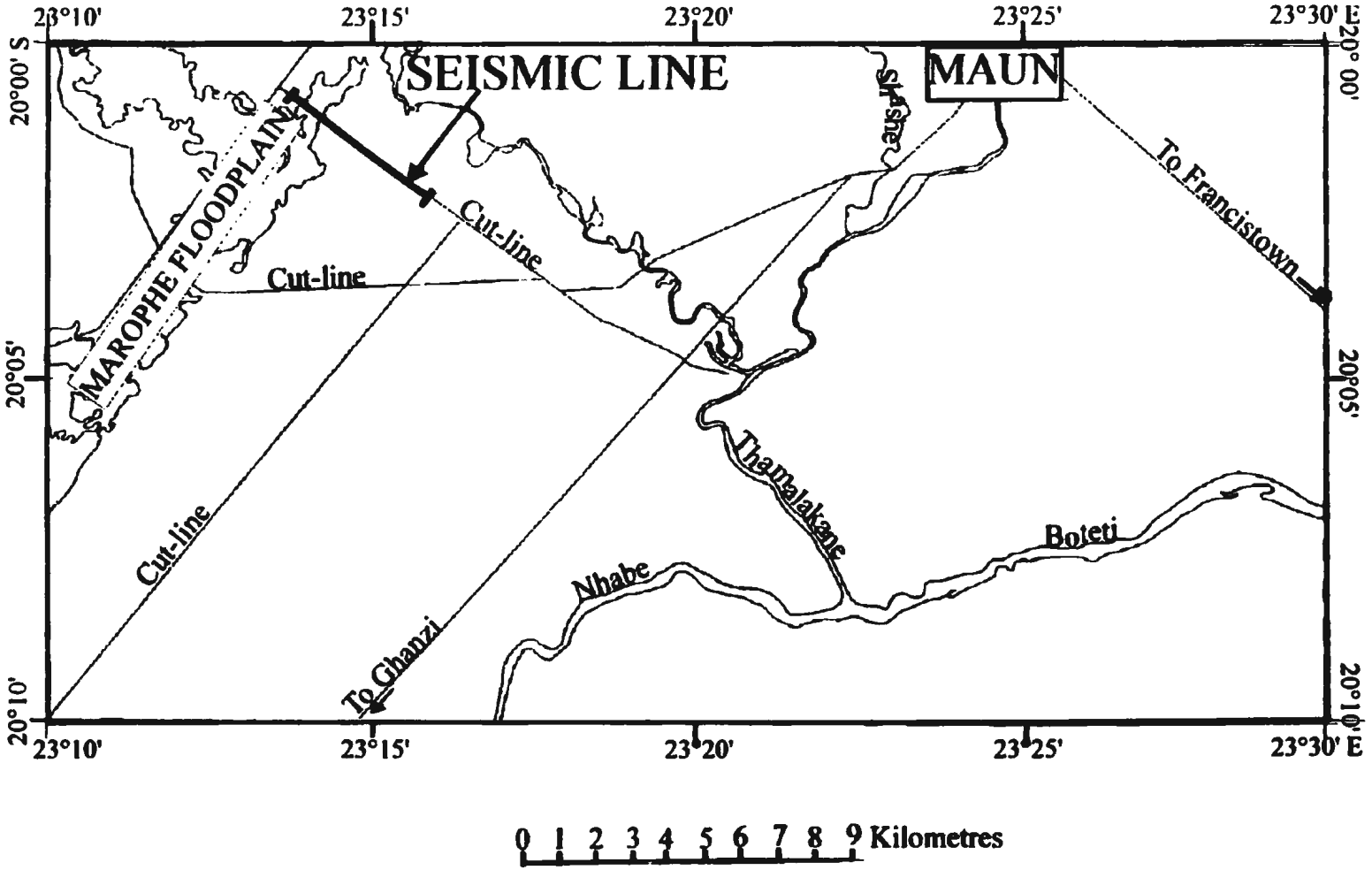

Figure 4.1-1: Site map showing the location of the seismic line with respect to Maun. The main drainage system is shown. Note that the Nhabe river flows to the west, and the Boteti to the east after the division of the Thamalakane.

minimum size of usable aquifer targets. On the other hand, the Karoo basalt and sediments may be hundreds of meters thick. The sediment thickness at Marophe was determined from an electrical resistivity sounding to be ~438 m. The sediments thicken to the northwest, implying a dipping basin edge. The seismic velocity for the Kalahari sequence was found to be 1800-1900 m/s (fig. 3-2) by the refraction survey of Greenwood and Carruthers (1973).

Given these ground conditions, one needs to design a seismic reflection survey suitable to detect the smallest aquifer thickness at ~1 m and also the deepest horizon at ~380 m (fig. 3-2). The design of optimum field acquisition parameters involves consideration of the required recording time, target depth, and the target seismic velocity (Anstey, 1986). Values for these quantities were obtained from records of previous investigations. The required spread length (x) was then determined from the reflection travel time equation;

$$x=\sqrt{(t^2v^2-4z^2)} \qquad (1)$$

where t,v, z, are the target time, velocity, and depth. Substituting anticipated values for the present survey, one gets x ≈ 482 m.

Once the optimum spread length was known, the Common-Midpoint (CMP) interval was calculated by consideration of the target frequency (f_{max}) required to avoid the shortest

wavelength (λ) surface waves. The refraction survey established a weathered layer velocity of 400-800 m/s. The receiver station interval was determined from the equation (Graebner, 1960);

$$\lambda = \frac{v_{min}}{f_{max}} \qquad (2)$$

At a target maximum frequency of 40 Hz, (2) gives a receiver interval of 10.0 m. This would give a CMP sampling interval of 5.0 m. The receiver interval should accommodate the maximum possible reflector dip to avoid spatial aliasing. The required number of recording channels N is calculated from;

$$N = \frac{x}{\lambda} \qquad (3)$$

and the fold of coverage is given by N/2 = 24, since the CMP and receiver interval are equal for a symmetric split spread. It was decided (from substitution in (3)) to use 48 recording channels for the survey. The source interval in high resolution surveys should always equal the receiver interval (Anstey, 1986).

The choice of a signal source is determined by the cost, required frequency bandwidth, portability, and the amount of power needed for maximum penetration. Surface sources are preferred for high resolution surveys since they are highly mobile. The main problem is that surface sources generate strong surface waves which degrade the data signal to

noise ratio. A Betsy seismic gun was chosen for a signal source because it has a broad frequency bandwidth and adequate energy to reach the anticipated depth.

4.1.2 Field Procedure

The first field day was spent on a reconnaissance survey to locate the position of the profile on the ground with topographic maps and GPS (Global positioning system) navigation. The prospective sites were visited and assessed for access. It was decided at this point that only one seismic reflection profile, across the Kunyere fault and along the 1973 refraction cut-line, would be carried out. A profile across the Thamalakane fault could not be surveyed since the Thamalakane River was in flood at the time. Moreover, the Maun-Ghanzi highway runs parallel to and close to the river, so that traffic noise could degrade data quality. The reflection line was commenced from the northwest, 14.3 km from the highway, and carried on to the southeast along the cut-line. The equipment used for data acquisition is listed in Table 4-1.

Table 4-1: Field equipment used to acquire seismic data at Marophe

Item	Type	Quantity
seismograph	Bison 9000 A	1
seismic cables & accessories	Mark products, 48 channel 96/48 channel roll-along	2 1
receivers	Mark products, 40 Hz geophones	96
data storage media	1 Gb optical disc	1
signal source	Betsy seismic gun 1000 12 gauge shells	1
survey equipment	tilting level, 2 stadia	1
GPS	Magellan NAV 5000	1
communication	Motorola, portable short wave radios	2
computer	80486 PC	1
transport	off-road vehicles	2

Once the location of the profile was ascertained, the crew went on to flag the line at 9 m intervals[5]. It had been decided during the survey design to use 10 m station spacing, but since a smaller station spacing meant increased resolution, it was decided to proceed at 9 m station interval. Shot holes were dug midway between receiver points, since a split spread geometry had been chosen to maximize the fold of coverage. A symmetric split spread is also required to asses the amount of reflector dip so that adjustments can be made if the dip is found to be large. The shot holes were used to improve coupling of the signal with the ground. Preparation of the shot holes was slow due to the presence of clayey soil. The situation improved further down the line where the ground comprised loose sand.

The line was set up in a symmetric split spread, after which the survey proceeded following a standard roll-along fashion. The record length was 1000 ms at 0.5 ms sampling rate. This gives a Nyquist frequency of 1000 Hz. A printout of the shot records was produced periodically in the field to assess the signal to noise ratio (S/N) of the data. It was decided after the first recording day that the signal source was rather weak and thereafter two shots were stacked at each shot point. A comparison of the field records for the two periods is shown in figure 4.1.2-1. Although this procedure increased the signal to noise ratio, it meant that the anticipated length of profiling could not be

[5] The seismic cable was only 9.90 m between the takeout points when fully stretched.

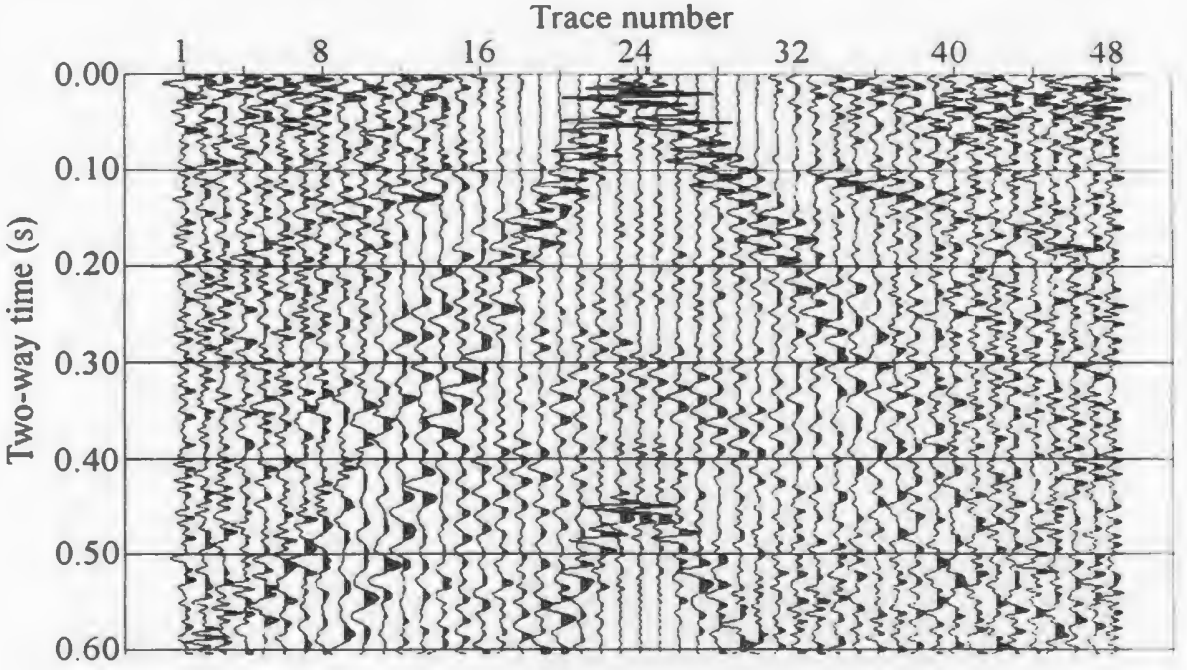

(a) Shot 1345

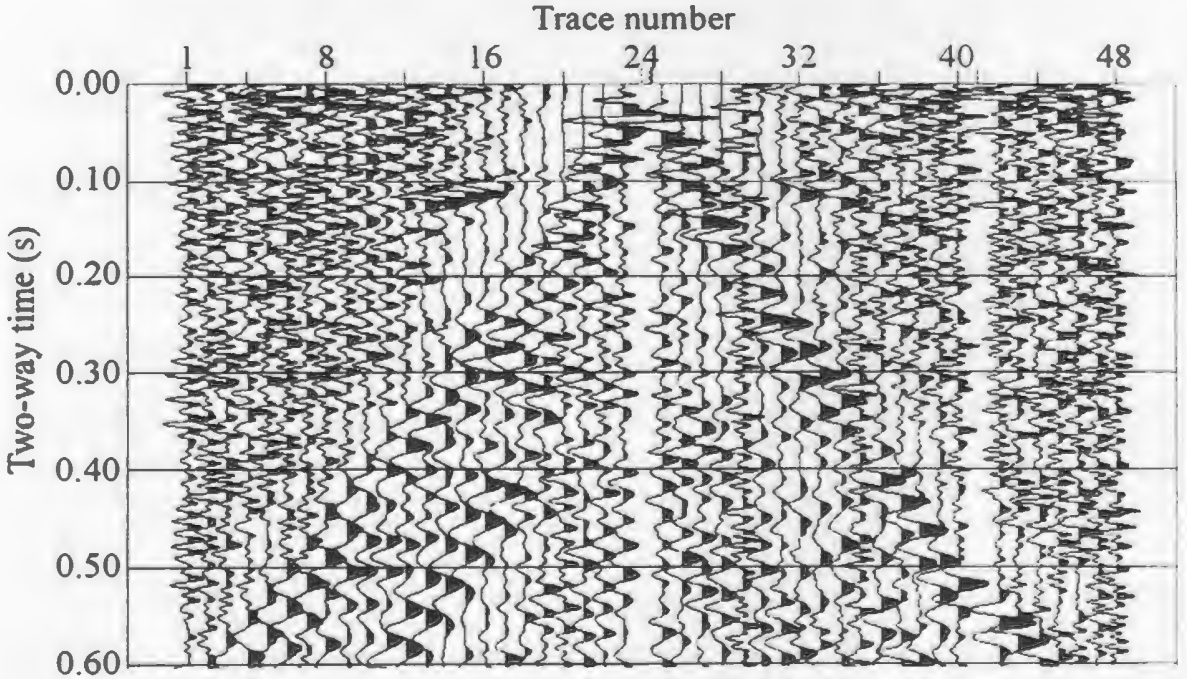

(b) Shot 1875

Figure 4.1.2-1: Field shots recorded with one (a) and two (b) stacked shots. The records were amplified using a 200 ms AGC time gate, and filtered at 15/20-120/140 Hz Note that deeper reflection events are visible in (b) e.g. at 0.30 s.

reached, as the budget for shot shells was exhausted. One alternative would be to increase the station interval, but this would degrade the resolution of the survey. Moreover, it was apparent from the rate of progress that the anticipated length of profile ($\sim$ 10 km) could not be reached given the time constraint. The final length of profiling accomplished was 4 452 m. The shooting and recording was followed at the end of each day by surveying and levelling that portion of the line already covered. The flagging tape was then picked up, leaving the site in its original condition. The acquired data was downloaded to the optical disk for storage each evening.

Some operational problems were encountered with the roll-along wherein there appeared to be a gap in the live channels. Attempts to fix this problem met with failure after disassembling the instrument several times. A second recording problem was caused by the trigger switch which failed to set the seismograph on when the Betsy was fired. After futile attempts to fix the trigger, it was decided to use a geophone as a trigger. This worked well and recording progress was accelerated.

Precautions were taken during data acquisition to avoid recording during strong wind gusts in order to avoid low frequency noise. The data was examined in Vista 6.6 each evening to assess noise levels and apply some preliminary filtering tests.

4.2 Processing Overview

The aim in processing seismic reflection data is to enhance the signal to noise (S/N) ratio so that structure is clarified on the seismogram. Noise removal is achieved through different filtering processes, the most important of which is the summing of adjacent traces in such a way that noise events interfere destructively. This process yields a stacked trace with improved S/N ratio. Before data can be stacked, it is necessary to apply dynamic and static time corrections to reduce all the traces to zero-offset time. These latter corrections involve refraction statics and velocity analysis, discussed in the following sections.

Reflection seismic data processing described above is concerned with the enhancement of only reflected events on a seismogram. The data, however, contains direct and refracted arrivals obtained from the weathered layer. Analysis of these first breaks provides a near-surface velocity model for the line, which cannot be otherwise obtained from reflected arrivals. First break energy is removed prior to stacking since it may introduce artifacts into the stacked section.

4.2.1 Hardware and Software

A suite of different computer systems and software applications was used at various stages of processing the present data set, to achieve specific processing objectives not easily met by a single software suite. The process involved a continuous data exchange over the network between a personal computer and Sun workstations. The workstation software applications were run under the SunOS® 5.4 operating system. Data file transfer was effected using commercial file transfer protocol software produced by ftp Software®, Inc. Various application software packages used during processing are described in the following sections.

4.2.2 Vista® 6.6

The Vista® 6.6 (1992) seismic analysis program was used to convert the raw data from the field format (Bison-2) to SEG-y floating point for review and editing purposes. The Vista® 6.6 program is designed to read any seismic field data format. The raw data were then converted to IBM floating point, for input into the Landmark® Insight IT&A (1994) v. 5.1 application software on the Sun workstations. The Vista® 6.6 program was later used to perform interactive first break picking on the shot gathers prior to refraction statics analysis, which was done using Hampson-Russell® (1994) GLI3D.

4.2.3 Landmark® Insight IT&A 5.1

The Insight IT&A seismic analysis application software comprises a package of several programs designed to perform specific tasks involved in routine processing. The package is applicable to both 2D and 3D land and marine seismic data. The software was run on three Sun Microsystems computers connected to a SPARCserver 1000. The computers are networked to a local Laserjet hard copy device and also to a Versatec 36" black and white raster plotter (Kocurko, 1994). The main seismic processing aspects were carried out with this application software. The entire task was approached in an iterative manner wherein the result from every processing step was inspected and either accepted or the processing parameters adjusted until an acceptable solution was achieved.

4.2.4 Hampson-Russell®

The Hampson-Russell® seismic analysis software comprise three interactive programs: GLI3D, AVO, and Strata. GLI3D was used for refraction statics analysis and the computation of a near surface velocity model based on the first break arrivals. First break energy picking may be performed within or without the program. In this case picking was done in Vista® 6.6. AVO is a prestack seismic modelling program used for the analysis of the variation of trace amplitude with offset. This modelling is normally

carried out when a down-the-hole sonic log is available. However, in this particular case, no sonic log was available, but a pseudo-log was created from RMS seismic velocities obtained through velocity analysis. The data inversion achieved with this method was acceptable. The third program, Strata®, also strictly requires the presence of a sonic log, but a reasonable model may be obtained by a prudent choice of a pseudo-sonic log from available RMS seismic velocities.

4.2.5 Preprocessing

The shot gathers were inspected in Vista® 6.6 for dead and noisy traces. This exercise was intended to update the observer's log notes created during field acquisition. A tabular inventory of all the shot and receiver stations was prepared with appropriate flags for live and dead traces. The data were then converted from the Bison-2 format to IBM floating point for input to Insight IT&A 5.1. The error in the GPS (x,y) coordinates is ± 30 m, hence the accuracy of the end points of the line is only that good. However, the receiver and shot locations were accurately positioned along the line to ± 0.5 m by the transit survey[6]. The seismic data, observer and survey notes files were then transferred to Insight IT&A 5.1, wherein trace headers were assigned to the data. The processing flow chart for the data is shown in figure 4.2.5-1.

---

[6]The (x,y,z) co-ordinates for the seismic line at Marophe obtained from the transit survey are listed in appendix A.

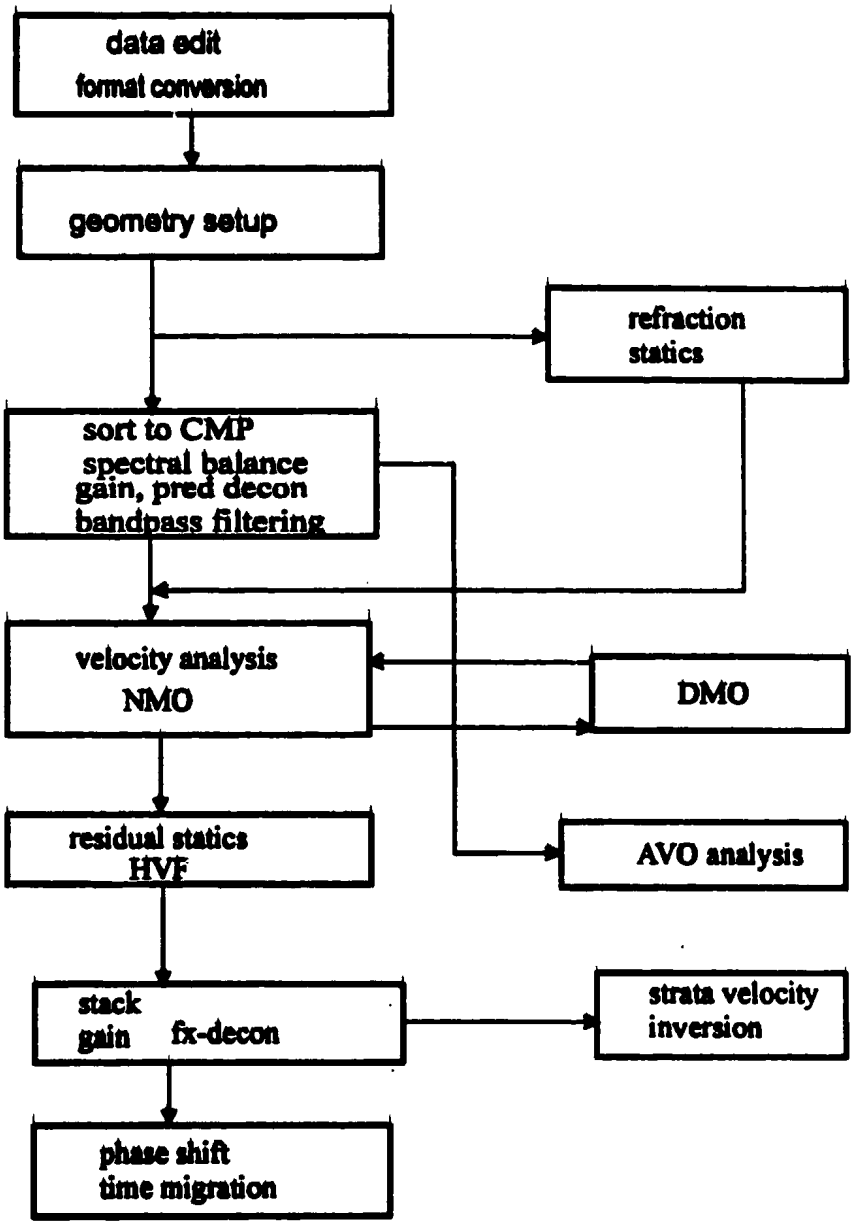

Figure 4.2.5-1: Flow diagram showing the processing steps used on the current data.

4.3 Prestack Processing

4.3.1 Geometry Definition

The field records comprised 48 channel split spread gathers. The line was shot at every station, producing a nominal stacking fold of 24. The station interval was 9.0 m, thus giving a CDP sampling of 4.5 m and a total spread length of 432 m.

The observer notes file created in the previous section was input into Insight IT&A 5.1 to generate a field acquisition geometry model (fig. 4.3.1-3). The fold diagram is staggered at the beginning because of a number of dead shots that were recorded in the first day. The diagram (fig. 4.3.1-3) shows that a maximum fold was maintained for most of the seismic line. The survey file was used to create the line geometry in ground coordinates and also the elevation profile (fig. 4.3.1-1). It is apparent from figure 4.3.1-2 that the survey line was essentially straight. The elevation profile indicates a 9.9 m elevation change over the entire line (4452 m). This yields an average terrain slope of 0.002. However, figure 4.3.1-1 shows that much of the elevation change occurs at a location between eastings 734797 and 735022 (225 m). There was a visible topographic ridge on the ground at this place, marking the surface location of the Kunyere fault. Both the observer and survey models were incorporated into the seismic data trace headers, after inspection.

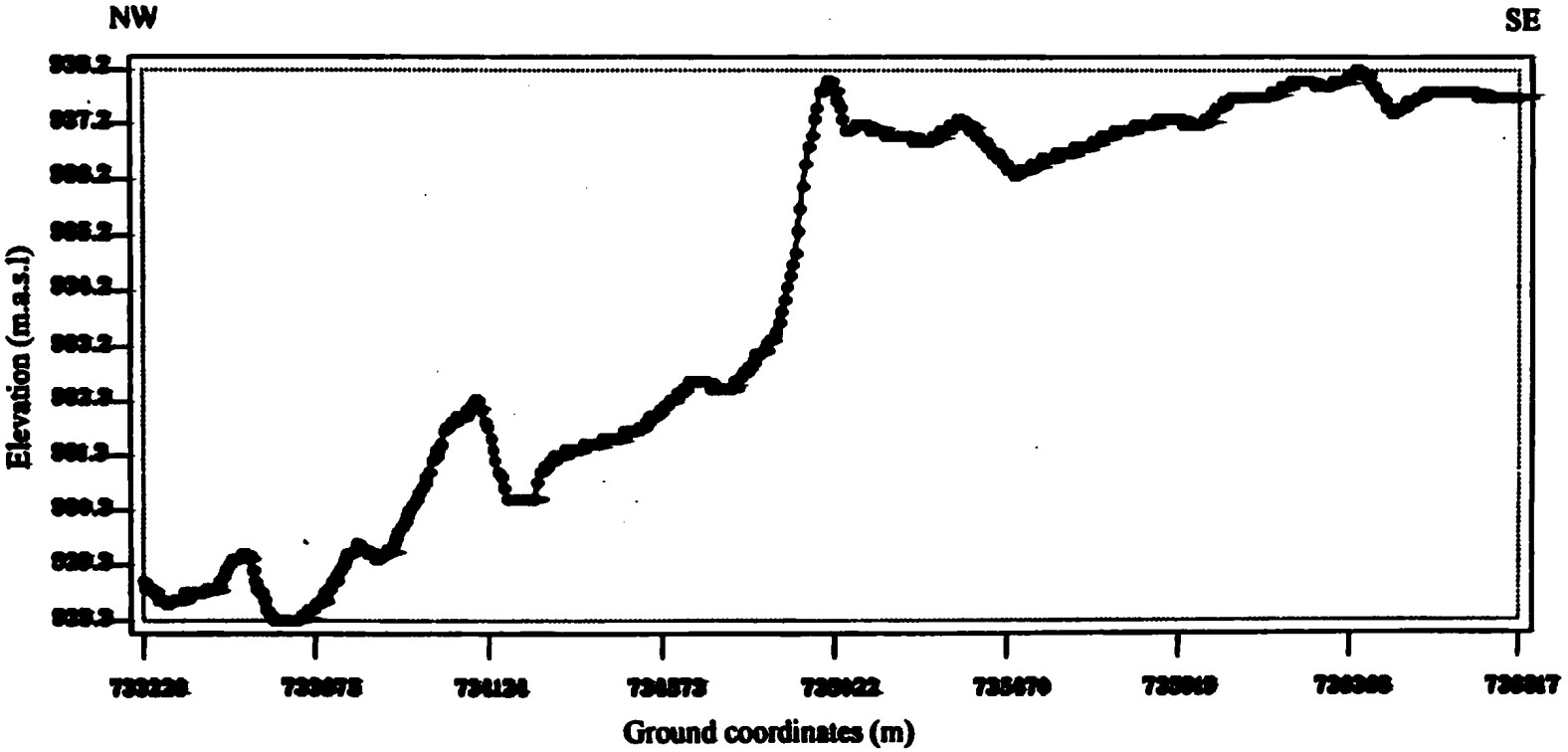

Figure 4.3.1-1: Elevation profile along the seismic line. The ground coordinates are UTM, zone 34, referenced to the Clarke 1880 spheroid.

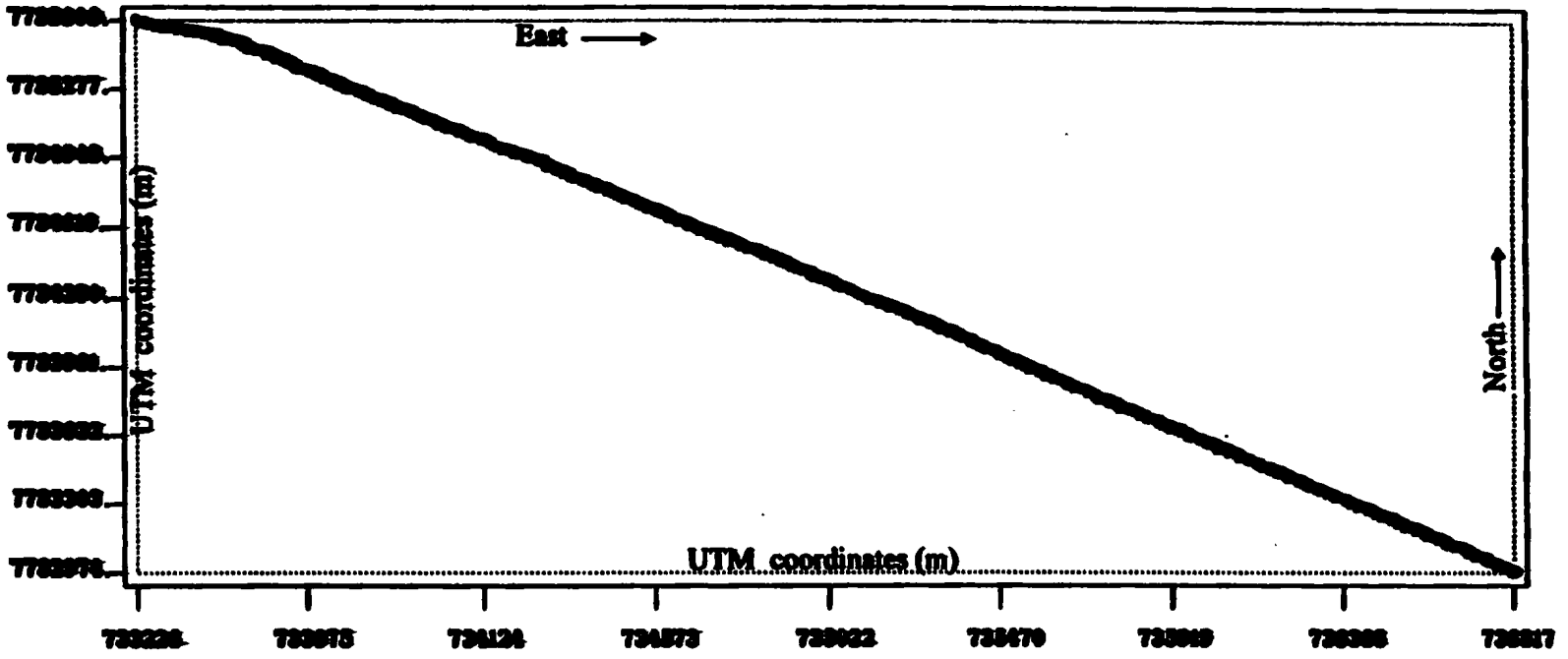

Figure 4.3.1-2: The ground plan of the seismic line. The map projection is UTM, zone 34, Central meridian of 21° E.

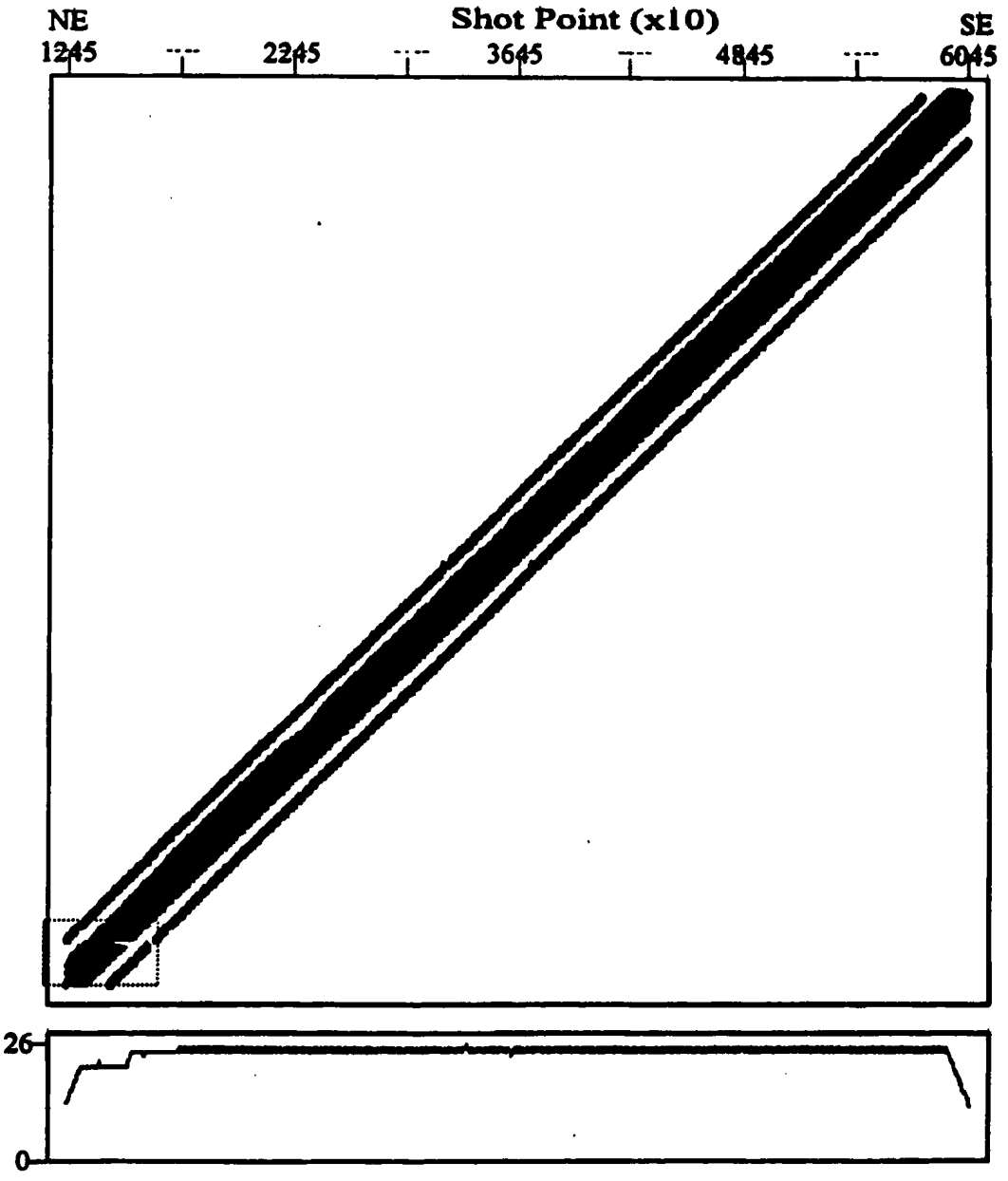

Figure 4.3.1-3: The fold stacking chart. The chart shows that a nominal fold of 24 was maintained for most of the line.

4.3.2 Refraction Statics

A discussion of refraction statics follows from the simple source-receiver geometry in figure 4.3.2-1. The source and the receivers in the figure are at different elevations, and the weathered layer below the surface has a variable thickness.

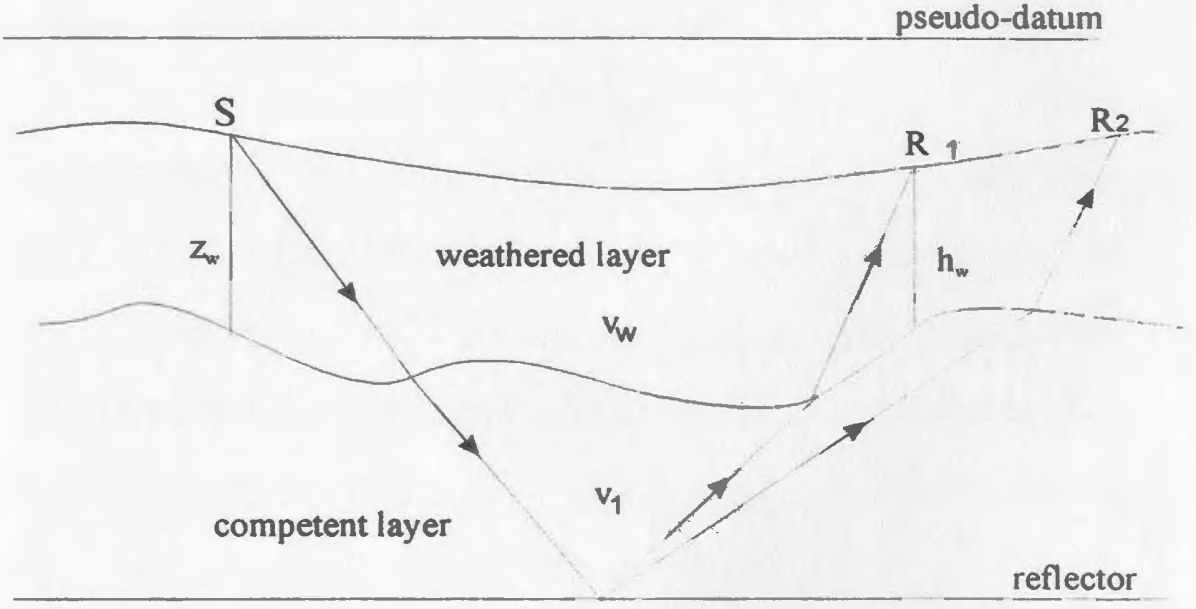

Figure 4.3.2-1: A schematic diagram to explain the various quantities considered in the calculation of static time corrections.

The delay on the reflection travel time due to the weathered layer at R_1 is;

$$t_w = \frac{z_w + h_w}{v_w} \qquad (4)$$

where t_w, z_w, h_w, and v_w are the transit time, thickness, and seismic velocity of the weathered layer, assuming normal incidence of the seismic ray. The receiver R_1 will record a different delay time because of the differences in weathering thickness and elevation, but also because the receiver is further away from the source. The effect of the latter is treated under the section on velocity analysis. If the time delay due to elevation and weathering thickness variation is removed from the seismogram, the reflections from the first reflector would line-up smoothly. Any deviation from a smooth line-up would be due to structure on the reflector surface. This is of course the goal of the reflection survey.

In practice, static time shifts are removed by replacing the seismic velocity of the weathered layer with an average replacement velocity representative of the material just below the weathered zone. The receiver and source elevations are transformed to a common datum to remove the effect of elevation variation. The static elevation correction in this case at R_1, for example, would be;

$$t_e = \frac{z_e + h_e}{v_w} \qquad (5)$$

where z_e and h_e are elevation differences of the source and the receiver above or below the datum. The total static shift to be removed is therefore $t_w + t_e$.

The seismic velocity of the weathered layer may be obtained by measuring uphole times or by carrying out a special refraction experiment in regional surveys. In high resolution seismic work, however, the source-receiver spacing is sufficiently small to allow a simultaneous recording of the direct and near-surface refraction energy. This allows for the determination of the near-surface velocity model directly from the reflection seismogram, prior to further processing. These events are then muted out before stacking to avoid contamination of the stacked section with spurious events[7].

The required static time shifts are obtained by tracing out and recording the first arrival energy on a reflection seismogram. This energy will comprise direct rays at near offsets and refracted rays at far offsets. The main problem with first break picking is that data should not be filtered prior to first break picking, as this may shift peaks and troughs on the seismic trace. First break picking is therefore performed on raw shot gathers, with only amplitude gain applied. This is critical since by nature static time shifts are very small.

---

[7] Refracted arrivals may sometimes be incorporated into the stack to image very shallow structure. This procedure requires that the refractions be corrected for linear refraction moveout (RMO). This technique is outlined in Çoruh et al., 1995.

4.3.4 Hyperbolic velocity filtering

Conventional frequency filtering of seismic data requires that signal and noise on a seismogram be dominant at different frequency bands. In the event that this is not the case, it is necessary to use alternative methods such as hyperbolic velocity filtering (HVF) (Mitchell and Kelamis, 1990). In this section we examine the physical basis of HVF and its applicability to the present data set.

We define the appropriate concepts and terminology using figure 4.3.4-1. Assume a plane wavefront approaching a horizontal surface at an angle ϕ from below. By Pythagoras' theorem we see that (Treitel et al., 1982)

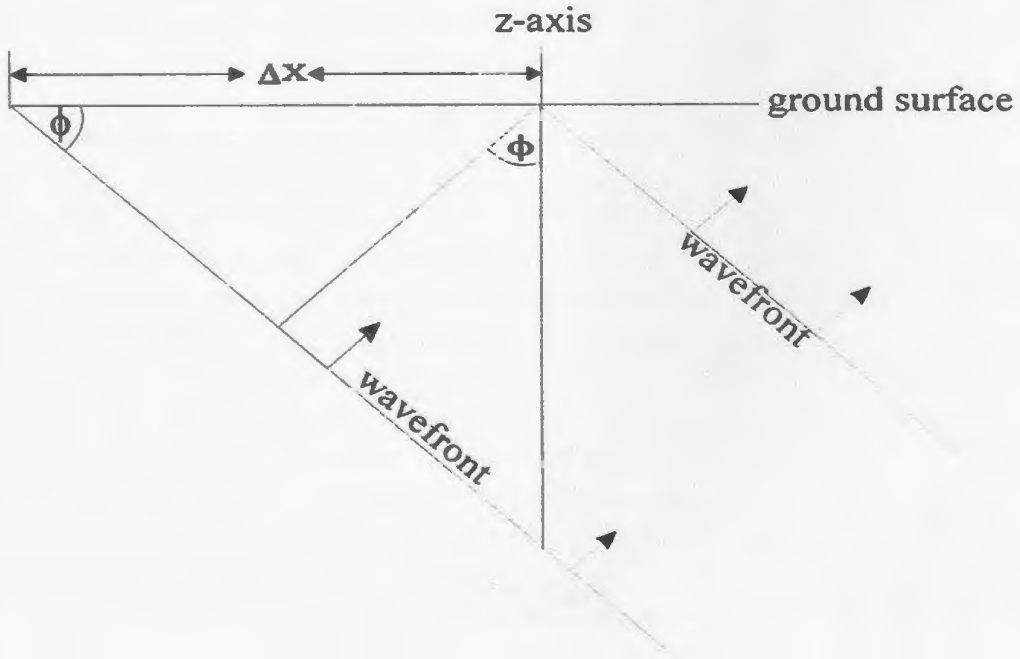

Figure 4.3.4-1: Definition of terms and concepts used in hyperbolic velocity filtering

deepest layer on the velocity-depth model. This method was used initially to derive a preliminary velocity-depth model and also to calculate a replacement velocity.

The second method of static calculation takes into account the velocity of the deepest layer and includes the calculation of a flat pseudo-datum. The statics are calculated from the relation (Hampson-Russell®, program documentation, 1994);

$$T_s = \frac{(D_P - D_{PS})}{V_{REP}} - \sum_{J=1}^{NL} \frac{(D_{J-1} - D_J)}{V_J} - \frac{(D_{NL} - D_{PS})}{V_{NL+1}} \qquad (6)$$

for a surface shot and

$$T_R = \frac{(D_P - D_{PS})}{V_{REP}} - \frac{(Z_R - D_1)}{V_1} - \sum_{J=2}^{NL} \frac{(D_{J-1} - D_J)}{D_{J-1}} - \frac{(D_{NL} - D_{PS})}{V_{NL}} \qquad (7)$$

for a receiver, where T_S, T_R, are the shot and receiver statics, D_P, D_{PS}, the processing datum and pseudo-datum, Z_R, the receiver elevation, V_{REP}, the replacement velocity, D_J, the elevation at the base of the J^{th} layer, V_J, the velocity of the J^{th} layer, and D_{NL}, V_{NL}, the elevation and velocity of the deepest layer.

The first term in both equations (6) and (7) is constant if the processing datum and pseudo-datum are flat. Hence a change in the replacement velocity will effect a bulk time shift to the entire line. The last term takes account of the deepest layer in the calculation.

The statics derived from the above equations are called long wavelength since a smoothing function is applied to stabilize the algorithm. The statics however contain elevation statics which comprise both long-wave and short- wave components. Residual short-wave statics are also computed from the data (not the model) during the inversion and are included in the output statics model. These are derived through the Gauss-Seidel algorithm (Hampson-Russell®, program documentation, 1994). Residual static calculation is discussed in a later chapter.

If we add equations (6) and (7), we get;

$$T_{S+R}=\frac{2D_P}{V_{REP}}-L_S-L_R \tag{8}$$

where L_S and L_R are the long-wave shot and receiver static components. If we let.

$$D_P=\frac{V_{REP}(L_S+L_R)}{2} \tag{9}$$

then the calculated static time shift would be zero. In practice, the processing datum is chosen such that the derived static time shifts are as small as possible. This is important in high resolution work because a large static time shift may displace reflections on the stacked section, giving an erroneous interpretation. A large upward static time shift makes reflection events more prone to distortion by NMO stretching, since the latter is more severe at early times. The datum is chosen as close to the ground surface as possible so that reflection events are retained at their correct arrival times. The statics

inversion calculated a pseudo-datum of 865 m.a.s.l., and a replacement velocity of 1323 m/s at a processing datum of 940 m.a.s.l.

The velocity-depth model derived through first break inversion is included in figure 4.3.2-2. The model consists of two low velocity layers overlying a half space. The surface layer has a constant thickness of ~ 15 m with a perturbation at station 4155. The velocity for this layer is ~600 m/s for the entire line. The ground surface was observed to consist of loose sand in the southeast, and unsaturated clays in the northwest. Moreover, the groundwater level was observed at 14.5 m in a hand-dug well close to the seismic line. The second horizon has a velocity varying from 1800-1600 m/s from the northwest to the southeast. The base of this layer is very irregular. The layer is ~40 m thick. The seismic velocity at the top of the half space decreases from 2800 to 2200 m/s from the beginning to the end of the line. The derived statics also show a marked anomaly at station 4155 corresponding to the velocity anomaly.

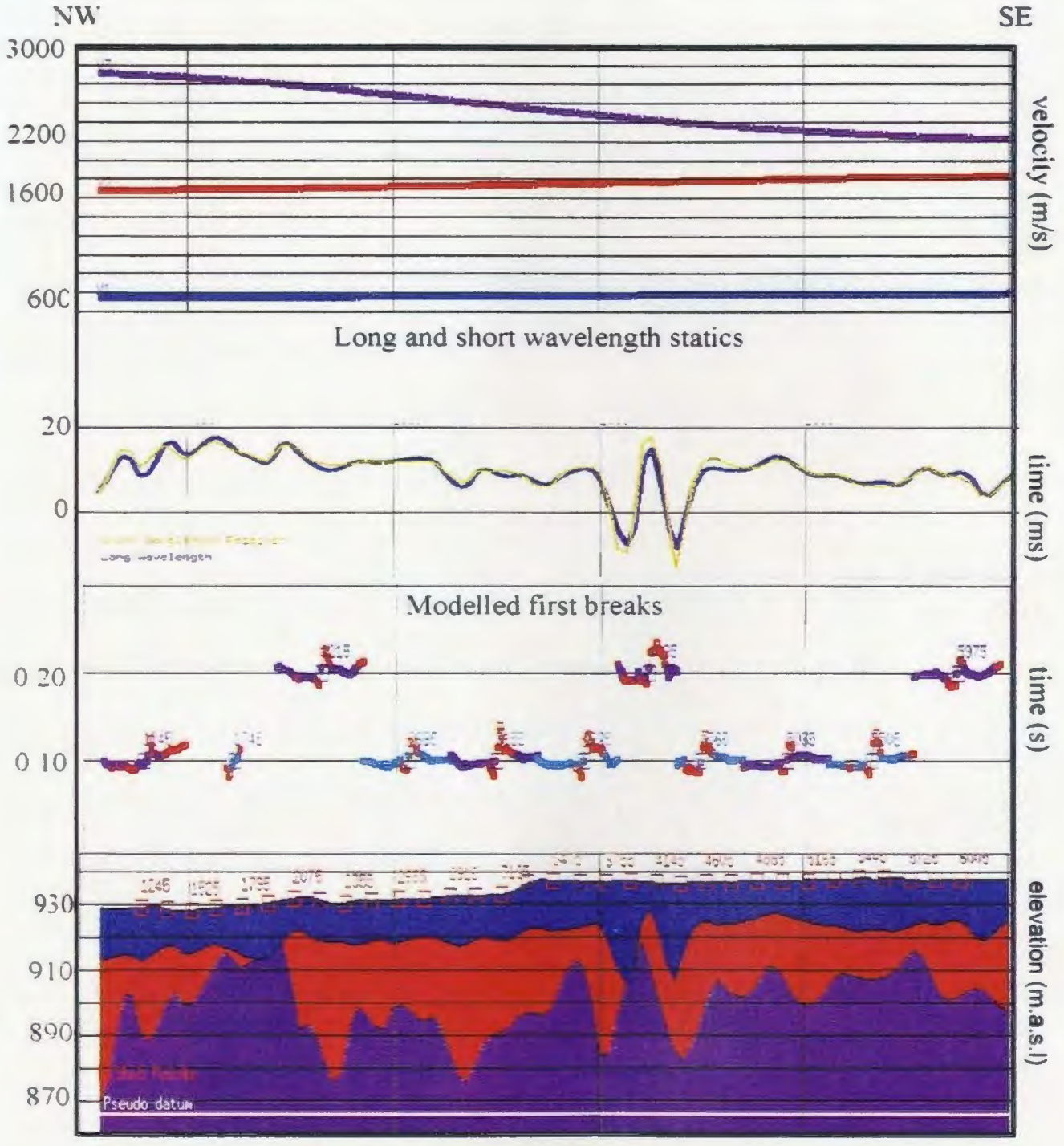

Figure 4.3.2-2: Near-surface velocity-depth model derived through refraction statics analyis with the GLI3D program. The top panels show the modelled first breaks, the calculated statics, and the lateral velocity function for the near-surface.

4.3.3 Gain and filtering

The shot gathers were amplified using a 200 ms AGC (automatic gain control) time gate and inspected to assess the signal to noise level and also to determine optimum frequency filtering parameters. Amplitude spectra for selected shot records show high energy events confined to a 20-150 Hz frequency bandwidth (fig. 4.3.3-1). The remaining frequencies comprise low amplitude ambient noise.

Furthermore, 20 Hz wide frequency filter panels were calculated and displayed side by side (fig. 4.3.3-2). Both coherent noise and signal dominate the spectral band 40-100 Hz, beyond which the events are equally weakened. These events are indicated with arrows in figure 4.3.3-2.

Spectral balancing involves the application of bandpass filters to input data over a specified frequency band, and computing a weighted average within each band. The weighted averages from each band then constitute the output spectrally balanced spectrum. The lower and upper cutoff frequencies are varied until an acceptable result is achieved. Spectral balancing was applied to the data over a 20-120 Hz frequency window, at 20 Hz filter bands, and 200 ms AGC. The derived amplitude spectrum for CDP 3665 is shown in figure 4.3.3-3.

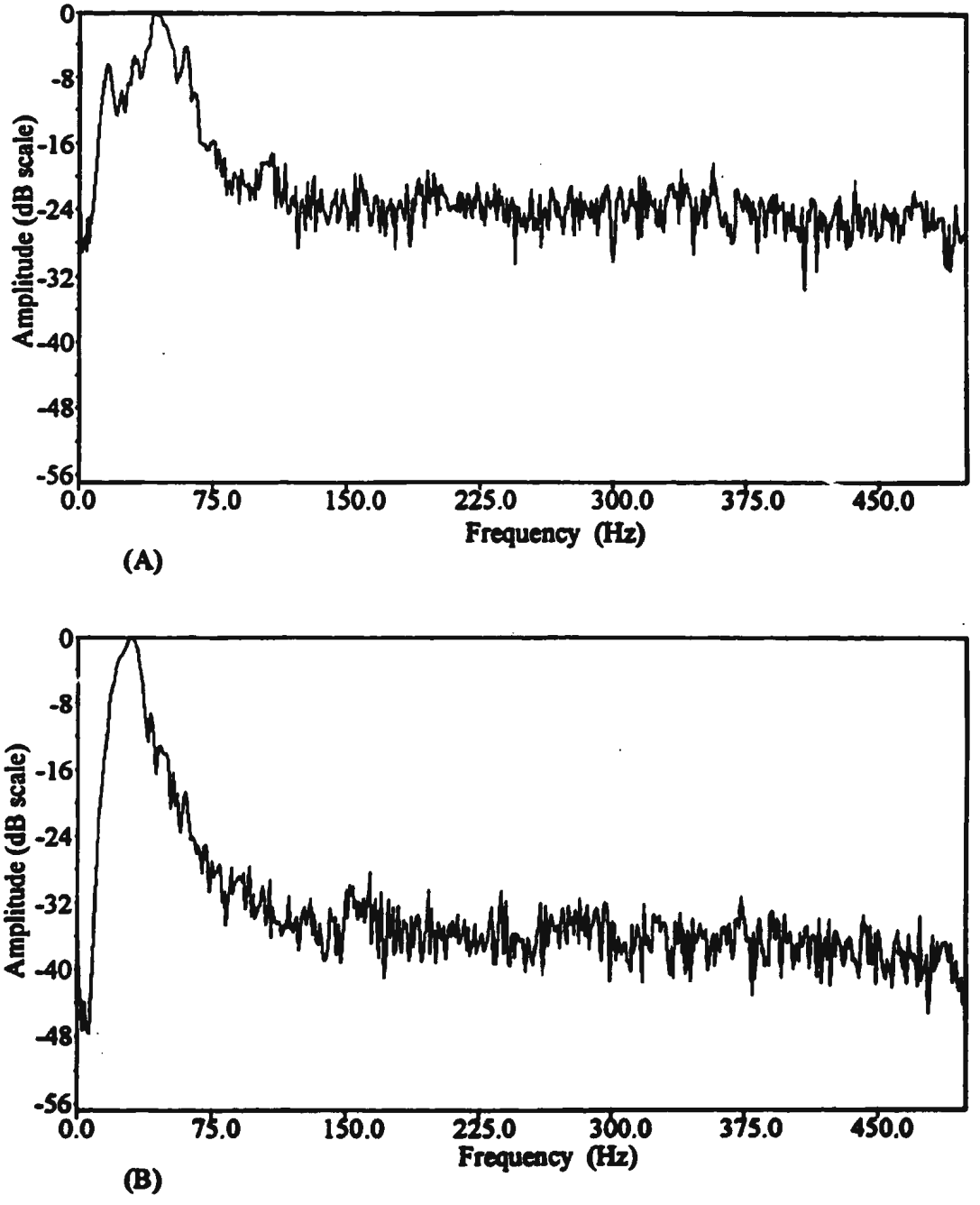

Figure 4.3.3-1: Amplitude spectra from CDP 2350 (A) and (B) 4735. Note that the spectrum is low amplitude and white beyond 150 Hz.

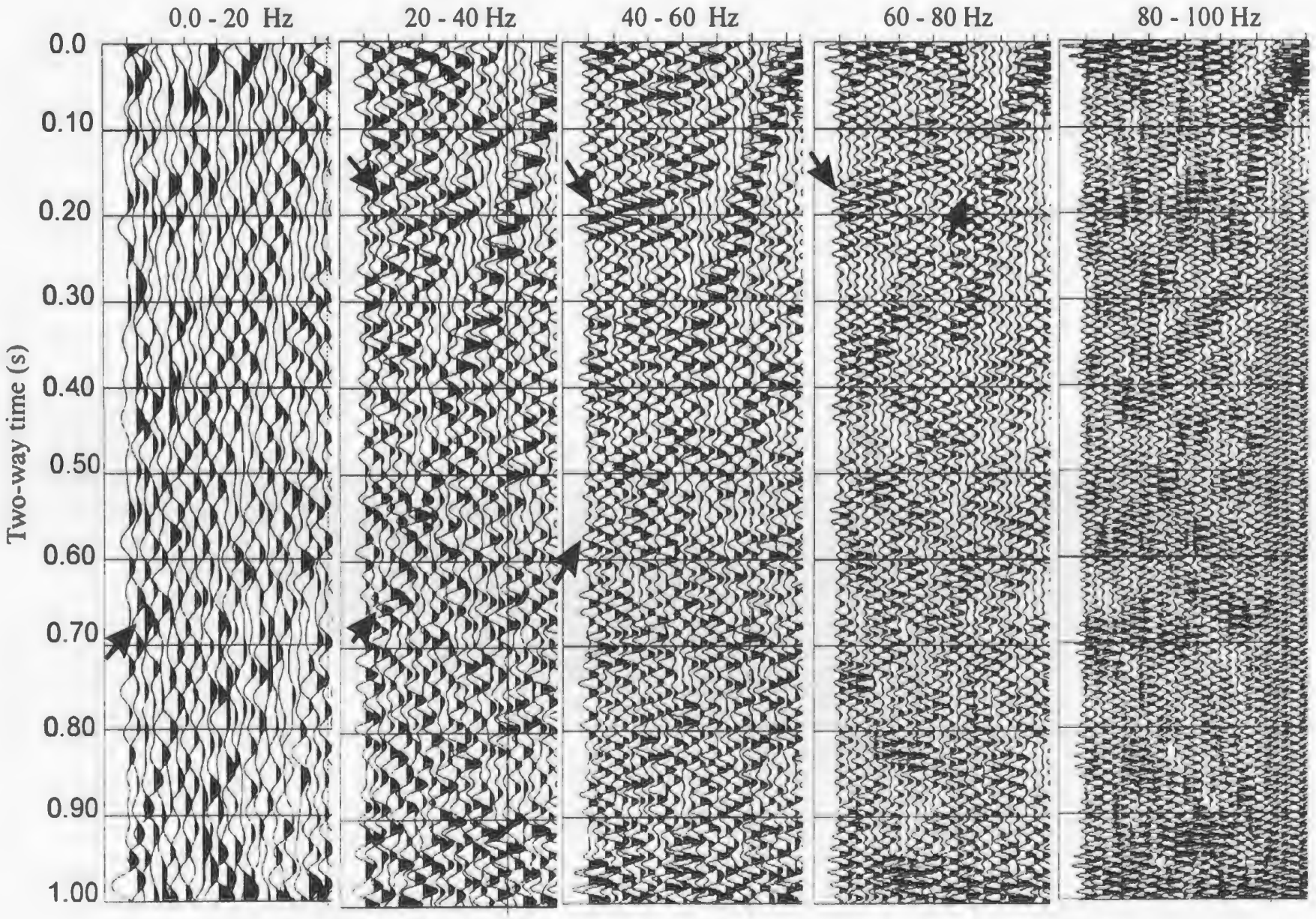

Figure 4.3.3-2: Frequency filter panels displayed to determine optimum bandpass filter parameters. Shot 4285. It is apparent from the display that the ground-coupled airwave dipping to the left is present at all frequencies

Inspection of the shot gathers showed that the signal comprises visible reflections, direct wave, and refraction(s), and that the noise is dominated by a ground-coupled air wave (v = 340 m/s). The frequency bandwidth of the air wave (fig. 4.3.3-2) is very broad, hence it cannot be separated from the signal by conventional bandpass filtering. Examination of the frequency spectrum in the f-k domain indicates that the noise train is aliased over the higher frequencies. It appears that the sampling interval was not small enough to prevent aliasing in the recording. The most effective method to remove the air wave without compromising the phase component of the signal was found to be hyperbolic velocity filtering (HVF). This is because tau-p processing allows a re-sampling of the data during inverse tau-p transformation.

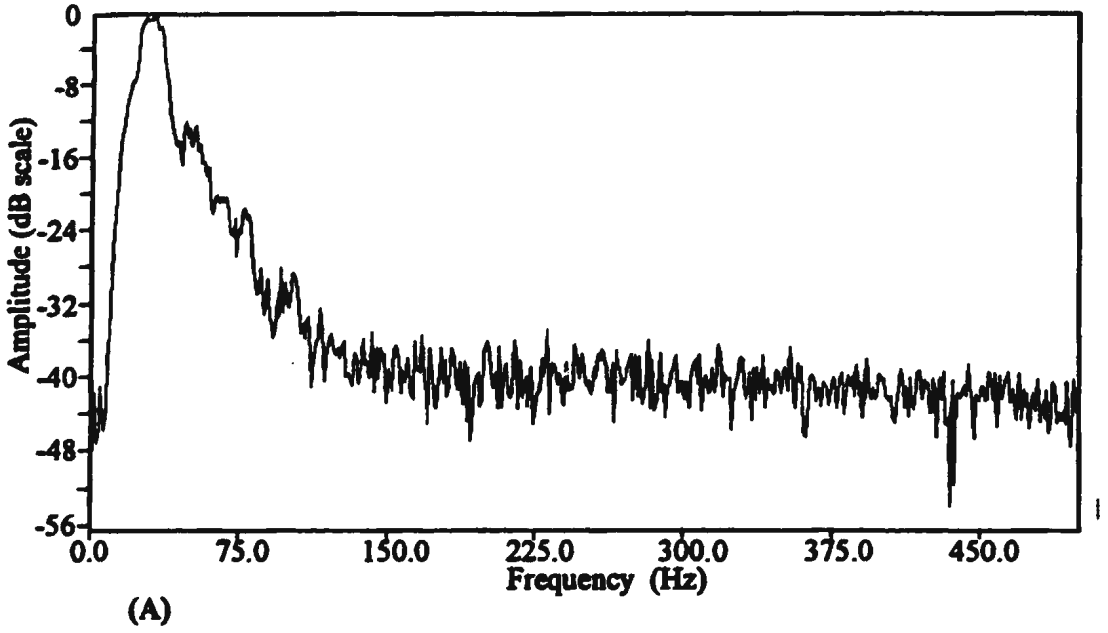

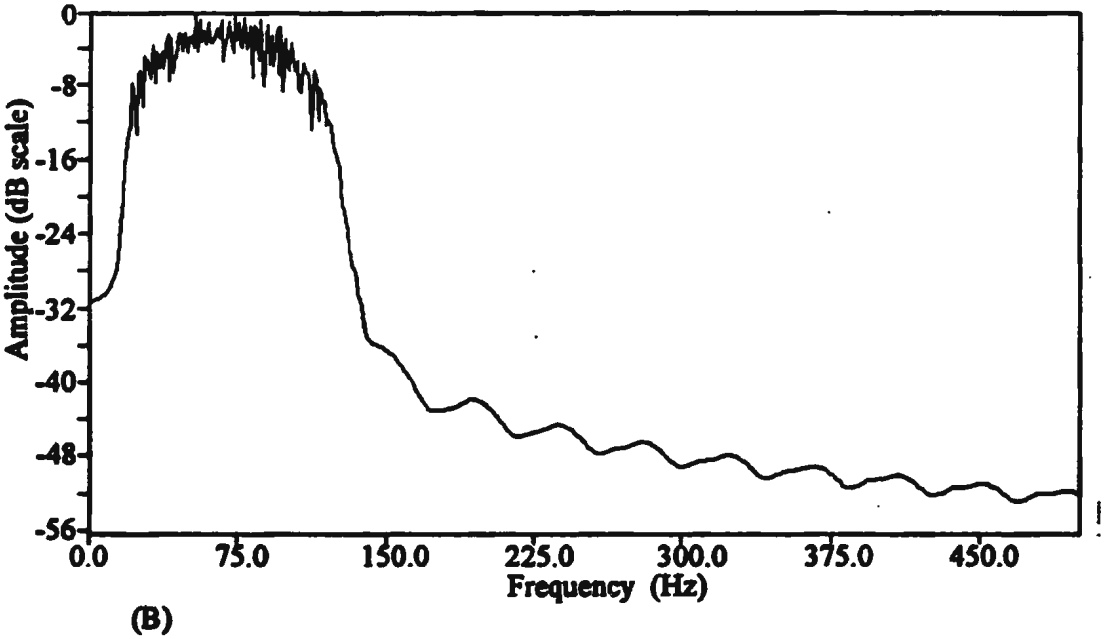

Figure 4.3.3-3: Amplitude spectra for CDP 3665 before (A) and (B) after spectral balancing and HVF. Note that the spectrum is white beyond 150 Hz.

4.3.4 Hyperbolic velocity filtering

Conventional frequency filtering of seismic data requires that signal and noise on a seismogram be dominant at different frequency bands. In the event that this is not the case, it is necessary to use alternative methods such as hyperbolic velocity filtering (HVF) (Mitchell and Kelamis, 1990). In this section we examine the physical basis of HVF and its applicability to the present data set.

We define the appropriate concepts and terminology using figure 4.3.4-1. Assume a plane wavefront approaching a horizontal surface at an angle ϕ from below. By Pythagoras' theorem we see that (Treitel et al., 1982)

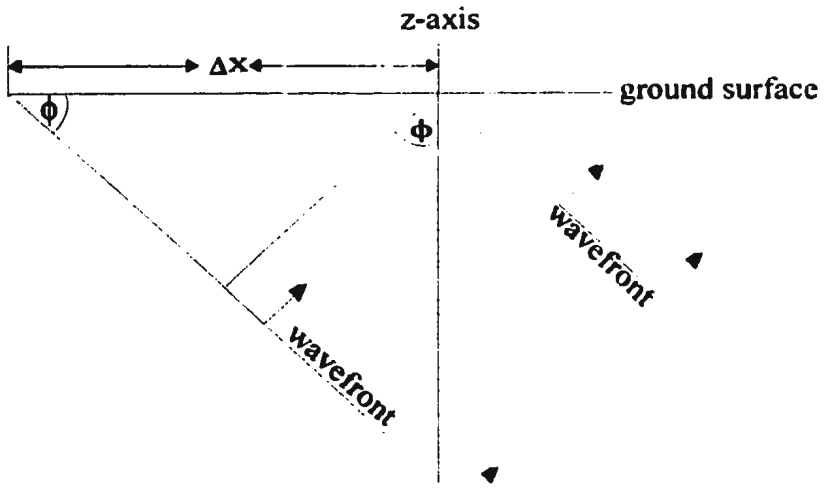

Figure 4.3.4-1: Definition of terms and concepts used in hyperbolic velocity filtering

$$\sin\phi = \frac{v\Delta t}{\Delta x} \tag{10}$$

where Δx is the horizontal distance travelled by the wave in the time increment Δt, and v is the wave velocity. The quantity $\Delta t/\Delta x$ is the Snell, or ray parameter, p. It may be seen from figure 4.3.4-1 that the inverse of p, i.e. $\Delta x/\Delta t$ represents the horizontal phase velocity of the propagating wavefront. The ray parameter, p, is therefore the horizontal slowness of the wavefront. It is often referred to as "stepout per trace" (Treitel et al., 1982)

Consider the expression for hyperbolic moveout in T-X space (Yilmaz, 1987);

$$t^2 = t_0^2 + \frac{x^2}{v^2} \tag{11}$$

where t is the reflection time, t_0 is the zero-offset time, x is the horizontal offset, and v is the wave velocity. Differentiation of (11) gives;

$$\frac{dt}{dx} = \frac{x}{tv^2} \tag{12}$$

and we note from (10) that (Noponen and Keeney, 1986)

$$\frac{dt}{dx} = \frac{\Delta t}{\Delta x} = p \tag{13}$$

so that

$$p=\frac{x}{tv^2} \tag{14}$$

Stoffa et al. (1981) define τ as the contribution to the travel time of the vertical component of the wavefront propagation, as defined in figure 4.3.4-1 and express it as

$$\tau=t-px \tag{15}$$

Substituting for t in (14), we have

$$p^2v^2x+pv^2\tau-x=0 \tag{16}$$

The positive root of (16) is

$$p=-\frac{\tau}{2x}+\sqrt{\left(\left(\frac{\tau}{2x}\right)^2+\frac{1}{v^2}\right)} \tag{17}$$

Using (17), we can define the inequality (Mitchell and Kelamis, 1990);

$$\mu+\sqrt{\left(\mu^2+\frac{1}{v^2_{max}}\right)}\le p\le\mu+\sqrt{\left(\mu+\frac{1}{v^2_{min}}\right)} \tag{18}$$

where $\mu = -\tau/2x$. If we limit the value of p according to the inequality in (18) during the forward τ-p transform, we are effectively executing a mute operation in τ-p space (Mitchell and Kelamis, 1990). The extent of the mute is controlled by the stacking velocities v_{max} and v_{min}. Mitchell and Kelamis (1990) have shown that a hyperbolic event in T-X space maps to an elliptical line segment in the τ-p domain. The action of the mute

in (18) is to select portions of the line segments at points of tangency to the ellipses. The length of the segment to select is specified by the velocities v_{max} and v_{min}. The design and implementation of (18) constitutes the process of hyperbolic velocity filtering (HVF).

While HVF achieves some success in noise removal, it may also introduce artifacts into the data. For this reason it may be advisable to proceed to stack data in the τ-p domain if it contains noise that cannot otherwise be removed by T-X processing. This avenue has been investigated by Mitchell and Kelamis (1990), Stoffa et al. (1981), and Treitel et al. (1982), and has produced promising results.

The present data set was filtered using the HVF and then inverse transformed to T-X space because the current processing package (Insight IT&A 5.1) does not support further processing in τ-p space[8]. Sample HVF filtered and frequency filtered records are shown for comparison in figure 4.3.4-2.

[8] tau-p processing requires an algorithm to correct for elliptical moveout, which is a tau-p analogue for NMO.

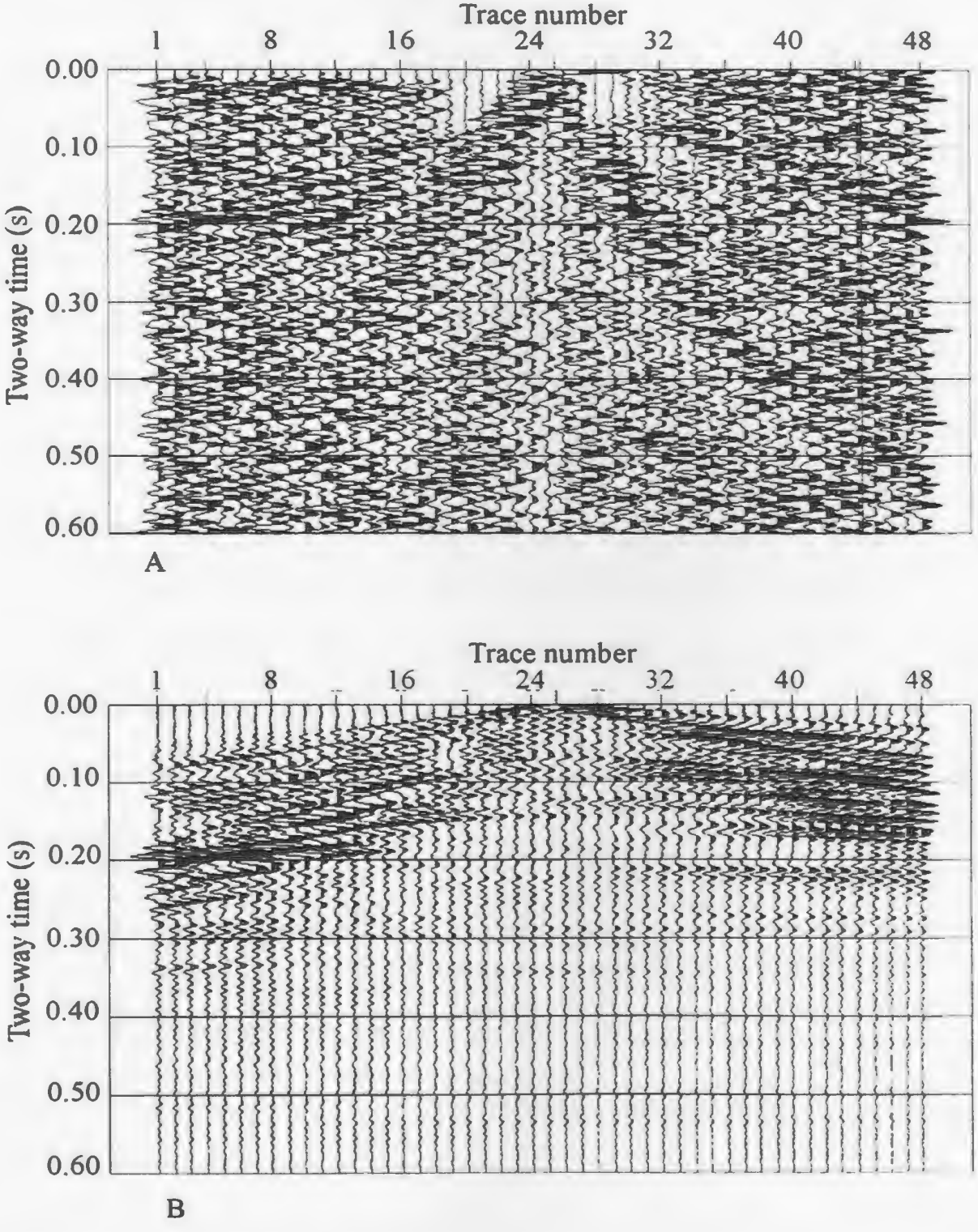

Figure 4.3.4-2: Frequency (A) and (B) hyperbolic velocity filtering on CDP 3650. (A) was filtered using a 20-40/120-140 Hz trapezoidal bandpass filter. HVF has effectively removed the low velocity noise train visible in (A).

4.3.5 Deconvolution

The autocorrelation function (ACF) of a seismic trace contains a contribution from reflected signal at small time lags, where it is periodic (Robinson, 1984). At long time lags the contribution from random noise and/or multiple reflections dominates the autocorrelation function. This property of the ACF provides a way to design and implement a predictive deconvolution filter whose aim is to shorten the function to the periodic window, and remove any coherent events outside this window (multiples). The effect of deconvolution on the seismic trace is to improve temporal resolution by broadening the frequency spectrum (shortened wavelet), and removal of multiple reflections. In the event that the seismic wavelet is shortened to the length of the sampling interval, one speaks of spiking deconvolution (Yilmaz, 1987).

Inspection of the autocorrelation function at several shot gathers showed the presence of some weak long period multiples at a 150-200 ms lag (fig. 4.3.5-1). These may be reverberations from the base of the Kalahari beds. A predictive deconvolution operator was designed to remove these multiples and also to shorten the wavelet to 15.0 ms (2nd 0-crossing). This operation was tested on a number of shot gathers and was found to produce good results. Graphs of the autocorrelation function before and after deconvolution on shot 1840 are shown in figure 4.3.5-1.

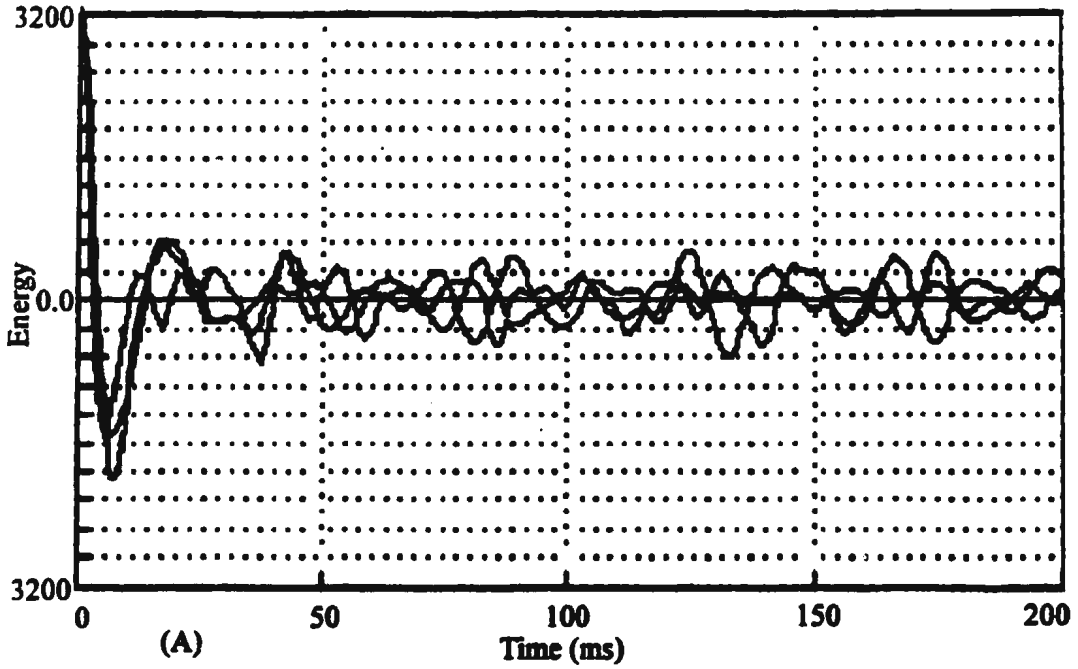

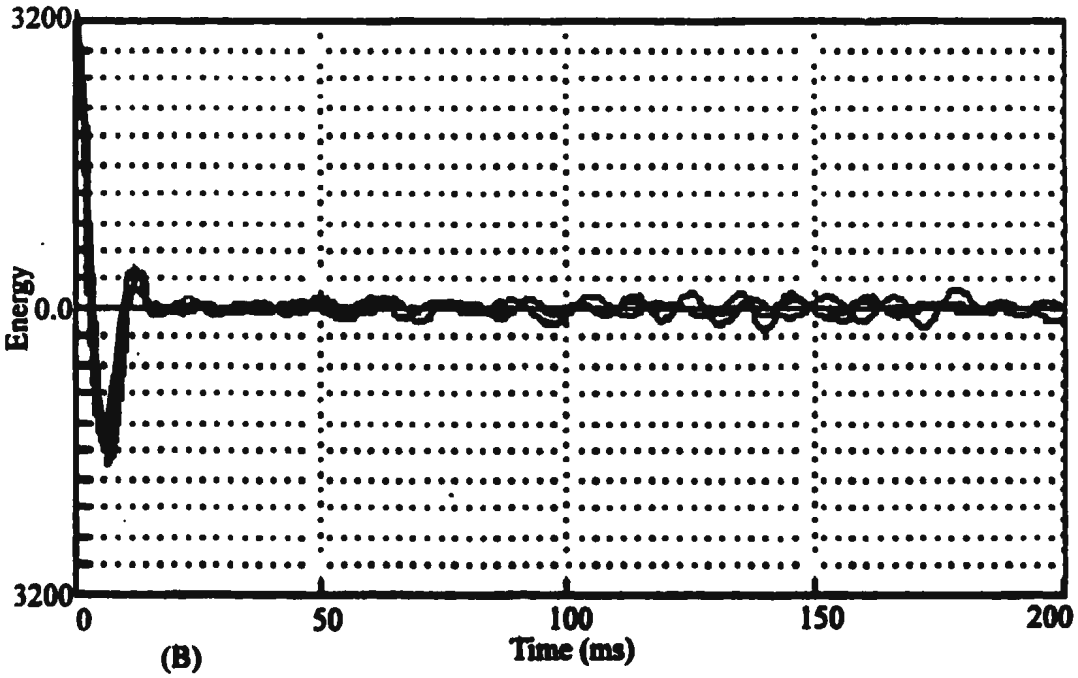

Figure 4.3.4-1: The autocorrelation function for traces 44-46 of shot 1840 before (A) and after (B) predictive deconvolution.

4.3.6 Velocity Analysis

The aim of acquiring multichannel reflection seismograms is that the individual traces within the record can be stacked at zero-offset time to produce a trace with improved S/N ratio. This ideal cannot be realized without further processing because reflection events arrive at increasingly later times with increasing offset. We restate equation (11) to define normal moveout (NMO) (Yilmaz, 1987);

$$t^2 = t_0^2 + \frac{x^2}{v^2} \tag{19}$$

We may see from (19) that NMO constitutes the difference between the two-way travel time at zero-offset and a given non-zero offset x. The presence of NMO on a seismogram will cause destructive interference on the reflection event during stacking. The situation can be remedied by calculating the velocity to a given reflector from the seismogram, and then using that velocity to calculate NMO. A correction is then applied to the seismogram which results in reflections lining up in a horizontal line. This linear form then ensures that the reflection amplitudes will add constructively to produce a stacked trace with improved S/N ratio. Velocity analysis is a computational procedure used to obtain and correct for NMO on a seismogram. Three complementary velocity analysis methods were used in the present work; the T^2-X^2 method, constant velocity stacking (CVS), and semblance analysis.

4.3.6.1 T^2-X^2 method

The reflection travel time equation (19) describes an hyperbola in T-X space. However, in T^2-X^2 space, the same equation describes a straight line with slope $1/v^2$, and intercept t_0^2. This attribute in T^2-X^2 space provides a reliable method to compute stacking velocities from a reflection seismogram (Yilmaz, 1987). This method can also be used to compute the apparent dip of reflecting horizons from split spread gathers. In this setup one half of the spread records in the updip direction while the other records in the downdip direction. An estimate of the apparent reflector dip α is obtained from a T^2-X^2 plot using the relation (Robinson and Çoruh, 1988);

$$\alpha = \cos^{-1}\left(\frac{t_{min}}{t_0}\right) \tag{20}$$

where t_{min} is the intersection of the positive and negative arms of the graph, t_0 is the zero-offset time. Some of the shot gathers examined using this method indicated apparent dips of up to 20°. The accuracy of the method relies on the S/N ratio, which affects the quality of picking reflection events. Although the present data set had a low S/N ratio, the presence of some particularly strong reflection events made it possible to pick reflectors with confidence. Stacking velocities were determined on selected shot gathers along the seismic line. The results are shown in Table 4-2.

Table 4-2: Stacking velocities calculated using the T^2-X^2 method. It will be noticed that only one reflector was picked because of the poor S/N ratio.

Shot	Two-way zero-offset time (s)	Velocity (m/s)	Depth (m)	Dip (°)
2275	0.173	1821	158	21
2955	0.130	1626	107	19
3825	0.155	1685	131	8
3975	0.158	1829	144	0
4785	0.191	1874	179	0
4935	0.167	1800	150	0
5745	0.170	1570	133	0
5795	0.114	1628	93	0
5845	0.176	1730	152	0
5895	0.155	1732	134	18

4.3.6.2 Constant Velocity Stacks (CVS)

When NMO correction is applied to a reflection event on a seismogram, the event is flattened to a horizontal line. If, however, the correction was applied with an incorrect velocity, the event will bend away from the horizontal, depending on whether a higher or lower velocity was used. By repeatedly changing the estimated velocity, one may eventually arrive at the correct NMO velocity. This is efficiently implemented through an automated algorithm where different NMO velocities are applied to the same CDP gather. The gather is then stacked at each velocity. These constant velocity stacks are then displayed side by side in panels. The correct NMO velocity is picked by visual inspection as the one that produces the best horizontal coherent event across the stack.

Caution is required when picking velocities from a CVS panel (Yilmaz, 1987). First, one should have an idea of the expected velocity range for the particular data set. Yilmaz (1987) notes that dipping events may show unrealistically high velocities. The success of the CVS method depends on the S/N ratio. Since the present data set has a low S/N ratio, the method had only a limited success.

4.3.6.3 Semblance Velocity Analysis

The application of signal coherency measures to CMP data is discussed in Neidell and Taner (1971) and Yilmaz (1987). A signal coherency measure refers to a quantitative expression of the likeness of seismic signal in different CMP channels (Neidell and Taner, 1971). Common signal coherency measures include crosscorrelation, stacked amplitude, and semblance. The latter is particularly useful because in addition to quantifying coherence, it can also be used to estimate stacking velocities from CMP-ordered seismic data. Semblance is defined as the output to input energy ratio. The normalized version of semblance is described by (Yilmaz, 1987);

$$E_n = \frac{1}{M} \frac{\sum_t s_t^2}{\sum_t \sum_{i=1}^{M} f_{i,t(i)}^2} \qquad (21)$$

where M is the number of traces in the CMP gather, s_t is the stacked amplitude, $f_{i,t(i)}$ is the amplitude of the i^{th} trace at time t(i), and t(i) represents hyperbolic moveout of reflection trajectories (19).

By implementing (21) with the correct velocity, the signal is stacked constructively along a hyperbolic reflection trajectory. In this manner, reflection trajectories can be preferentially enhanced on a seismogram. In practice, the CMP gather is stacked at a

variety of velocities. The most coherent events (and hence correct stacking velocities) are then picked interactively on a graphical display.

Semblance analysis was performed on CMP's spaced at regular intervals along the seismic line at a sampling rate of 50 m/s. The analysis was bedeviled by the fact that the data was low S/N ratio and particularly difficult to pick. The picked velocities were cross-checked for authenticity and manually updated with information from the other velocity analysis methods described earlier. The final velocity file was used to interpolate a velocity function for stacking along the entire line (Table 4-3). Although the data had a low S/N ratio, this method turned out to be quite successful in picking RMS velocities.

4.3.6.3.1 Dip moveout correction (DMO)

A conventional seismic processing sequence includes NMO correction to CMP data followed by stack to produce an image of the subsurface. The expression for NMO correction (19) is strictly valid for horizontal reflections. In the presence of dipping reflectors the required NMO velocity is related to the true medium velocity by (Hale. 1984);

Table 4-3: RMS velocities determined from semblance velocity analysis. The time is zero-offset two-way in seconds and the velocity is in m/s.

CDP	T_1	T_2	T_3	T_4	V_1	V_2	V_3	V_4
1130	0.079	0.203	-	-	1499	2100	-	-
1530	0.081	0.158	0.279	0.641	1465	1626	2146	5900
1905	0.118	0.209	0.451	-	1264	1596	3216	-
2260	0.122	0.267	-	-	1327	2574	-	-
2620	0.059	0.167	0.274	-	1416	1579	2158	-
2880	0.106	0.291	-	-	1428	1812	-	-
3285	0.071	0.182	0.400	-	1302	1529	2184	-
3670	0.077	0.166	-	-	1302	1680	-	
4020	0.109	0.192	-	0.558	1906	2400	-	5848
4375	0.067	0.191	-	0.688	1441	1655	-	5900
4685	0.092	0.196	-	0.661	1462	1606	-	5900
5070	0.090	0.198	-	0.866	1328	1617	-	5786
5505	0.081	0.204	0.262	0.390	1350	1743	1800	2450

$$v_{NMO}=\frac{v_{true}}{\cos\theta} \tag{22}$$

where θ is the angle of dip of a given reflector. (22) indicates that for dipping reflectors a higher NMO velocity is required. However, since neither medium velocity nor dip is known prior to velocity analysis, it is difficult to estimate the correct NMO velocity from the shot gathers. A consequence of this aberration is that detail is lost from dipping reflectors during stack. A variety of algorithms has been developed to reduce the dependence of NMO velocity on reflector dip, so that both dipping and flat events can be stacked with the same NMO velocity (Hale, 1984; Notfors and Godfrey, 1987; Cabrera and Levy, 1989). For the general case, the hyperbolic moveout equation is (Hale, 1984);

$$t_0^2=t^2-\frac{4h^2}{v^2}+\frac{4h^2\sin^2\theta}{v^2} \tag{23}$$

where $(t^2 - 4h^2/v^2)$ is the NMO term and $(4h^2\sin^2\theta)/v^2$ is the DMO term, h is half the source-receiver offset. Hale (1984) developed a frequency-wavenumber algorithm to reduce NMO-corrected gathers to zero-offset sections, thus achieving the effect of migration before stack. For this reason DMO is also commonly referred to as prestack partial migration (PSPM). Removal of the DMO term from (23) leaves only the NMO term, free from the effects of reflector dip. This allows correct NMO velocities to be determined from the shot gathers in the usual manner (semblance, CVS, T^2-X^2). The main drawback with DMO algorithms is that they are computationally intensive. They

are thus taxing on the computing resources and may add significant cost to the processing sequence (Hale, 1984).

Notfors and Godfrey (1987) introduced a somewhat simpler DMO algorithm involving logarithmic transformations prior to Fourier transformation. Their premise was that the DMO operator in the logarithmic domain is both temporally and spatially stationary. The algorithm was extended and customized for application in the shot domain by Cabrera and Levy (1989). Starting with the Hale (1984) DMO equation for a shot gather:

$$P_0(t_0,x)=P_n\left(\sqrt{\left(t_0^2-\frac{x^2\sin^2\theta}{v^2}\right)},x\right) \tag{24}$$

where P_n and P_0 are NMO and DMO corrected gathers, and x is the source-receiver offset, Notfors and Godfrey (1987) define a logarithmic time transformation as:

$$\tau_0=T_c\ln\left(\frac{\tau_0}{T_c}\right) \tag{25}$$

where T_c is a reference time. Rearrangement of (24) and substitution of the log time transform yields (Notfors and Godfrey, 1987);

$$q_0(\tau_0,x)=q_n\left[\tau_0-\frac{x^2}{2T_c}\left(\frac{d\tau_0}{dx}\right)^2,x\right] \tag{26}$$

where q_0 and q_n are the data in the log time domain. Cabrera and Levy (1989) defined a logarithmic spatial transformation as;

$$\lambda = F_c \ln\left(\frac{x}{F_c}\right) \tag{27}$$

Substituting for x in (26) and taking the Fourier transform, the required DMO transformation becomes (Cabrera and Levy, 1989)

$$q_0(\omega,k) = q_n(\omega,k)\exp\left(-i\omega\frac{F_c^2}{2T_c}\frac{k^2}{\omega^2}\right) \tag{28}$$

where ω, k, are the temporal and spatial frequencies, and F_c is the dominant temporal frequency of the data.

The present data set contain significant reflector dip which made it hard to pick correct NMO velocities to the north of the Kunyere fault zone. Shot domain DMO correction (DMOS) was applied to the gathers to reduce them to zero-offset sections prior to detailed velocity analysis. The shot domain DMO correction was very successful in removing the dip dependence from the picked NMO velocities. An HVF-filtered shot gather is shown in figure 4.3.6.3-1 for comparison before and after DMO correction.

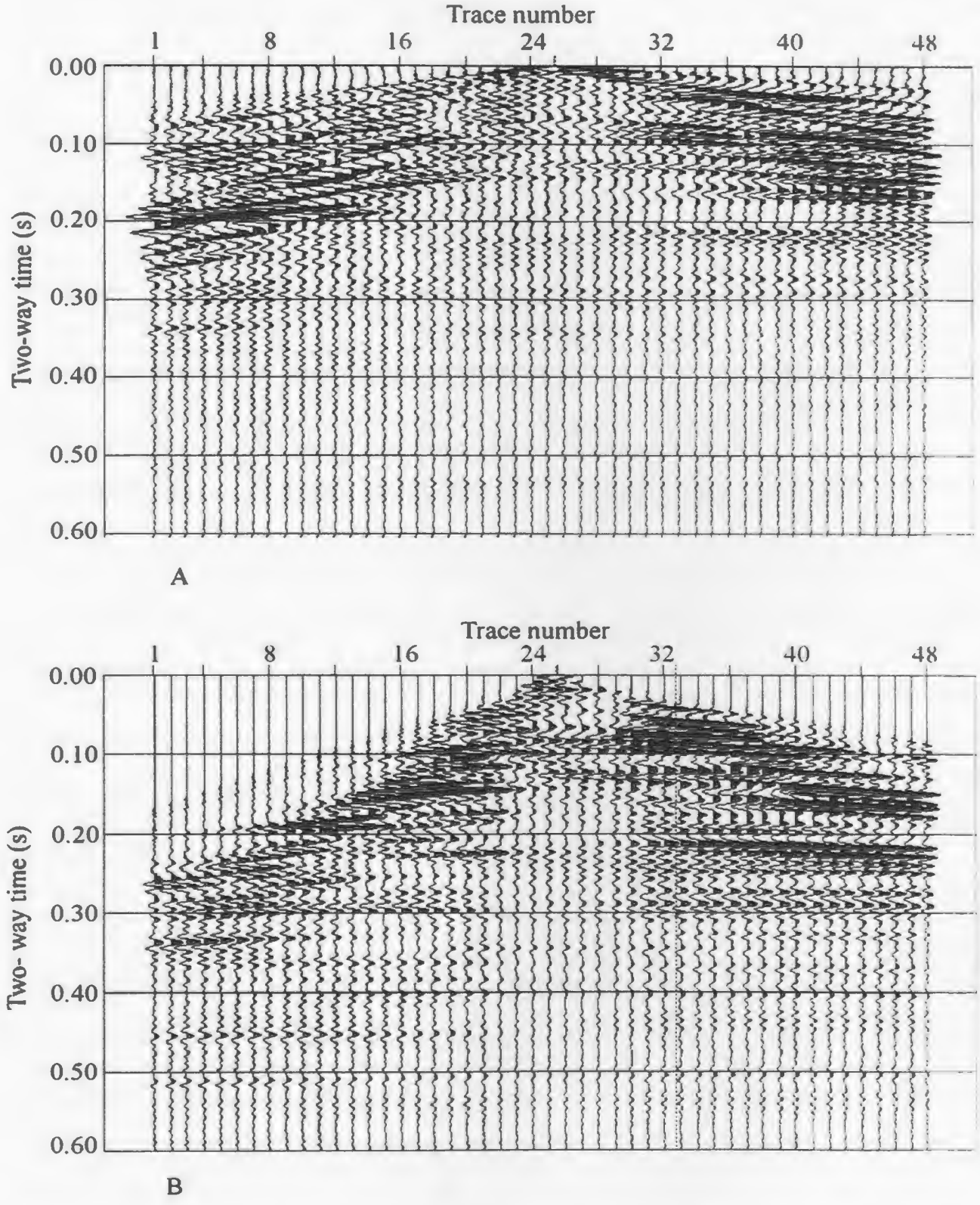

Figure 4.3.6.3-1: HVF-filtered CDP 3650 (A) before and (B) after DMO correction. DMO correction improved velocity analysis considerably. Note that reflector assymetry has been reduced in (B).

4.3.7 Muting and stack.

NMO correction to CMP data causes distortion of the dominant frequency in the data. The dominant period is stretched, and frequency is thus lowered. NMO stretching is quantified as (Yilmaz, 1987);

$$\frac{\Delta f}{f} = \frac{\Delta t_{NMO}}{t(0)} \tag{29}$$

where f is the dominant frequency, Δf the change in frequency, Δt_{NMO} the change in hyperbolic moveout time, and t(0) the zero-offset time. NMO stretching is severe at early times and large offsets since these correspond to the largest moveout before NMO correction. Since some of the moveout is due to residual static time shifts, it is advisable to apply residual static corrections before muting to reduce stretch effect.

Muting refers to the removal of severely NMO stretched events, as well as any other event which may be undesirable to include in the stacked section (ground-coupled air waves, refractions, and direct waves). The design of a mute is accomplished by trial and error until the unwanted event is removed with minimum damage to the data. An automatic top mute of 35% stretch tolerance was applied to the data during NMO correction.

Common depth point (CDP) data contains a redundancy of sampling equal to the fold of coverage. CDP stacking refers to the summation of all the traces in a CDP gather to produce one output trace. Such CDP stacking improves the S/N ratio by $\sqrt{n}$, where n is the fold of coverage. Also, the S/N ratio is enhanced by preferentially staking multiples out of phase due to the effect of NMO correction. There exist a number of CDP stacking schemes, each appropriate for a specific processing objective. The details of stack weighting criteria are discussed in Naess and Bruland (1985). In the present exercise a mean power stack was applied to the data set. This is basically a type of diversity stack wherein some coherency measure is used to calculate and weight the energy in successive time gates. The prestack processing options are summarised in Table 4-4.

Table 4-4: A summary and appraisal of the prestack processes used on the seismic data.

Process	Options	Goal	Performance
Refraction Statics		determine static corrections	good
Data filtering	Frequency: spectral balancing	remove noise	fair
	f-k dip filtering	remove coherent noise	data aliased
	HVF	remove ground roll	good, data re-sampled
Velocity analysis	T^2-X^2	stacking velocities, reflector dip	fair, low S/N
	Constant Velocity Stacks	RMS velocities for NMO correction	poor, low S/N
	Semblance analysis, DMO	RMS velocities for NMO correction	good

4.4 Poststack Processing

4.4.1 Residual Statics

NMO correction is intended to line up reflections on CMP data such that the traces will stack at maximum power. Irregularities on reflection events may however occur as small static time shifts between traces in the same CMP gather. These static time shifts occur for a number of reasons, including topographic differences at source and receiver locations, lateral velocity variation in the near-surface layering, and structural variation along the reflecting horizon (Yilmaz, 1987; Ronen and Claerbout, 1985; Nickerson, 1993). Assuming that the observed static time shifts are surface-consistent (i.e. they depend only on the surface location of sources and receivers) allows one to decompose the static travel time into various components through the relation (Ronen and Claerbout, 1985; Yilmaz, 1987);

$$t_{ijh} = s_j + r_i + G_{kh} + M_{kh} x_{ij}^2 \tag{30}$$

where s_j is the residual static time shift at the j^{th} source, r_i the residual static time shift at the i^{th} receiver, G_{kh} the difference in two-way travel time at a reference CMP and the k^{th} CMP location along horizon h (structural component), and M_{kh} is the residual NMO component along horizon h. The assumption of surface consistency relies on all ray paths being vertical beneath sources and receivers at all offsets. The fact that accurate residual

static time corrections are routinely obtained from seismic data confirms the validity of the assumption to some extent (Ronen and Claerbout, 1985).

In practice, the initial time shifts are picked on CMP data and decomposed into the various components using an automatic procedure. The most common algorithm for static travel time picking is the Ronen-Claerbout (1985) scheme. The algorithm obtains static shift travel times by picking maxima on a crosscorrelation between a pilot trace and every trace on the CMP. The redundancy contained in CMP data allows a solution to (30) to be obtained from the seismic data through the Ronen-Claerbout algorithm. A modification of this algorithm allows residual statics to be calculated from stacked CMP data which is less time-consuming and was found to be effective on the present data. Here the stacked section is divided into equal segments from which a pilot trace is calculated. Every trace in the segment is then cross-correlated with the pilot trace.

Examination of the stacked section showed some misalignment on the reflection events. The residual static calculation was performed on a 150-200 ms correlation window, with a maximum allowable shift of 10 ms. These values were arrived at after several trials and examination of the stacked section after each run.

4.4.2 F-X Deconvolution

Predictive deconvolution in the time domain removes predictable coherent noise like multiples from a seismogram. When used with a unit prediction length, it improves temporal resolution by contracting the seismic wavelet. The details of predictive deconvolution are discussed in section 4.3.5. It suffices here to say that the same basic principles of temporal deconvolution apply in the f-x domain. In the following section we examine some of the salient features of f-x deconvolution.

Forward Fourier transformation takes seismic data into the f-x domain. In this domain events that are linear in the x-direction are predictable by a one-step-ahead prediction operator (Gulunay, 1986; Fokkema et al., 1990). The basic theorem is formulated as follows: For a given times series input of length N,

$$u_1 u_2 u_3 \ldots u_N,$$

there exists a filter of length M, such that

$$u_{k+1} = f_1 u_k + f_2 u_{k-1} + \ldots f_m u_{k-m+1} \tag{31}$$

The above relation may be expressed as a convolution. Thus,

$$u_t * f_i = u_{t+1} \tag{32}$$

where u_{t+1} is a one-step advanced version of u_t. The convolution operation implies that there must exist a filter such that

$$(1,-f_1,-f_2,\ldots -f_m)*(u_1u_2\ldots u_N)=(1,0,0,\ldots,0) \tag{33}$$

where u_1 is the irreducible first part of the input. The filter coefficient series in (33) is called the prediction error operator (Gulunay, 1986).

A dipping event in t-x space is described by

$$t=c+mx \tag{34}$$

where c is the intercept, and m is the slope. The analogous expression for the same event in f-x space is

$$e^{i2\pi fc}.e^{i2\pi fmx} \tag{35}$$

For events with conflicting dips, Gulunay (1986) has shown that the f-x prediction operator is impractical by using the polynomial equation;

$$1+x+x^2+\ldots+x^n=\frac{1-x^{n+1}}{1-x} \tag{36}$$

and the z-transform, with $x = ze^{ik\Delta x}$. One considers two events of different slopes:

$$A_1(z)=1+ze^{ik_1\Delta x}+z^2e^{ik_2 2\Delta x}+\ldots, \tag{37}$$

$$A_2(z)=1+ze^{ik_2\Delta x}+z^2e^{ik_2 2\Delta x}+.... \tag{38}$$

The problem is to find the inverse of $A_1(z) + A_2(z)$. If we let

$$a=\left(e^{ik_1\Delta x}+e^{ik_2\Delta x}\right) \tag{39}$$

and

$$b=e^{i(k_1+k_2)\Delta x} \tag{40}$$

then after algebraic manipulation, one obtains;

$$\frac{1}{A_1(z)+A_2(z)}=\frac{1}{2}\left[(1-az)+(b-a^2)\frac{z^2}{1-az}\right] \tag{41}$$

We may see from (41) that unless $b = a^2$, the inverse contains infinitely many terms, but if $b = a^2$, then we have that

$$e^{i(k_1+k_2)\Delta x}=\left(3^{ik_1\Delta x}+e^{ik_2\Delta x}\right)^2 \tag{42}$$

Since this equation is only true if $k_1 = k_2$, (i.e when the slopes are equal) it follows that the f-x prediction operator can not work on events with conflicting dips (Gulunay, 1986).

The effect of f-x deconvolution on seismic data is to predict and preserve only coherent reflection events and attenuate random noise. It has also been applied successfully to

remove ground roll from stacked seismic sections (Gulunay, 1986). Since the f-x prediction operator also acts as a shaping filter in the x-direction (33), it leads to improved lateral coherency on a stacked section. No frequency content is lost through application of f-x deconvolution, hence it is superior to conventional coherency enhancement techniques such as lateral trace mixing.

F-x deconvolution was applied to the present data primarily because of excessive noise due to a ground-coupled air wave. This noise train could not be satisfactorily removed prestack because it had a broad band frequency. The f-x deconvolution parameters used were an 11 sample prediction length, a frequency bandwidth of 20-80 Hz, and a 10% add back option. The latter is important if the f-x deconvolution operator tends to attenuate dipping trends of structural significance, such as faults. The f-x filter performance was found to be excellent. The effects of lateral trace mixing and f-x deconvolution on the stacked section are illustrated in figures 4.4.2-1 and 4.4.2-2 (in the back pocket).

4.4.3 Migration

The aim of migration on a stacked time section is to restore dipping structures to their correct subsurface locations, remove diffractions, and improve lateral resolution (Ramananantoandro, 1995). Displacement of dipping structures in the updip direction is

not significant on shallow seismic reflection sections because the time and spatial sampling intervals are typically small. This fact generally defeats the purpose of applying migration algorithms to shallow seismic sections. Black et al. (1994) discuss simple migration equations which may be used to predict quantitatively the effect that migration would have on a given seismic reflection section. The horizontal (d_x) and vertical (d_t) reflector displacement effected by migration is described by (Black et al., 1994):

$$d_x = v^2 t \frac{D_{ut}}{4} \tag{43}$$

and

$$d_t = t\left(1 - \sqrt{\left(1 - \left(\frac{vD_{ut}}{2}\right)^2\right)}\right) \tag{44}$$

where v is the RMS velocity, t is the two-way travel time, and D_{ut} is the reflector dip.

In shallow reflection surveys, migration is performed to enhance reflector lateral resolution rather than structural effects. The resolution at which a reflector appears on the seismic section depends on the width of the Fresnel zone. Events that fall within one quarter of the dominant wavelength belong to the same Fresnel zone. They add constructively to produce one blurry image. If the width of the Fresnel zone is reduced, closely-spaced samples are resolved since they then fall into separate Fresnel zones. That this effect is achieved satisfactorily by migration has been documented by

Ramananantoandro (1995). The result of a phase shift time migration (Gazdag, 1978) are shown in figure 4.4.3-1 (in the back pocket). The lateral resolution on the time section was noticeably increased after migration. A lateral mixing of five adjacent traces was applied on the migrated section with the ratio 0.5:0.75:1:0.75:0.5. A phase shift depth migration was also performed on the stacked section for geological and structural interpretation. The depth section is discussed in chapter 6.2.

4.5 Summary of results and observations

Refraction statics analysis produced a two layer velocity-depth model (fig. 4.3.2-2). The model shows a low velocity ($\sim$600 m/s) surface layer to a depth of $\sim$15 m. The underlying layer shows seismic velocities of 1600-1800 m/s. The refraction static time shifts indicate small anomalies except at shot 4155.

Velocity analysis was difficult on the present data set because of the low S/N ratio and also the presence of dipping reflectors. DMO correction was used to improve the performance of semblance velocity analysis. The velocities picked in semblance analysis were updated with values obtained from the T^2-X^2 method. The latter method also allowed determination of reflector dip along the line (Table 4-2). Constant velocity stacking (CVS) was unsuccessful because of the low S/N ratio.

The migrated time section (fig. 4.4.3-1) shows strong reflectivity at 0-0.40 s in the southeast. Strong wide angle reflections occur at 0.10 s and 0.20 s. These bright horizons were further analyzed in order to determine their likely cause. The time section shows no reflectivity below 0.40 s in the southeast. The material below 0.40 s has high seismic velocity. The reflective horizons above 0.40 s in the southeast are subhorizontal. The reflectivity in the northwest is low, but persists to ~0.45 s. The reflective layers in this area are dipping gently to the northwest.

5.0 INTERPRETIVE PROCESSING

The processing techniques discussed in the previous chapter involve the manipulation of field data for the removal of noise and both dynamic and static time shifts. The resulting seismic section may then be interpreted in terms of horizon velocity and visible structure. Certain features of seismic data such as bright spots cannot, however, be quantified without further inversion for particular elastic parameters. Inversion algorithms for AVO and pseudo-acoustic impedance are available in the Hampson-Russell® suite of programs. The time section derived in the previous section (fig. 4.4.3-1) shows that there are some high amplitude reflections at CDP's 5200-5380 (fig. 5-1). These wide angle reflections were investigated for the probable cause using Strata® and AVO inversions.

5.1 AVO Analysis

AVO refers to the variation of reflection amplitude with increasing offset from the shot point. Under normal circumstances such variation is minimal and does not cause visible anomalies on the reflection seismogram. There are instances, however, when ground conditions cause an anomalous change in AVO, resulting in "bright spots" associated with certain horizons.

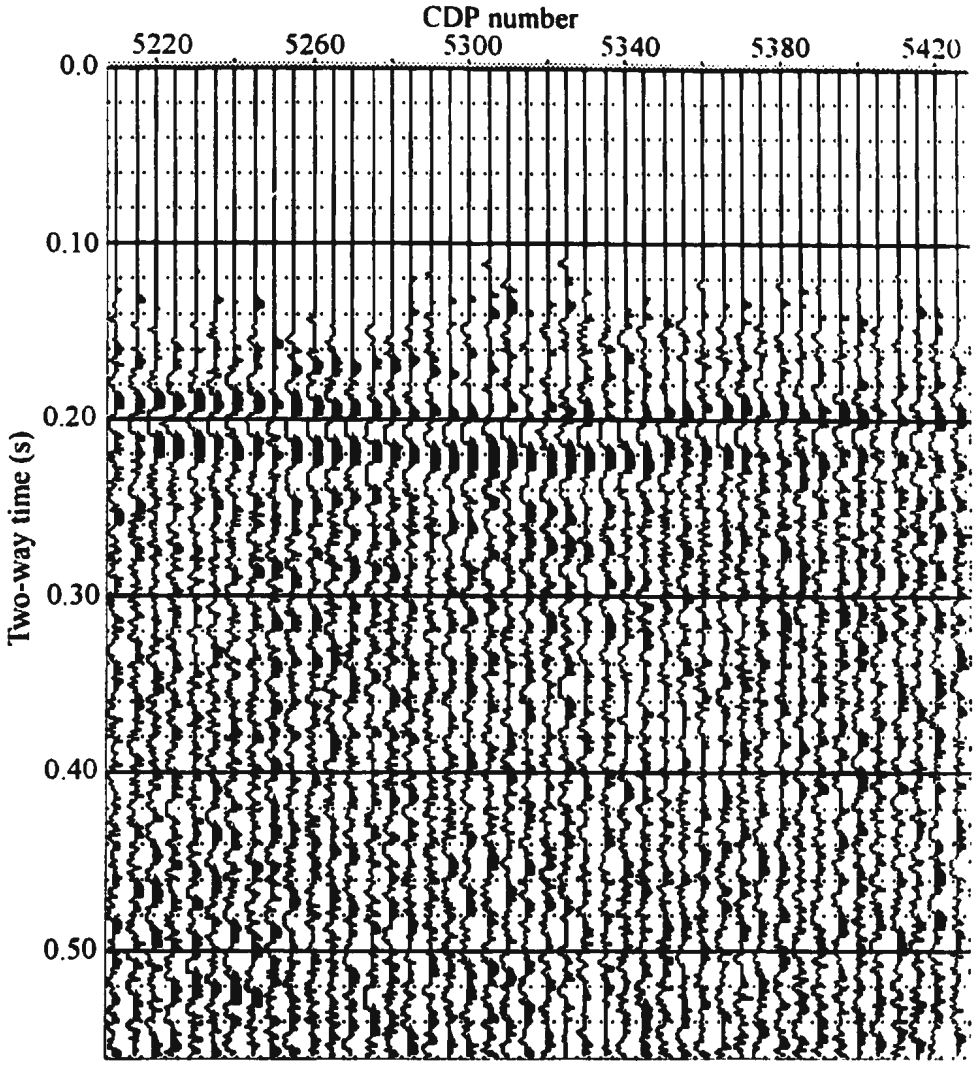

Figure 5-1: An offset-limited stack showing a strong wide-angle reflection at ~190-220 ms. The stack comprises the offset range 111-218 m.

The occurrence of bright spots on stacked seismic data is used as an indicator of gas accumulations in the petroleum industry. However, some bright spots may not be related to gas accumulations (Ostrander, 1984). The analysis of the variation of reflection amplitude with offset (AVO) is intended to infer and perhaps quantify elastic rock properties which are diagnostic of bright spot production. One such elastic property is the Poisson's ratio, σ;

$$\sigma = \frac{\left(\frac{v_p}{v_s}\right)^2 - 2}{2\left[\left(\frac{v_p}{v_s}\right)^2 - 1\right]} \tag{45}$$

where v_p and v_s are the compressional and shear wave velocities. Common rock formations have σ values in the range 0.0-0.5. Gas sands have values of ~ 0.1, while brine-saturated sands have values of ~ 0.4 (Ostrander, 1984).

In normal incidence reflection profiling there is usually only a small amplitude variation with offset. It has been shown, however, that when there is a large change in σ across a reflecting interface, there occurs an anomalous variation of reflection amplitudes with offset (Ostrander, 1984). Furthermore, the reflection coefficients either decrease or increase algebraically with increasing offset depending on whether a lower or higher Poisson's ratio occurs in the bottom layer. The reflection coefficient amplitudes remain more-or-less constant in the absence of a gas sand. Gassaway et al. (1986) note that

bright spots may also be caused by subtle facies changes wherein silica is replaced by carbonate cement. In this instance one typically observes an increase in both the p-wave velocity and Poisson's ratio with increasing offset. It follows therefore that a gas sand should have both a lower p-wave velocity and lower Poisson's ratio.

AVO analysis was applied to the present data because of the presence of high amplitude reflections on the stacked section at ~200 ms (fig. 5-1). The geological section is inferred from electrical resistivity soundings of Hutchins et al. (1977) to comprise an alternating sequence of clays and semi-consolidated sands down to 300 ms. Since the data was collected from a relatively unexplored area, no well logs were available. A pseudo-sonic log was created using RMS velocities derived from stacking of the seismic data. The density log was derived from the RMS velocities using Gardner's equation (Hampson-Russell®, program documentation, 1994). Constraints on the density log were imposed using published density values for some of the formations. The initial σ value was set constant at 0.4 for unconsolidated brine-saturated sands[9]. These initial constraints were perturbed through several algorithms included in the AVO modelling program to produce a synthetic seismic model that best approximates the seismic data.

---

[9] Electrical resistivity soundings in the area indicate very low formation resistivities, implying that either the aquifers are brine-saturated or the horizons consist of clays/shales (Hutchins et al., 1977).

The horizon under consideration is indicated by an arrow in figure 5.1-1. The p-wave velocity increases from 1800 to 2800 m/s at the top of the horizon (~ 148 m). This increase in compressional wave velocity corresponds to a drop in σ from 0.30 to 0.18. At the base of the horizon (~ 177 m), the p-wave velocity decreases from 2800 to 2600 m/s, with a corresponding increase in σ from 0.18 to 0.24. The reflectivity response of these events is presented graphically in figure 5.1-2. At ~ 148 m, the amplitudes of both the reflected p-wave (PR) and s-wave (SR) decrease algebraically with increasing angle of incidence. The reflected s-wave is affected slightly more than the p-wave[10]. At ~ 177 m, the reflected s-wave reflection amplitude increases with increasing offset to 0.12 at 32° (125 m), and then decreases to 0.08 at 48° (218 m). The p-wave reflection coefficient increases from -0.08 at 0° to +0.02 at 48°. Overall, the reflection coefficients are decreasing at the top interface and increasing at lower interface.

---

[10]$\Delta PR = 0.20 - 0.10 = 0.10$, and $\Delta SR = 0.0 - 0.15 = -0.15$ (fig. 5.1-2). n.b. the reflected s-wave was derived by the program from the input p-wave pseudo-log.

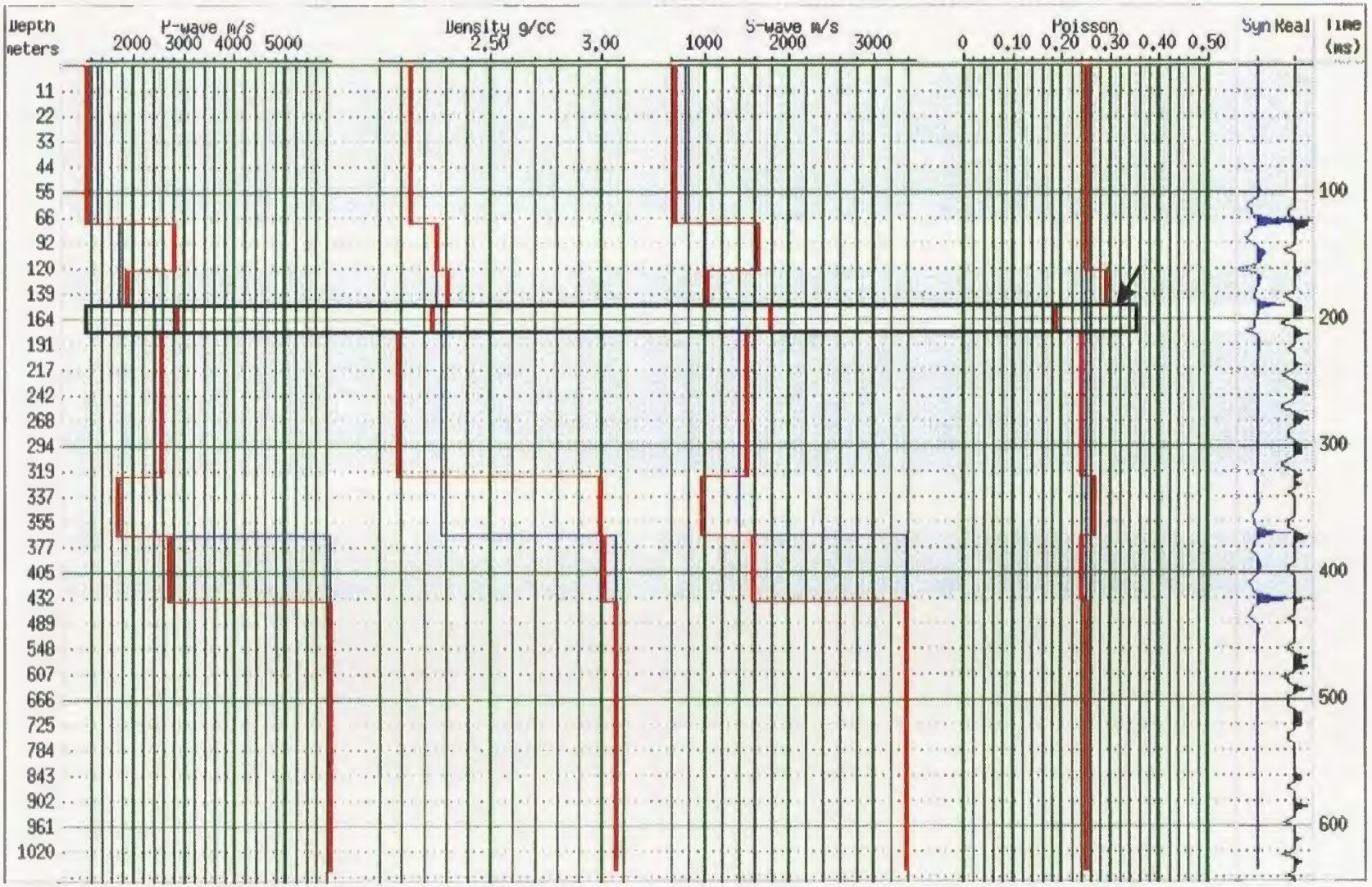

Figure 5.1-1: AVO inversion showing the response of the bright spot at 189-209 ms. The horizon of interest is indicated by the arrow to the left of the Poisson's ratio log.

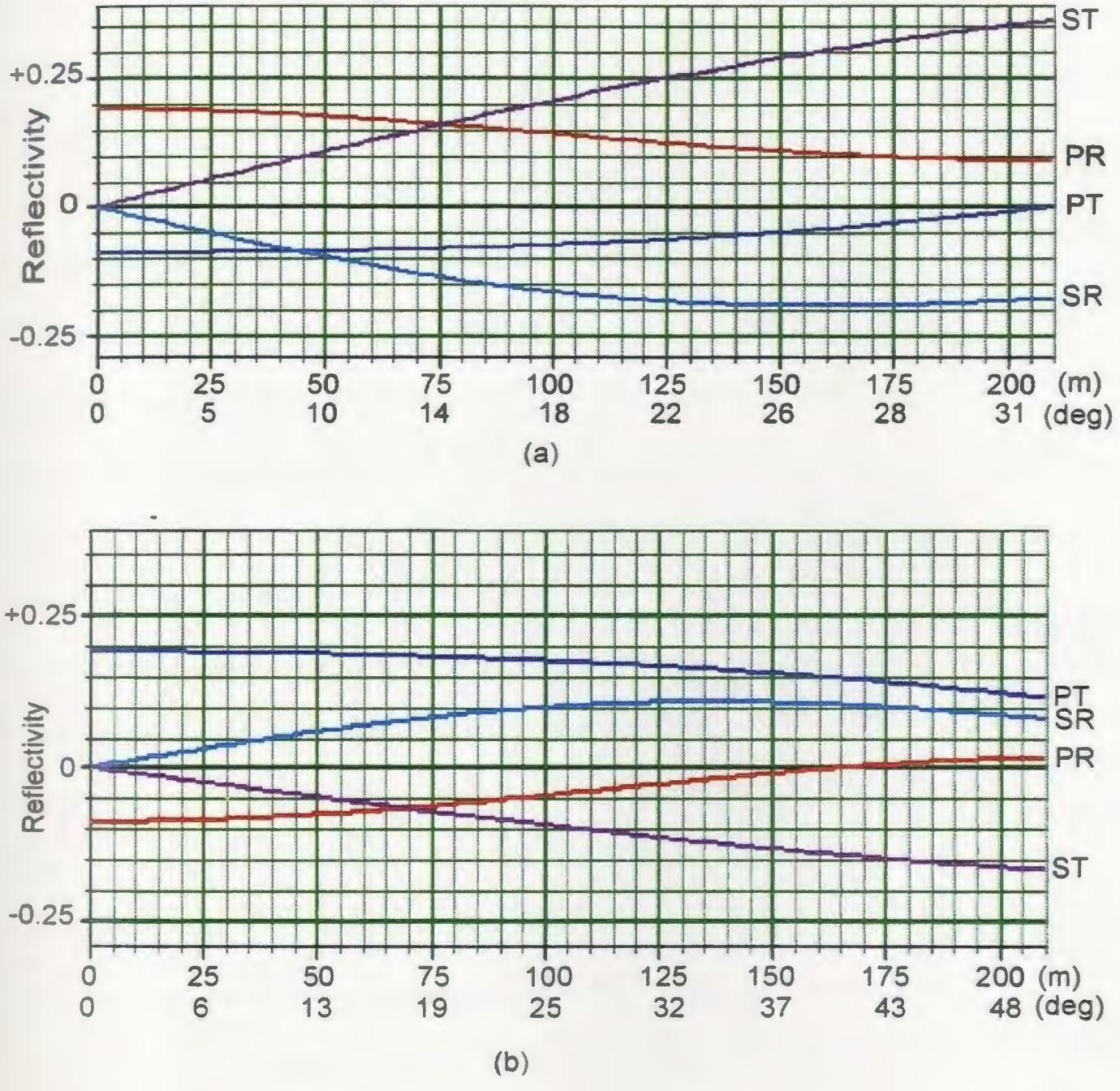

Figure 5.1-2: AVO reflectivity response curves for the modelled bright spot. (a) top reflector at 147.9 m. 189 ms. (b) bottom reflector at 177.3 m. 209 5 ms

The above discussion indicates that the horizon above 147.9 m is probably brine-saturated (high σ). The lower horizon (below 147.9 m) has a lower brine saturation, and also a different matrix composition (lower σ, higher ν_p). This scenario is similar to the ones studied by Gassaway et al. (1986) wherein bright spots were found to be related to a subtle facies change. Since the change in σ across the two horizons is relatively small (0.12), and the variation in reflection amplitudes is also small, it is concluded that the observed anomaly is caused by a facies change at the base of the Kalahari beds. Moreover, the bright horizon shows a lower σ, and a higher p-wave velocity.

5.2 Strata® Inversion

A portion of the stacked seismic section was examined in the Hampson-Russell® program Strata. The required input to Strata® include sonic and density logs. However, in the absence of recorded logs, a pseudo-sonic log may be constructed from RMS velocities determined by velocity analysis. A pseudo-density log may then be derived from the latter by Gardner's equation;

$$\rho = a v^{b} \tag{46}$$

where a and b are constants. These constants are variable for different formations. For the present data the constants were varied until the density log assumed reasonable values for the expected lithologies. Density values for these formations were extrapolated from drilling results of Meixner and Peart (1984), density estimates from the gravity survey of Ngamiland (Reeves, 1978), and horizontal seismic velocities established by Greenwood and Carruthers (1973) at selected stratigraphic boreholes. These sources establish a density of ~ 2.14 g/cm^3 for Kalahari beds, and ~ 2.65 g/cm^3 for non-igneous basement.

A blocky velocity inversion of part of the stacked section is shown in figure 5.2-1. The velocity model shows that the section comprises four distinct geologic units with subhorizontal boundaries. The top layer comprises all geological horizons with a p-wave velocity of $v_p \leq 2153$ m/s (fig. 5.2-1). The layer starts at the surface and reaches a total depth of ~ 191 m, and has an average p-wave velocity of 1827 m/s. Some isolated units of the same velocity range occur in the lower horizon. These may be lenses of saturated sandstones within otherwise consolidated shales. The base of the top layer coincides with the bright spot discussed in section 5.1. The velocity range, density distribution, and Poisson's ratio (fig. 5.1-1), of the top layer indicate that it may constitute the Kalahari sequence.

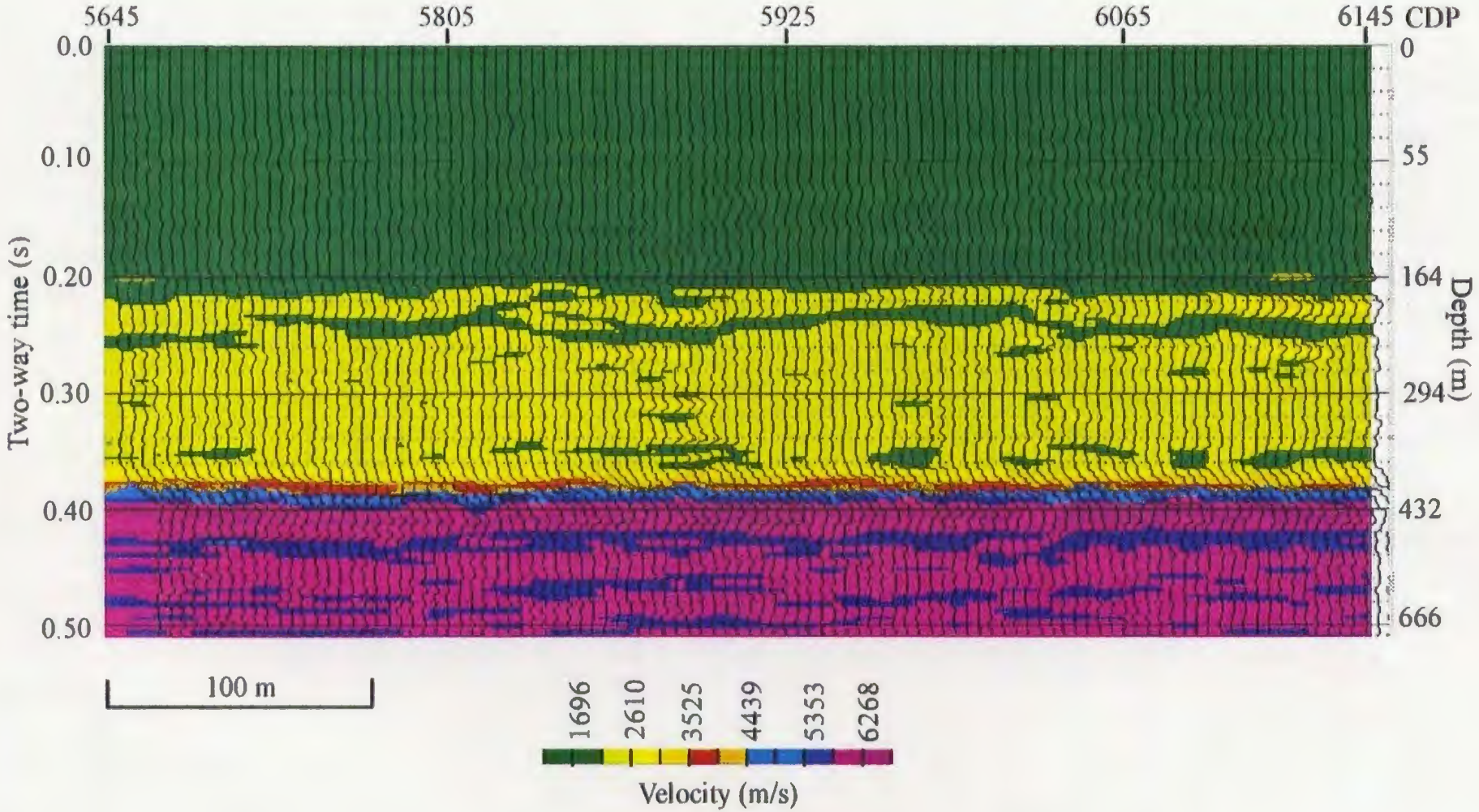

Figure 5.2-1: A blocky velocity inversion of the stacked section south of the Kunyere Fault

Below the Kalahari beds occurs a horizon from 191 to 377 m (fig. 5.2-1). The unit has p-wave velocities in the range $2153 \leq v_p \leq 3525$ m/s. The layer is ~186 m thick. The velocity range of this unit is similar to that established for Karoo sediments at Lake Ngami by Greenwood and Carruthers (1973). The latter were not, however, able to image these Karoo beds on their seismic line A (fig. 3-2). These Karoo sediments are without the capping basaltic lava that is associated with the Karoo succession elsewhere in the country. There exists a thin, high velocity layer at the base of the Karoo beds (brown/blue in fig. 5.2-1). This unit occurs at 380-390 ms, and at an average velocity of 4439 m/s, has a thickness of ~22 m. The velocity range of $3525 \leq v_p \leq 5353$ m/s is indicative of igneous rock material. Furthermore, the horizon is persistent and has a uniform thickness across the section. The foregoing strongly suggests that the horizon is a basaltic sill intruded at the base of the Karoo sequence. Occurrences of such basaltic sills have been reported elsewhere within the Karoo sub-basins (e.g. Farr et al., 1981). The lowermost unit comprises high velocity material in the range $5353 \leq v_p \leq 6268$ m/s. At the depths considered in the present work, it is likely that this basement comprises igneous rock material.

In summary, the blocky velocity inversion reveals a stratigraphic sequence comprising 377 m of Kalahari and Karoo sediments, underlain by a basaltic sill 22 m thick. The basement is an igneous rock intrusion.

6.0 INTERPRETATION

6.1 Refraction Statics Model

The near-surface velocity model for the seismic line is discussed in section 4.3.2 and shown in figure 4.3.2-2. The model shows a surface layer with a thickness of ~15 m and a velocity ≤600 m/s. This top layer constitutes the unsaturated zone composed of loose sand, crete, and clays. The lateral velocity profile (fig. 4.3.2-2) shows that all horizons below this zone have velocities ≥1600 m/s, hence they are either saturated or semi-consolidated. The free water table was observed at 14.5 m in a hand-dug well near the seismic line (~100 m south of shot point 1945). The short and long wavelength statics model in figure 4.3.2-2 indicates a marked anomaly between shot points 3755 and 4145. This anomaly shows an abrupt increase in thickness of the unsaturated zone and a pinchout of the layer below it. This brings the half-space into contact with the unsaturated zone. The area around this anomaly was observed in the field to support healthy tree vegetation, while away from the anomaly, the vegetation is stunted tree scrub. Based on these observations, it appears that the horizon immediately below the unsaturated zone is impermeable to groundwater flow. This scenario corroborates the findings of BRGM (1984) and SMEC (1987) near Maun that the Kalahari sequence comprises ~10 m of unsaturated clays and sands lying over ~40-50 m of plastic clay (fig. 2.3-2). The material comprising the half-space would in this case be the lower Kalahari beds.

6.2 Seismic Section

An interpretation of the migrated depth section is shown in figure 6.2-1 (in the pocket). The geologic units were derived by tracing prominent reflectors across the section. Information from velocity analysis and inversion (Strata®) was used to assign the geologic horizons to established stratigraphic units. The structural elements were drawn at locations where the geologic horizons indicated possible displacement. In this section, the near-surface geologic units described in section 6.1 are included as part of the top unit.

Figure 6.2-1 comprises four different geologic units determined on the basis of average formation velocity, local geology, and the continuity of reflector boundaries. The geologic unit coded yellow occurs from the surface to ~200 m at CDP's 4460-6145. The sedimentary bedding trends indicate that this unit is buried on the left-hand side of figure 6.2-1 (CDP's 1130-4460). The top of the unit migrates downward through a series of northwest dipping faults, to a depth of ~155 m at CDP 1130. Velocity analysis and inversion have indicated that this unit has an average velocity of 1827 m/s in the southeast, increasing laterally to ~3000 m/s in the northwest (see also fig. 4.3.2-2). The formation has an average thickness of ~200 m (CDP's 4575-6145) in the southeast, and ~230 m in the northwest at CDP 1130. The lateral increase in velocity is probably caused by increase in cementation due to increasing depth of burial. The total downward displacement of the geologic unit is ~155 m. Examination of the blocky velocity

inversion in figure 5.2-1 indicates that this unit has physical properties consistent with the Kalahari beds. The top formations of this unit were clearly imaged in the refraction statics model (fig. 4.3.2-2).

The light green unit on the top left corner of figure 6.2-1 (CDP's 1130-4460) shows regressive sedimentary structures. These regressive beds all dip to the northwest in contrast to the unit on the top right corner which shows subhorizontal bedding. The sedimentary form, and the lower average formation velocity (1600 m/s) (fig. 4.3.2-2 and Table 4-2), form the basis for assigning the formation to the Okavango rather than the Kalahari Beds. The Okavango sediments are terminated by a northwest dipping fault at CDP 4460, where the unit is ~45 m thick. The beds increase in thickness to ~ 155 m at CDP 1130. The refraction static anomaly described in section 6.1 coincides with the fault contact between the Okavango and Kalahari beds. Since this feature provides hydraulic continuity between surface flow and the lower permeable layers, it is likely that it may be a recharge point. Furthermore, the feature impounds against a fault structure, which may act as a conduit for recharge into the underlying Karoo beds. It is likely that the feature may be a buried paleaofluvial system, in which case it could contain sand aggregate deposits similar to the Shashe river aquifer. The anomalous feature may have hydraulic continuity with the Kalahari beds. The latter contain saline fossil groundwater (Neumann-Redlin, 1980). Indications from velocity analysis are that the Okavango beds may comprise alternating layers of semi-consolidated clays and sandstones.

The basal sedimentary unit (brown) was delineated on the basis of velocity analysis and inversion. The horizon occurs at 200-380 m in the southeast and 380-565 m in the northwest. The average formation velocity in the southeast is 2839 m/s. The formation is 180 m thick in the SE and 185 m in the extreme northwest at CDP 1130. The average velocity in this area has increased to 3255 m/s. Velocity inversion and the AVO pseudo-logs (fig. 5.1-1) indicate that the formation contains some intercalations of lower velocity members. The Poisson's ratio log (fig. 5.1-1) indicates increased water saturation at a depth of 320-377 m. The p-wave velocity log shows a decrease in velocity at the same depth interval. This suggests the presence of a high saturation, low velocity horizon within the sequence. The average formation velocity in general points to a consolidated sandstone. Indeed, similar seismic velocities were established for the Karoo sediments at Lake Ngami by Greenwood and Carruthers (1973). These Karoo beds are underlain by a thin (22 m), high velocity layer in the southeast at CDP's 5645-6145 (fig. 5.2-1). The layer is likely to be a mafic sill, since its average seismic velocity is 4439 m/s. This velocity range is typical of mafic intrusions. Furthermore, mafic sills occur at the base of the Karoo in the Central sub-basin (Farr et al., 1981). A salient feature of the formation described so far is the absence of a capping basalt sheet associated with the Karoo elsewhere in the country. Although the occurrence of the such a basalt sheet is suggested in Greenwood and Carruthers (1973), there is no indication of it on the present seismic reflection section. In fact, the magnetic anomaly thought to suggest its existence can be attributed to the faulted structure at CDP's 4360-4460 (fig. 6.2-1).

The absence of the basalt sheet over the Karoo may allow hydraulic continuity between the latter and the Kalahari beds. This may lead to deterioration of water quality by saline recharge. However, shaly aquicludes of the Kalahari beds may occur above the main aquifer.

The basement underlying the sedimentary pile described above shows a consistently high velocity of 5353-6268 m/s. This velocity suggests that it is probably a massive mafic body.

6.3 Aeromagnetic data

The goal of reconnaissance aeromagnetic surveys is to establish the approximate depth to magnetic sources and to delineate regional magnetic trends of basement features. The determination of depth to magnetic sources was difficult because of the reconnaissance nature of the data (too wide line spacing). This makes it inappropriate to apply depth inversion routines such as Euler deconvolution and straight slope methods (Barongo, 1984; Ram Babu et al., 1986; Reid et al., 1990). Depth determination by Euler deconvolution is limited to a minimum depth equal to the profile spacing. The profile spacing of 4 km exceeds the anticipated depths to magnetic basement in Northwest Botswana. Furthermore, the straight slope method of Ram Babu et al. (1986) requires

unbiased contouring of the magnetic anomalies. This was difficult to achieve at the present profile spacing. It was therefore decided to employ a statistical approach introduced by Spector and Grant (1970) and discussed by Naidu (1970) in order to derive depth estimations. This involves analysis of the power spectrum of the total magnetic field. The depth, d, to magnetic basement is obtained from the plot of the power spectrum using the equation (Spector and Grant, 1970);

$$d=\frac{-s}{4\pi} \tag{47}$$

where s is the average slope of a segment of the graph.

Interpretation of the aeromagnetic data was performed by tracing all linear and two-dimensional anomalies visible on the different residual maps onto the same overlay. The various anomaly trends thus obtained were overwritten onto the total field pole-reduced anomaly map (fig. 2.1.4-1). The structural domains delineated in this manner define two categories.

First, a system of sinuous magnetic anomalies occurs with a northeast trend. These anomalies correspond to the Damara metamorphic belt in the north and the Ghanzi-Chobe fold belt in the south. The magnetic anomalies along the Damara belt are likely to be a response from infolded basic rocks and/or magnetic metamorphic products. In the

northeast quadrant of the map, that underlying the Okavango delta, the sinuous Damara magnetic anomalies are replaced by straight lineaments. These lineaments represent parallel graben faulting that defines the Okavango delta. The magnetic signature underlying the Okavango delta seems to preclude the existence of Damara rocks beneath the delta. The Damara belt swings to a northerly trend at the southwest edge of the delta. The material beneath the delta is therefore likely to be Archean basement.

Secondly, a dense swarm of magnetic highs are present with a northwest trend. These positive magnetic anomalies are due to a dolerite dike swarm emanating from the Lebombo-Sabi failed rift at Nuanetsi in the east (Ellam and Cox, 1989; Reeves and Hutchins, 1982). The dike swarm is 78 km wide southeast of the delta, tapering down to 35 km northwest of the Okavango delta. The dike structures truncate the rift graben in the southwest. In fact, the graben faults terminate in the vicinity of the dike swarm. Although the dikes are themselves affected by the faulting, they show no appreciable horizontal displacement. This fact implies that the rift faulting is primarily caused by normal crustal extension.

The present seismic reflection line falls within the post-Karoo dike swarm discussed above. This confirms the seismic finding that the basement at Marophe comprises basic intrusive rocks. Furthermore, the seismic line runs parallel to the dike swarm. The depth, d, to magnetic basement in the vicinity of the delta was determined to be $200 < d \leq$

500 $\pm$100 m (figs. 6.3-1 to 6.3-3). This result agrees closely with that established from the seismic (figs. 5.1-1, 5.2-1, and 6.2-1) wherein the basement is encountered at ~377 m south of the Kunyere fault and ~570 m north of the fault. It will be noted in figure 6.2-1 that the basement is plunging to the northwest. As such, the depth difference at the opposite ends of the seismic line may not be entirely due to fault displacement.

The calculated depths to magnetic sources for the area northwest and west of the Okavango Delta indicate the presence of deep sources at 2.3 km (fig. 6.3-1). The shallowest magnetic features occur at 0.3 km. Ludtke (1986) describes some isolated outcrops of Nosib quartzite at Tsodilo hills. These strata contain abundant detrital magnetite horizons. Over the Okavango delta, (fig. 6.3-3) deep magnetic sources occur at 2.2 km. In general, shallow magnetic basement occurs at ~500 m. The area indicates a markedly increased thickness of non-magnetic cover. This is consistent with increased sediment thickness being caused by fluvial deposition within the confines of the delta. The results show that magnetic basement does not outcrop anywhere within the delta. Figure 6.3-2 depicts a scenario similar to the one in figure 6.3-1. Deep magnetic sources occur at 2.5 km. Within observation error, the estimated depths agree well with the known and inferred geological situation in Ngamiland.

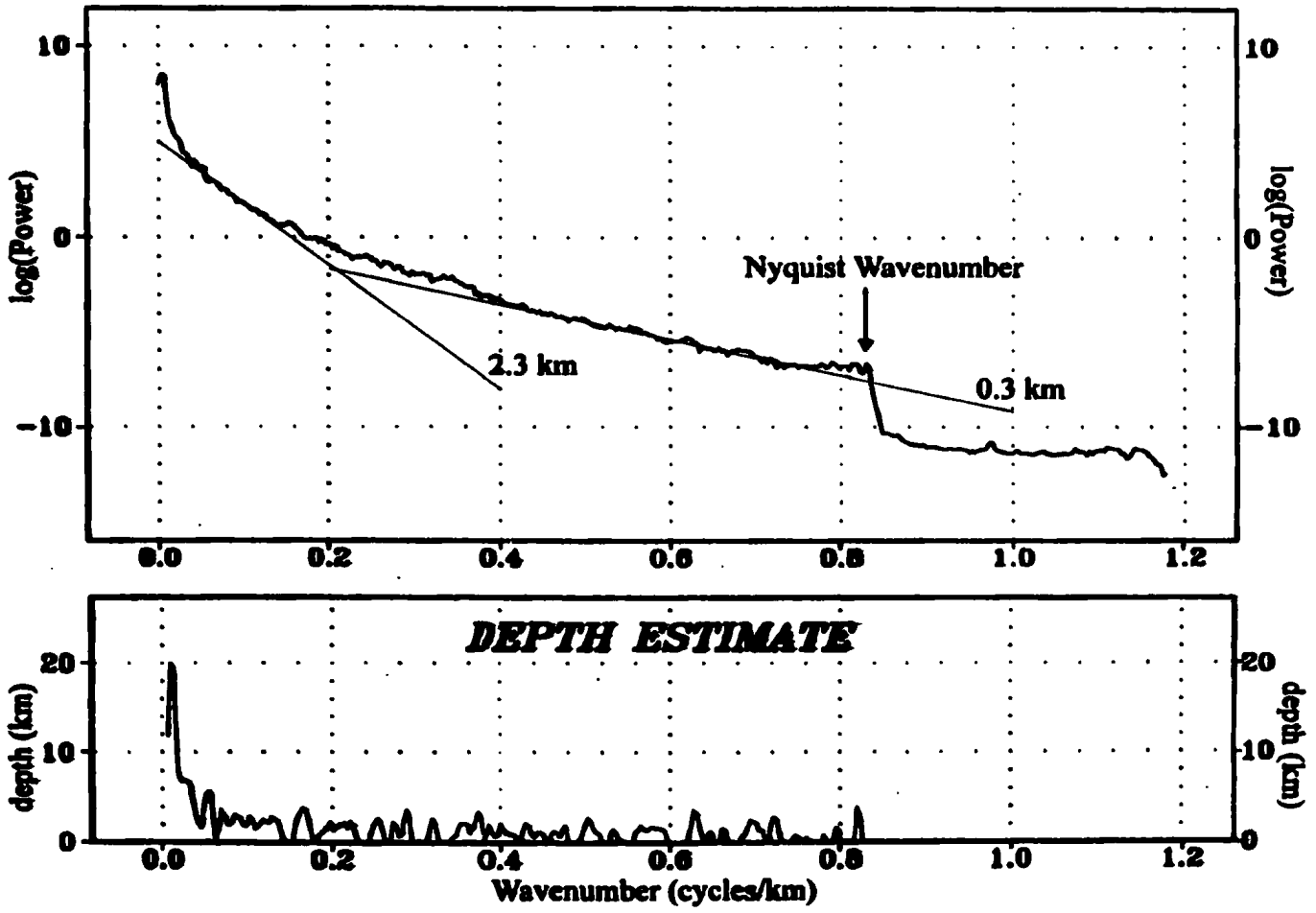

Figure 6.3-1: Power spectra analysis of the total magnetic field northwest and west of the Okavango Delta.

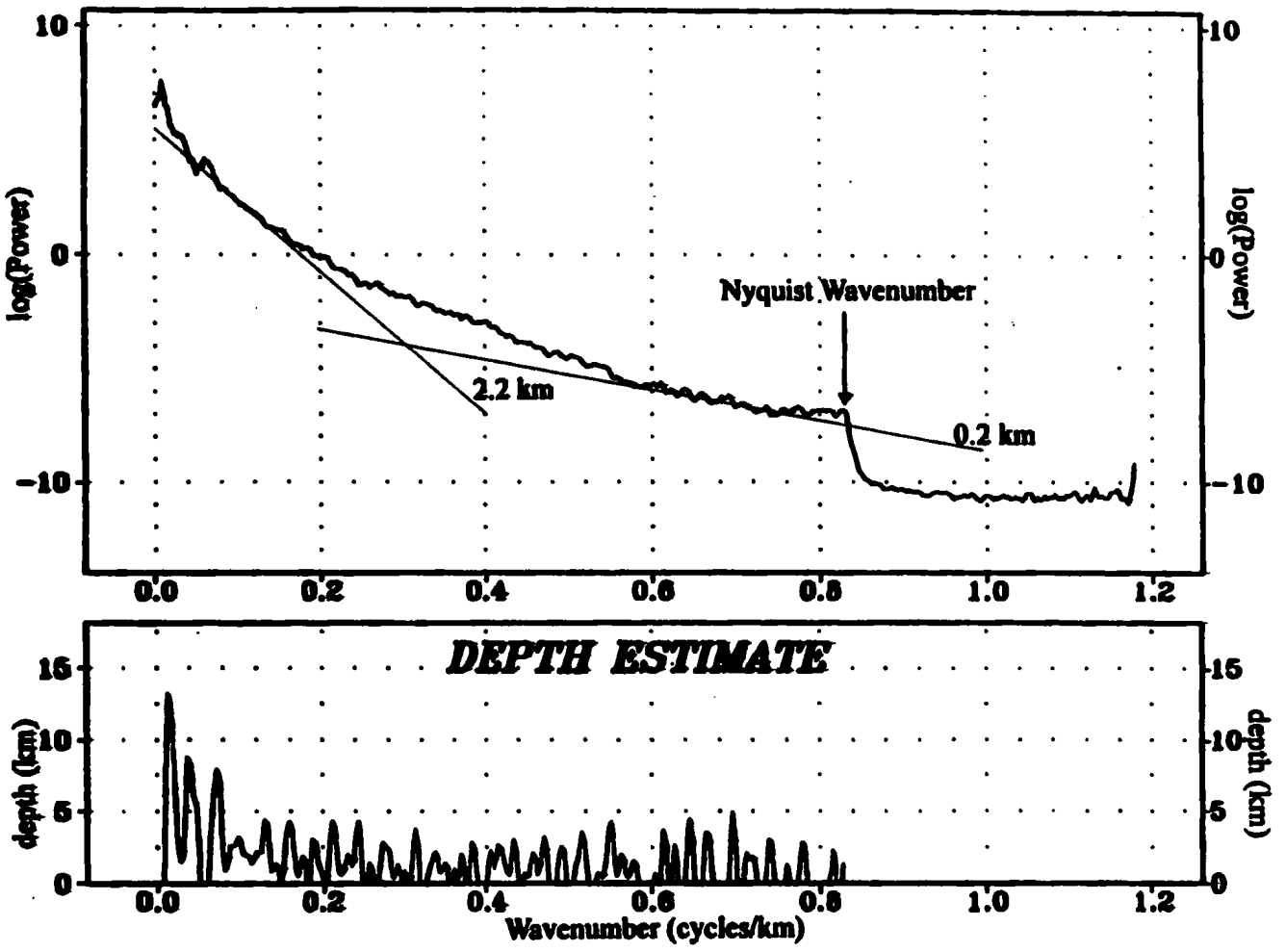

Figure 6.3-2: Power spectra analysis of the total magnetic field to the southeast edge of the Okavango Delta.

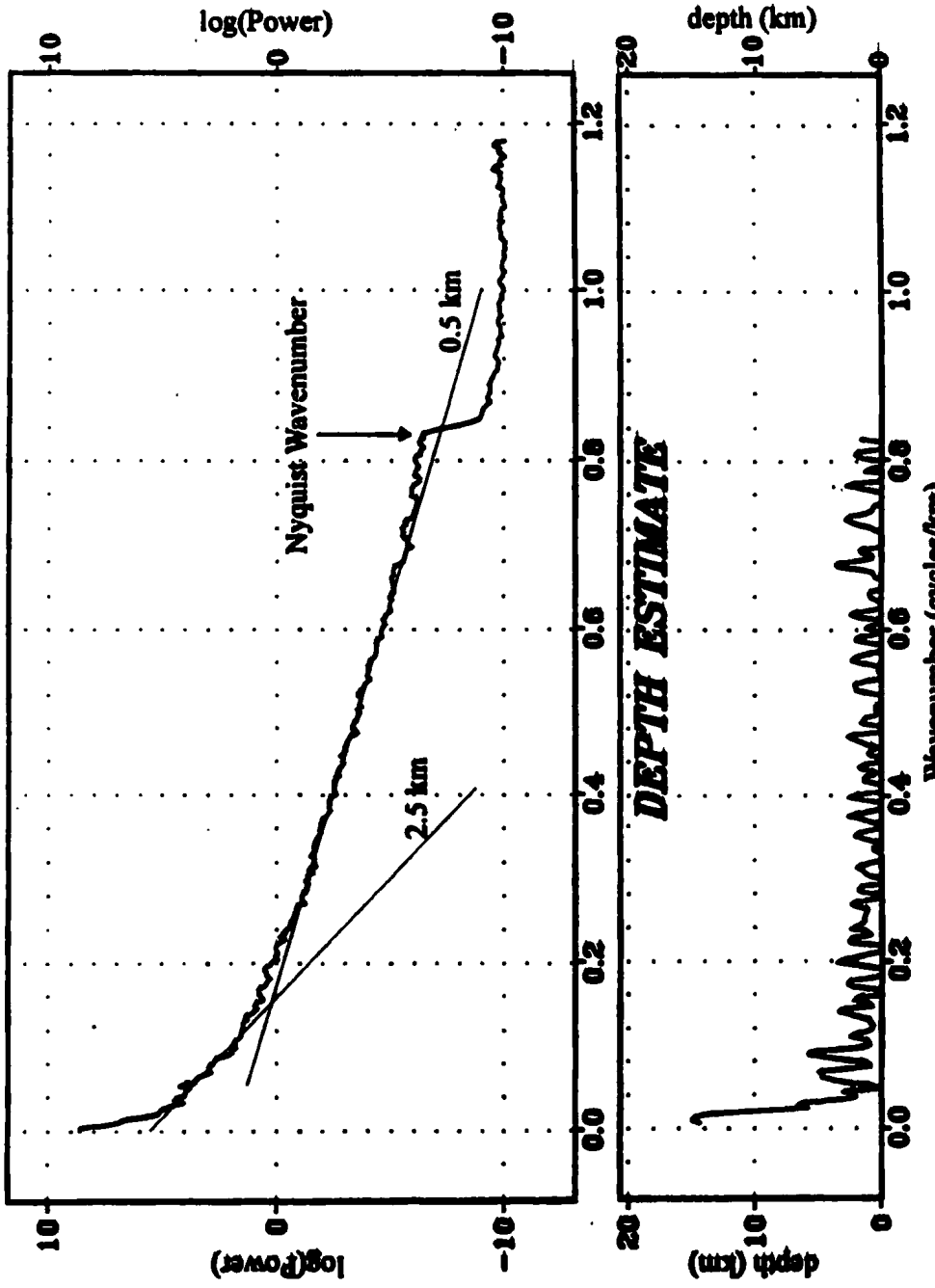

Figure 6.3-3: Power spectra analysis of the total magnetic field over the Okavango Delta.

6.4 Summary

The refraction statics model (fig. 4.3.2-2) indicates that the unsaturated zone is ~ 15 m thick over the entire seismic line. It overlies an impermeable horizon of variable thickness (0-50 m). The fault zone at CDP's 4360-4460 (fig. 6.2-1) is probably a recharge point.

Interpretation of the depth section (fig. 6.2-1) shows that the stratigraphy comprises three sedimentary units lying over an intrusive igneous body. The sediments are displaced by northwest dipping faults. These faults together constitute the Kunyere fault zone. The total cumulative fault displacement is 155 m to the northwest. The tentative stratigraphy is shown in Table 6-1.

Analysis of the aeromagnetic data shows that the basement to the northeast of the current line is likely to be Archean basement (fig. 2.1.4-1). The depth to basement established from statistical calculations is reliable and agrees closely with that measured by the seismic.

Overall, the seismic reflection experiment has established that Karoo beds may be present below the recent sediments at Marophe. The recent sediments thicken to the northwest. It is worth noting that Karoo basalt is absent from the beds at Marophe. That this does

not compromise the water quality in the likely Karoo aquifers can only be established through drilling.

Table 6-1: Stratigraphic relationships established from the current work at Marophe.

Age	Stratigraphic Unit	Thickness (m)		
		N of Fault	S of Fault	
		depth section	depth section	Strata®
Cenozoic	Okavango Beds	155		
	Kalahari Beds	230	200	191
Palaeozoic-Mesozoic	Karoo Beds	185	180	186
Basement	Post-Karoo basic intrusion		mafic sill ~22 m	
	Total (m)	570	380	377

7.0 CONCLUSIONS AND RECOMMENDATIONS

Processing of the current data was difficult because of ground roll and a low signal to noise ratio. The data quality could be improved during field acquisition by using deeper shot holes and a stack array setup to reduce ground roll. Hyperbolic velocity filtering was successful in attenuating the ground roll, but it increased the cost of processing. Also, the signal source used in this survey was fairly weak. It is suggested that a stronger signal source be used in future surveys of a similar nature in the Okavango.

Refraction statics analysis successfully delineated the near-surface velocity structure along the line. This analysis identified and mapped the unsaturated zone in detail. AVO and velocity inversions through the Hampson-Russell® programs have effectively imaged the stratigraphy south of the Kunyere fault zone. Both the bases of the Kalahari beds and the Karoo strata were mapped by these methods. AVO and Strata® inversions require recorded sonic and density logs to be more accurate. It is therefore necessary that such logs be collected during future drilling operations in the area.

Overall, analysis of the seismic data, and re-appraisal of the aeromagnetic data, produced a detailed geological structure and stratigraphy across the Kunyere fault zone at Marophe. The Kunyere fault zone has a total throw of ~ 155 m to the northwest. Furthermore, it has been adequately shown that Karoo sandstones are present below Tertiary cover at Marophe. The Karoo basalt is absent from the stratigraphy along the seismic line. This

would imply that the Karoo sandstones may have hydraulic continuity with the saline Kalahari beds and hence saline recharge.

The seismic reflection method has been shown in this survey to be well-suited to groundwater exploration in the Okavango because it is not affected by either salinity or velocity inversion. It is best employed at the detailed aquifer investigation stage to site test boreholes after a reconnaissance survey with potential fields methods.

References

Anstey, N.A., 1986. Field techniques for high resolution. Geophysics: The leading edge of exploration, 5, Nº 4, 26-34.

Barongo, J.O., 1984. Euler's differential equation and the identification of the magnetic point-pole and point-dipole sources. Geophysics, 49, Nº 9, 1549-1553.

Black, R.A., Steeples, W.D., and Miller, R.D., 1994. Migration of shallow seismic reflection data. Geophysics, 59, Nº 3, 402-410.

Borg, G., 1988. The Koras-Sinclair-Ghanzi rift in Southern Africa: volcanism, sedimentation, age relationships, and geophysical signature of a late Middle Proterozoic rift system. Precambrian Research, 38, Nº 1, 75-90.

Bureau de Recherches Géologiques et Miniéres (BRGM), 1984. Maun Water Supply Hydrogeological Survey. Interim report. Ministry of Mineral Resources and Water Affairs, Botswana.

Cabrera, J., and Levy, S., 1989. Shot dip moveout with logarithmic transformations. Geophysics, 54, Nº 8, 1038-1041.

Catterall, D.J., and Carruthers, H.E., 1992. Maun Copper Venture geological interim report. Anglo American Corporation Botswana. Unpublished.

Çoruh, C., Domoracki, W.J., Costain, J.K., 1995. Composite refraction-reflection stack sections: imaging shallow subsurface features. Symposium on the Application of Geophysics to Engineering and Environmental Problems, Orlando, pp. 937-943.

Davies, J., and Goldberg, G., 1980. Groundwater research in Botswana - past, present, and future, in: Hydrogeology in Commonwealth Africa, Volume 1, Ed. E.G. Hopkinson and C.F. Beavington, London.

de Beer, J.H., Gough, D.I., and van Zijl, J.S.V., 1975. An electrical conductivity anomaly and rifting in southern Africa. Nature, 255, 678-680.

Dincer, T., Child, S., and Khupe, B., 1987. A simple mathematical model of a complex hydrologic system - Okavango Swamps, Botswana. J. Hydrology, 93, 41-65.

Ellam, E.M., and Cox, K.G., 1989. A Proterozoic lithospheric source for Karoo magmatism: evidence from the Nuanetsi picrite. Earth Planet. Sci. Lett., 92, 207-218.

Farr, J.L., Cheney, C.S., Baron, J.H., and Peart, R.J., 1981. Evaluation of underground water resources. GS10 final report. Geological Survey, Botswana.

Fokkema, J.T., Baeten, G.J.M., and Vaage, S., 1990. Directional deconvolution in f-x domain. 60th Annual SEG meeting. Expanded abstracts. San Francisco. pp 1675-1676.

Gassaway, G.S., Brown, R.A., and Bennett, L.E., 1986. Pitfalls in seismic amplitude versus offset analysis: Case histories. 56th Annual SEG meeting. Expanded abstracts. Houston, pp. 332-334.

Gazdag, J., 1978. Wave equation migration with phase-shift method. Geophysics, 43, Nº 7, 1342-1351.

Geosoft Inc. Geosoft® Software for Earth Sciences, Geosoft Mapping System. 1995 Release. Toronto, Canada.

Gieske, A., 1993. Groundwater supply for the proposed Okavango Research Centre - University of Botswana. Unpublished.

Graebner, R.J., 1960. Seismic data enhancement. Geophysics, 25, Nº 1, 283-311.

Greenwood, P.G., and Carruthers, R.M., 1973. Geophysical surveys in the Okavango Delta, Botswana. Institute of Geological Sciences, Report Nº 15, London.

Gulunay, N., 1986. Fx-decon and complex Wiener prediction filter. 56th Annual SEG meeting. Expanded abstracts, Houston. pp. 279-281.

Hale, D., 1984. Dip-moveout by Fourier transform. Geophysics, 49, Nº 6, 741-757.

Hampson-Russell Software Services ltd. Hampson-Russell®, 1994. Calgary, Canada.

Hartnady, C., Joubert, P., and Stowe, C., 1985. Proterozoic crustal evolution in southern Africa. Episodes, 8, Nº 4, 236-244.

Hutchins, D.G., Hutton, S.M., Jones, C.R., and Loenhert, E.P., 1976. A summary of the geology, seismicity, geomorphology, and hydrogeology of the Okavango Delta. Geological Survey, Botswana.

Hutchins, D.G., Peart, R.G., and Herbert, P., 1977. Deep electrical soundings in the Okavango Delta - a trial survey. Internal report, Geological Survey, Botswana.

International Union for Conservation of Nature (IUCN), 1992. Review of the Okavango delta integrated water development project. Draft final report. Ministry of Mineral Resources and Water Affairs, Botswana.

Kocurko, T., 1994. Systems hardware and software, in: Memorial University Seismic Imaging Consortium, Annual Report.

Koosimile, D., 1994. Time domain EM of the Thamalakane and Kunyere faults (in preparation). Geological Survey of Botswana.

Lambiase, J.J., 1989. The tectonic framework of African rifting during the Phanerozoic. Journal of African Earth Sciences, 8, 183-190.

Landmark® Graphics Corporation. Insight IT&A 5.1, 1994. Houston, U.S.A.

Ludtke, G., 1986. Geophysical, geochemical, and geological investigations in the Ngamiland and Kheis areas of Botswana. Final report. Geological Survey, Botswana.

McCarthy, T.S., Stanistreet, I.G., and Cairncross, B., 1991. The sedimentary dynamics of active fluvial channels of the Okavango fan, Botswana. Sedimentology, 38, 471-487.

McCarthy, T.S., 1992. Physical and biological processes controlling the Okavango Delta - A review of recent research. Botswana Notes and Records, 24, 57-83.

Meixner, H.M., and Peart, R.J., 1984. The Kalahari Drilling Project: a report on the geophysical and geological results of follow-up drilling to the Aeromagnetic Survey of Botswana. Geological Survey, Botswana.

Mitchell, A.R. and Kelamis, P.G., 1990. Efficient tau-p hyperbolic velocity filtering. Geophysics, 55, Nº 5, 619-625.

Naess, O.E., and Bruland, L., 1985. Stacking methods other than simple summation, in: Developments in Geophysical Exploration Methods - 6, Edited by A.A. Fitch. Elsevier Applied Science Publishers. pp 189-223.

Naidu, P.S., 1970. Statistical structure of aeromagnetic field. Geophysics, 35, Nº 2, 279-292.

Neidell, N.S., and Taner, M.T., 1971. Semblance and other coherency measures for multichannel data. Geophysics, 36, Nº 3, 482-497.

Neumann-Redlin, Ch., 1980. Reconnaissance Hydrogeological Map sheet 1. Geological Survey, Botswana.

Nickerson, W., 1993. Seismic data processing for engineering and environmental applications. Memorial University of Newfoundland, Unpublished.

Noponen, I., and Keeney, J., 1986. Attenuation of waterborne coherent noise by application of hyperbolic velocity filtering during the tau-p transform. Geophysics, 51, Nº 1, 20-33.

Notfors, C.D., and Godfrey, R.J., 1987. Dip moveout in the frequency-wavenumber domain. Geophysics, 52, Nº 12, 1718-1721.

Ostrander, W.J., 1984. Plane-wave reflection coefficients for gas sands at non-normal angles of incidence. Geophysics, 49, Nº 10, 1637-1648.

Paterson, N.R., Redford, M.S., and Reeves, C.V., 1979. The reconnaissance aeromagnetic survey of Botswana - 1: some novel techniques of survey execution, data compilation and interpretation. in: The proceedings of a seminar pertaining to the Kalahari. Ed. G. McEwen. Geological Survey Department, Botswana.

Petters, S.W., 1991. Regional Geology of Africa. Springer-Verlag, Berlin.

Ram Babu, H.V., Vijayakumar, V., and Atchuta Rao, D., 1986. A simple method for the analysis of magnetic anomalies over dike-like bodies. Geophysics, 51, Nº 5, 1119-1126.

Ramananantoandro, R., 1995. Improvement of shallow reflection section using migration: Two case studies. Symposium on the Application of Geophysics to Engineering and Environmental Problems, Orlando, pp. 571-577.

Reid, A.B., Allsop, J.M., Granser, H., Millett, A.J., and Somerton, I.W., 1990. Magnetic interpretation in three dimensions using Euler deconvolution. Geophysics, 55, Nº 1, 80-91.

Reeves, C.V., 1978. The gravity survey of Ngamiland. Geological Survey, Botswana.

Reeves, C.V., 1979. The reconnaissance aeromagnetic survey of Botswana - ii: its contribution to the geology of the Kalahari, in: The Proceedings of a seminar pertaining to the Kalahari. Edited by G. McEwen. Geological Survey of Botswana, Bulletin 22.

Reeves, C.V., and Hutchins, D.G., 1982. A progress report on the geophysical exploration of the Kalahari in Botswana. Geoexploration, 20, 209-224.

Robinson, E.A., 1984. Seismic inversion and deconvolution. Part A: Classical methods, in: Handbook of seismic exploration. Edited by K. Helbig and S. Treitel. Vol. 4A.

Robinson, E.S., and Çoruh, C., 1988. Basic Exploration Geophysics. John Wiley & Sons, New York.

Ronen, J., and Claerbout, J.F., 1985. Surface-consistent residual statics estimation by stack power maximum. Geophysics, 50, № 12, 2759-2767.

Scholz, C.H., 1975. Seismicity, tectonics and seismic hazard of the Okavango Delta, Botswana. Final report to the United Nations Development Programme on the Okavango Delta, Investigation of the Okavango as a primary water source for Botswana, Food and Agriculture Organization.

Smith, R.A., 1984. The lithostratigraphy of the Karoo Supergroup in Botswana. Geological Survey, Botswana.

Snowy Mountains Engineering Corporation (SMEC), 1987. Southern Okavango Integrated Water Development. Phase 1 final report: Geomechanics and hydrogeology. Ministry of Mineral Resources and Water Affairs, Botswana.

Spector, A., and Grant, F.S., 1970. Statistical models for interpreting magnetic data. Geophysics, 35, Nº 2, 293-302.

Stanistreet, I.G., Kukla, P.A., and Henry, G., 1991. Sedimentary basinal responses to a Late Precambrian Wilson Cycle: the Damara Orogen and Nama Foreland in Namibia. Journal of African Earth Sciences, 13, Nº 1, 141-156.

Stoakes, F.A, and McMaster, D.W., 1990. Interpretation of the results of stratigraphic well - Masetlheng pan-1 in the Nosop-Ncojane basin of Southwest Botswana. Petro-Canada International Assistance corporation.

Stoffa, P.L., Buhl, P., Diebold, J.B., and Wenzel, F., 1981. Direct mapping of seismic data to the domain of intercept time and ray parameter - A plane wave decomposition. Geophysics, 46, Nº 3, 238-254.

Tankard, A.J., Jackson, M.P.A., Eriksson, K.A., Hobday, D.K., Hunter, D.R., and Minter, W.E.L., 1982. Crustal evolution of southern Africa. Springer-Verlag. New York.

Treitel, S., Gutowski, P.R., and Wagner, D.E., 1982. Plane wave decomposition of seismograms. Geophysics, 47, Nº 10, 1375-1401.

Seismic Image Software ltd. Vista® 6.6, 1992. Calgary, Canada.

Yilmaz, Ö., 1987. Seismic Data Processing. Ed. Stephen M. Doherty. Society of Exploration Geophysicists, Tulsa.

APPENDIX A

The following table lists the (x,y,z) coordinates for the seismic line established by a transit survey. The (x,y) coordinates are UTM zone 34, referred to a Central Meridian of 21° E, and 0° latitude. The Clarke 1880 projection spheroid is used for the production of local maps. The initial and final station coordinates (101 and 628) were recorded with a NAV 5000 GPS (Global Positioning System) with an uncertainty of ± 30 m for (x,y) and ± 0.1 m for z. The survey points were located to within ± 0.5 m (x,y) and ± 0.1 m (z) by the transit survey.

Table A1: Survey information for the seismic line at Marophe. The table continues to page 151.

SURVEY STN	NORTHING (m)	EASTING (m)	ELEVATION (m)
101	7785606	733226	929.0
108	7785582	733285	928.6
115	7785561	733346	928.8
123	7785544	733418	928.9
128	7785523	733459	929.4

SURVEY STN	NORTHING (m)	EASTING (m)	ELEVATION (m)
133	7785503	733498	929.5
137	7785475	733522	928.9
142	7785459	733563	928.3
151	7785407	733630	928.3
160	7785358	733692	928.7
172	7785292	733777	929.7
180	7785251	733836	929.4
185	7785222	733870	929.7
196	7785163	733952	930.8
204	7785118	734009	931.8
216	7785056	734097	932.3
222	7785025	734141	931.2
226	7785003	734171	930.5
235	7784962	734240	930.5
237	7784953	734257	931.0

SURVEY STN	NORTHING (m)	EASTING (m)	ELEVATION (m)
244	7784911	734303	931.3
255	7784848	734381	931.5
271	7784761	734497	931.7
292	7784646	734647	932.6
306	7784570	734748	932.5
322	7784487	734867	933.5
329	7784447	734916	934.9
333	7784424	734945	936.5
338	7784397	734981	937.8
342	7784374	735010	938.0
347	7784347	735047	937.1
353	7784313	735091	937.2
358	7784284	735126	937.1
364	7784255	735172	937.0
376	7784189	735258	936.9

SURVEY STN	NORTHING (m)	EASTING (m)	ELEVATION (m)
401	7784118	735352	937.3
409	7784070	735407	936.9
420	7784008	735484	936.3
451	7783939	735570	936.6
465	7783862	735669	936.8
479	7783784	735768	937.1
495	7783696	735884	937.3
508	7783626	735975	937.2
520	7783561	736059	937.7
532	7783495	736144	937.7
544	7783430	736228	938.0
556	7783366	736311	937.9
568	7783302	736395	938.2
580	7783237	736480	937.4
593	7783166	736572	937.8

SURVEY STN	NORTHING (m)	EASTING (m)	ELEVATION (m)
605	7783101	736656	937.8
617	7783034	736741	937.7
628	7782974	736817	937.7